# Ultrasound investigations of spin-ice materials

DISSERTATION

zur Erlangung des akademischen Grades

**Doctor rerum naturalium**
(Dr. rer. nat.)

vorgelegt

der Fakultät
Mathematik und Naturwissenschaften

von

Salim Erfanifam
geboren am 21.01.1983 in Maragheh, Iran

HOCHFELD-MAGNETLABOR DRESDEN
Helmholtz-Zentrum Dresden-Rossendorf e. V.
2013

GUTACHTER:
Prof. Dr. Joachim Wosnitza
Prof. Dr. Peter Lemmens

*Eingereicht am:* December 19, 2013
*Tag der Verteidigung:* noch offen

# Contents

# Abstract

This thesis is devoted to ultrasound investigations of a family of rare-earth compounds known as spin ice. The crystal structure of these compounds is composed of tetrahedral units with magnetic ions in each corners. In the ground state of these materials, two spins are directed inward on each tetrahedron and two spins outward. There are a number of features that are common to the spin-ice materials $Ho_2Ti_2O_7$ (HTO), $Yb_2Ti_2O_7$ (YbTO), and $Dy_2Ti_2O_7$ (DTO). In DTO, nonequilibrium processes have been probed by ultrasound waves at low temperatures. The sound velocity and sound attenuation exhibit a number of unusual anomalies as a function of applied magnetic field for temperatures below the freezing temperature of  500 mK. These robust anomalies can be seen for longitudinal and transverse acoustic modes for different field directions. The anomalies show broad hystereses. Most notable are peaks in the sound velocity, which exhibit two distinct regimes: an intrinsic (extrinsic) regime in which the data collapse for different sweep rates when plotted as function of field strength (time). Moreover, these quasi-periodic peaks are strongly affected by thermal-coupling conditions. We discuss our observations in context of emergent quasi-particles (magnetic monopoles) which govern the low-temperature dynamics of spin ice.

I have studied spin-lattice and single-ion effects in the spin-ice materials (DTO) and (HTO) in a wide range of temperatures and magnetic fields. The sound velocity and sound attenuation of various acoustic modes experience a renormalization due to phase transformations as well as interactions with low-energy magnetic excitations (topological defects). In particular, a sharp dip observed in the sound attenuation has been explained within the framework of the spin-ice model. In addition, crystal-electric-field effects lead to a renormalization of the sound velocity and sound attenuation at very high magnetic fields. We analyze our observations using an approach based on exchange-striction couplings and single-ion-type interactions.

Experiments on YbTO revealed evidence of a first-order transition known as a transition from a magnetic Coulomb liquid (MCL) to Coulomb ferromagnet state at $T = 0.15$ K. Coupling of the sound waves to quantum fluctuations cause a sharp anomaly in the sound velocity and sound attenuation. An increase of the quantum-fluctuation frequency when lowering the temperature down to the

phase transition, leads to a minimum in the sound velocity and a maximum in the sound attenuation. This behavior can be explained in frame of resonating sound waves in presence of quantum fluctuations. Below the transition temperature, the quantum fluctuation effects are less pronounced. Measurements in applied magnetic fields, revealed a transition from a fluctuating Coulomb-ferromagnet state to a state with suppressed fluctuations.

The experimental data presented in this thesis, show the important role of spin-strain interactions in spin-ice materials. In addition, theoretical considerations based on exchange-striction couplings and single-ion strain interaction, strongly support most of the experimental results.

# 1 Introduction

There is currently strong interest in the study of frustrated systems in solid-state physics. In magnetic systems, frustrations manifest themselves in a number of interesting properties. Due to their (thermodynamically) large ground–state degeneracy, frustrated magnets often remain in a disordered state down to lowest temperatures. In geometrically frustrated systems, phenomena arise which are in large part due to the collective behavior of the system [1–3]. In these systems topological excitations may exist which can be observed experimentally. Prominent examples of the topological excitations or emergent quasiparticles are those with fractionalized electric charge in the quantum Hall effect and fractionalized magnetic dipoles in a class of geometrical frustrated magnets known as spin ice [4].

The spin-ice materials belong to a family of compounds of rare-earth titan oxides with pyrochlore lattice [5]. These materials show a variety of remarkable phenomena such as (quantum) spin-ice [5, 6] states, as well as quantum spin-liquid states [7]. In the spin-ice state, two spins are directed inward and two spins outward (2 in–2 out state) on each tetrahedron which is the building unit of the pyrochlore lattice. In spin-ice materials with quantum effects, there is quantum tunneling between different configurations of 2 in – 2 out states. The elementary excitations of spin ice can be achieved by an ice–rule breaking spin flip in a tetrahedron to a so-called 3 in–1 out (or 3 out–1 in) state. These excitations appear as sources or sinks of the magnetic-field flux and break topological constraints. Indeed, these exotic states can be treated as magnetic monopoles.

Historically the theory of magnetic monopoles started with Dirac's paper in 1931 [8]. Based on Dirac's theory, magnetic monopoles can be created by stretching a magnetic dipole in a way to separate the north pole from the south pole. These separated poles, which are connected via an unobservable so-called Dirac string, can be regarded as point-like monopole-antimonopole particles. The searches for such exotic particles from the 1970s through the 1990s were performed mostly in condensed-matter and astrophysics. In February 1982, the transit of a magnetic monopole through a SQUID detector was reported [9], but the result of this experiment has never been reproduced. Therefore, there is no firm evidence for the existence of Dirac monopoles until today. Magnetic monopoles in spin-ice compounds are emergent quasiparticles which can exist independently in the material. At present, many aspects of these emergentquasi particles are still not well understood. The experimental results and theoretical analysis given in this thesis address some of these aspects.

Several experimental studies have been conducted to explore the properties of spin-ice materials (see Refs. [10, 11] for review). We used ultrasound to investigate the behavior of different longitudinal and transverse acoustic modes in a wide range of temperatures, from 0.02 to 300 K, and magnetic fields up to 62 T. This thesis addresses the spin–lattice and crystal-electric-field effects in the spin-ice materials $Dy_2Ti_2O_7$ (DTO), $Ho_2Ti_2O_7$ (HTO), and $Yb_2Ti_2O_7$ (YbTO). In our experiments, a phase–sensitive detection technique was employed to measure the relative change of the sound velocity, $\Delta v(T,H)/v$, and the sound attenuation, $\Delta\alpha$, as a function of temperature and external magnetic fields. The sound velocity and the sound attenuation are measured mainly for pure acoustic modes (for which the wave vector is parallel or perpendicular to the displacement vector) to probe characteristic responses of spin ice to the induced strain at different fields and temperatures.

At low temperatures, the sound characteristics exhibit a number of anomalies as a function of applied magnetic field. In particular, non-equilibrium processes are probed by ultrasound waves. These anomalies are related to avalanches of emergent quasiparticles (magnetic monopoles). The non-stationary processes observed in field sweeps in DTO have been argued to arise from inability of the phonons to carry away the Zeeman energy released by the flipping spins. As an additional proof, our results demonstrate that the thermal coupling of the sample to the bath (environment) is important for the non–equilibrium response of magnetic monopoles to the applied field. In HTO, however, we have only observed rather smooth features in the same temperature and magnetic field range. Apparently, in HTO the relaxation to equilibrium is too fast to be detected in our experiments: such fast relaxation channels are presumably provided by nuclear Ho spins in HTO.

Astonishingly, the sound attenuation of the acoustic $c_T$ mode exhibits a sharp decrease at the first-order gas-liquid-type transition, evidencing negative relaxation processes. This relaxation happens to the some dynamical steady state configuration of spins having higher energy than the lowest energy in the absence of sound waves. Such behavior is very unusual and rarely observed. We analyze our observations using an approach based on exchange-striction couplings and single-ion-type interactions. The temperature dependences of the sound velocity and sound attenuation in DTO and HTO indicate a high sensitivity of the spin-ice state to both the sweep rate and the sample history at low temperatures. Moreover, we have shown that the single–ion magneto-elastic coupling is responsible for high-temperature and high-magnetic-field anomalies of the sound characteristics. Crystal-electric-field effects lead to a renormalization of the sound velocity and sound attenuation at very high magnetic fields.

Ultrasound experiments also have been performed on the quantum spin-ice compound $Yb_2Ti_2O_7$ (YbTO). Anomalies in the sound velocity and sound attenuation evidence a first-order transition known as a transition from a magnetic Coulomb liquid (MCL) to a Coulomb ferromagnet state. Our measurements in applied magnetic fields revealed a transition from a fluctuating Coulomb ferromagnet state to a state with suppressed fluctuations. Reasons for the sound-velocity and sound-attenuation renormalization are discussed.

This thesis is organized as follows: In chapter two, a brief introduction to the elastic properties of solids is presented. In chapter three, the used experimental technique is described. In chapter four, the spin-ice state and magnetic monopoles are described. In chapters five, six, and seven, the results obtained with ultrasound experiment on the sound velocity and sound attenuation in (quantum) spin ice are discussed. In chapters five and six an analysis of the results based on exchange-striction couplings and crystal electric field (CEF) effects are presented.

# 2 Elastic properties of solids

This chapter gives an introduction to the theory of elasticity and its consequences for the calculation of the sound velocity and sound attenuation in condensed matter, focusing on the plane-wave limit. Elastic constants in cubic crystal systems are considered. Then, the attenuation of the acoustic waves in solids is discussed. Afterwards, the interaction of the acoustic waves with magnetic ions by two mechanisms of magneto-elastic couplings are introduced: single–ion strain interaction and exchange striction. Additionally, symmetry aspects are discussed.

## 2.1 Hook's law and elastic constants

In the 17th century Robert Hooke an English natural philosopher, discovered that the extension of a spring is directly proportional to the load applied to it [12, 13]. From Hooke's law, along with Newton's second law, follows that the time a particle needs to move and return to its equilibrium position is independent of the force applied, within a given material.

For long acoustic wavelengths, ($\lambda >> a$, in which, $a$ is the lattice constant) local displacements of atoms and the internal structure of the unit cell is irrelevant from the viewpoint of vibrations, therefore, the solid can be regarded as a continuous elastic medium [14]. The discontinuity of the lattice becomes important only for vibrations of shorter wavelengths ($\lambda \approx a$). In terms of frequencies, the interpretation of lattice vibrations as elastic waves is justified for frequencies up to the order of $10^{11}$ Hz [14]. Consideration of the solid bodies as continuous media leads to the theory of elasticity. The basic equations of elasticity were established in the 1820's by Cauchy and by Poisson [15]. In the elastic medium a relation between the stress and the strain is given by Hooke's law. A more general relationship between the stress tensor, $\sigma_{ik}$, and the strain tensor $\epsilon_{jl}$ can be expressed by $\sigma_{ik} = \sum_{jl} c_{ikjl}\epsilon_{jl}$ in which the elastic constants, $c_{ikjl}$, are composed of a four-index tensor. The stress tensor, $\sigma_{ik}$, represents the components of force per unit area acting on an element in the solid; the first subscript denotes the direction of the normal to the plane on which the stress component acts, and the second subscript denotes the direction of the stress

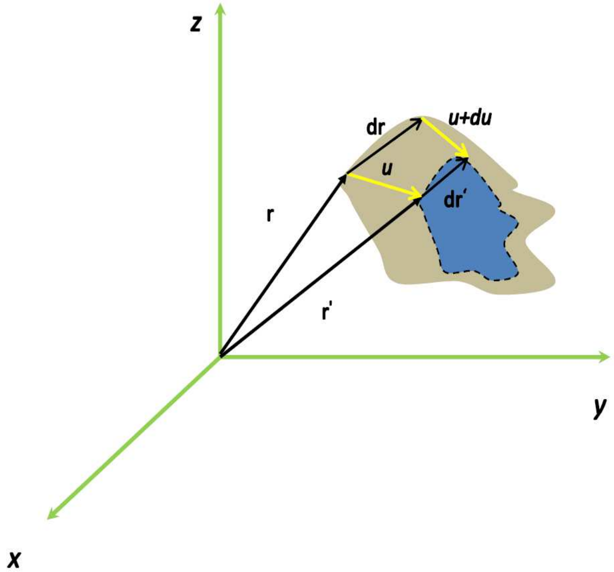

Figure 2.1: Displacement vectors, $\vec{u}, d\vec{u}$ of a volume element by shifting from site $r$ to $r'$ in an elastic deformation used for the description of strain.

component. Because of symmetry conditions arising from the assumed absence of torques, the stress tensor is symmetric, $\sigma_{ik} = \sigma_{ki}$. The Cauchy relations are symmetries that permit any permutation of the four tensor indices and give rise to six reductions [15]. The symmetry of $\sigma_{ik}$ and $c_{ikjl}$ in the first pair and last pair of indices makes it possible to simplify the notation by going to matrix form in which each pair of indices takes values as shown in table 2.1 [16].

Table 2.1: notations of elastic constants.

| tensor notation | 11 | 22 | 33 | 23, 32 | 13, 31 | 12, 21 |
|---|---|---|---|---|---|---|
| matrix notation | 1 | 2 | 3 | 4 | 5 | 6 |

The strain tensor interprets the coordinates of a point $x$ before and after deformation [17, 18]. The elastic constants are defined as the ratio of the applied stress to the strain (change in the shape of an elastic body). It is worth of note that the elastic constants have the dimensions of energy per unit volume.

By considering elastic waves in an isotropic medium one can write, in plane-wave approximation : $\rho\ddot{u}_i = \partial\sigma_{ik}/\partial x_k$. Here, $\sigma_{ik}$ is a component of the stress tensor and $u$ the displacement vector introduced in Fig 2.1. With the stress–strain relation, mentioned above which is the phenomenological Hooke's law, the vibrations of an elastic medium of density $\rho$ are governed by the equation of motion [19]: $\rho\ddot{u}_i = c_{iklm}\frac{\partial^2 u_m}{\partial x_k \partial x_l}$. For plane waves, $\mathbf{u}_i = u_{0i}e^{i(\mathbf{k}\cdot r-\omega t)}$ the velocity of propagation of the wave, v, can be obtained using this equation. Applying the matrix notation, the elastic coefficients can be defined in terms of a mass density and sound velocity:

$$c_{ij} = \rho v^2. \tag{2.1}$$

So far, we have discussed elasticity from a phenomenological or macroscopic point of view. In principle, the motion of the atoms in a lattice can be determined from a microscopic point of view by considering the interatomic potential energy, $V(u)$ [20, 21]. The potential can be expanded in powers of the displacement $u$,

$$V(u) = V_0 + \frac{1}{2}(\frac{\partial^2 V}{\partial u^2})u^2 + \frac{1}{3}(\frac{\partial^3 V}{\partial u^3})u^3 + ... \tag{2.2}$$

The approximation in which only second–order terms of the expanded potential are kept is called the harmonic approximation. By starting the description of elastic waves using this potential in the long–wavelength limit of acoustic vibrations, the energy of the elastically deformed crystal can be derived in terms of an elastic constant and strain.

## 2.2 Elastic constants in a cubic crystal system

The general relationship between the stress and strain by 36 independent elastic constants can be represented in matrix format. Reductions in the number of independent constants are possible by employing symmetry considerations. As we mentioned above (Sec. 2.1), symmetry in the elastic-constant matrix requires that $c_{ij} = c_{ji}$. There are 6 constants where $i = j$. Since $c_{ij} = c_{ji}$, only half of the remainning 30 constants with $i \neq j$ are independent. Therefore, for the lowest possible crystallographic symmetry (triclinic crystal systems) there are 21 independent elastic constants [18]

$$\begin{pmatrix} c_{11} & c_{12} & c_{13} & c_{14} & c_{15} & c_{16} \\ c_{12} & c_{22} & c_{23} & c_{24} & c_{25} & c_{26} \\ c_{13} & c_{23} & c_{33} & c_{34} & c_{35} & c_{36} \\ c_{14} & c_{24} & c_{34} & c_{44} & c_{45} & c_{46} \\ c_{15} & c_{25} & c_{35} & c_{45} & c_{55} & c_{56} \\ c_{16} & c_{26} & c_{36} & c_{46} & c_{56} & c_{66} \end{pmatrix}.$$

A further reduction in the number of elastic constants occurs because of the symmetry in cubic systems. These symmetry considerations lead to $c_{12} = c_{13} = c_{23}$, $c_{44} = c_{55} = c_{66}$, $c_{11} = c_{22} = c_{33}$, and all of the other coefficients are zero. Therefore, cubic systems require only three independent constants $c_{11}$, $c_{12}$, and $c_{44}$ [22] leading to

$$\begin{pmatrix} c_{11} & c_{12} & c_{12} & - & - & - \\ c_{12} & c_{11} & c_{12} & - & - & - \\ c_{12} & c_{12} & c_{11} & - & - & - \\ - & - & - & c_{44} & - & - \\ - & - & - & - & c_{44} & - \\ - & - & - & - & - & c_{44} \end{pmatrix}.$$

In an isotropic solid, there are two types of longitudinal and transverse sound waves which can propagate through the material. For longitudinal sound waves the propagation direction, $k$, is along the polarization direction, $u$, while, for transverse sound waves the propagation is perpendicular to the polarization. Using the equation of motion (mentioned in section 2.1) and sound waves with propagation and polarization directions along the principal axes of cubic systems, the sound velocities can be calculated from the independent elastic constants ($c_{11}$, $c_{12}$ and $c_{44}$) and mass density.

In Table 2.2 and Fig. 2.2 some elastic constants for different crystallographic directions in a cubic crystal are shown [17, 18]. The elastic constants for other crystal systems (tetragonal, orthorhombic and hexagonal) can be found in following references [17, 18].

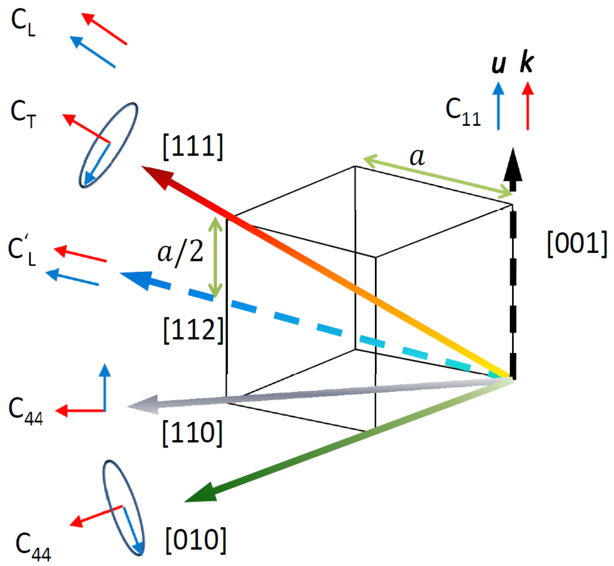

Figure 2.2: Various acoustic modes in a cubic crystal symmetry.

Table 2.2: Elastic constants and corresponding propagation and polarization direction of sound waves.

| | |
|---|---|
| $k \parallel u \parallel [111]$ | $c_L = \frac{c_{11}+2c_{12}+4c_{44}}{3}$ |
| $k \parallel [111] \perp u$ | $c_T = \frac{c_{11}+c_{44}-c_{12}}{3}$ |
| $k \parallel u \parallel [112]$ | $c_L^{'} = \frac{3c_L+3c_{11}-12c_T}{6}$ |
| $k \parallel u \parallel [001]$ | $c_{44} = \frac{6c_T-3c_{11}+3c_L}{6}$ |

## 2.3 Attenuation of acoustic waves in solids

The basic properties of acoustic waves in solids can be determined by the measurement of the attenuation and velocity of the sound waves [17, 18, 22]. The elastic constants of a solid can be determined using the mass density and the sound velocity, as mentioned in Sec. 2.2. In this section, the attenuation of acoustic waves in solid is discussed.

In real materials, the dissipation mechanisms of elastic waves can provide additional information on their physical properties [18, 22]. These dissipation mechanisms cause an attenuation of the elastic waves according to the distance traveled. The term “attenuation” is usually used for energy losses (as measured by an amplitude decay) arising from all causes when elastic waves are propagating through a solid medium. These total losses can be classified in broad sense as scattering and absorption arising from the intrinsic physical character of the solid under study. The sources for attenuation also can be classified in those intrinsic to the medium and those associated with the boundaries of the medium. Losses in the medium can be further classified into three basic types: viscous losses, heat-conduction losses, and losses due to internal molecular processes.

In order, to obtain the attenuation in terms of energy losses at a certain distance the acoustic waves traveled in the medium, we consider the sound waves in plane-wave approximation [18, 19]:

$$\mathbf{u}(r,t) = \mathbf{u}_0 e^{i(\omega t - \mathbf{k}\cdot\mathbf{r})}, \tag{2.3}$$

where $\omega$ is the angular frequency and $\mathbf{k}$ is the propagation vector (see above).

An expression for an attenuated wave can be obtained by assuming that either the propagation vector or that the frequency is complex.

In order to obtain the attenuation in terms of distance it is assumed that $\mathbf{k}$ is real, and that $\mathbf{v}$ and $\omega$ are complex. Thus,

$$\omega = \omega_1 + i\alpha_1,$$

which gives

$$\mathbf{u}(r,t) = u_0 e^{-\alpha_1 t} e^{i(\omega t - \mathbf{k}\cdot\mathbf{r})}, \tag{2.4}$$

where $\alpha_1$ has the dimension of reciprocal time. A substitution in $k^2 v^2 = \omega^2$ of the quantities defined by $\mathbf{v} = \mathbf{v}_1 + i\mathbf{v}_2$ and $\omega = \omega_1 + i\alpha_1$ yields, in this case,

$$\alpha_1 = \mathbf{k}\mathbf{v}_2.$$

Since the attenuation is determined by the amplitude of the high–frequency wave, one can use

$$\mathbf{u}(r) = \mathbf{u}_0 e^{-\alpha\mathbf{r}}.$$

Taking the logarithm, than can be written as

$$\log \mathbf{u}(r) = \log \mathbf{u}_0 - \alpha \mathbf{r}. \tag{2.5}$$

Then, the difference of Eq. 2.5 for two points of $\mathbf{r}_1$ and $\mathbf{r}_2$, where $\mathbf{r}_1 < \mathbf{r}_2$, results in

$$\alpha = \frac{1}{|\mathbf{r}_2 - \mathbf{r}_1|} \frac{\log \ u(r_1)}{\log \ u(r_2)}. \tag{2.6}$$

Detailed treatments of the attenuation can be found in, Truell *et al.* [18] and Tucker [22].

## 2.4 Symmetry approach to the elastic media

Molecules consist of finite numbers of atoms, and their symmetry is described by so–called space-symmetry groups, point-group symmetries and local symmetries [23, 24]. For example, the point-group symmetry can be used for the classification of the electronic states of a molecule [23]. The 32 crystallographic point groups can be classified into seven systems: cubic, hexagonal, rhombohedral, tetragonal, orthorhombic, monoclinic, and triclinic. The point groups in Schoenflies notation are as follows [25]:

(1) Cubic: $O_h$, $O$, $T_d$, $T_h$, $T$;
(2) Hexagonal and rhombohedral: $\mathrm{D}_{6h}$, $\mathrm{D}_6$, $\mathrm{C}_{6v}$, $\mathrm{C}_{6h}$, $\mathrm{C}_6$, $\mathrm{D}_{3h}$, $\mathrm{C}_{3h}$, $\mathrm{D}_{3d}$, $\mathrm{D}_3$, $\mathrm{C}_{3v}$, $\mathrm{S}_6$, $\mathrm{C}_3$;
(3) Tetragonal: $\mathrm{D}_{4h}$, $\mathrm{D}_4$, $\mathrm{C}_{4V}$, $\mathrm{C}_{4h}$, $\mathrm{C}_4$, $\mathrm{D}_{2d}$, $\mathrm{S}_4$;
(4) Orthorhombic, monoclinic and triclinic: $D_{2h}$, $D_2$, $C_{2v}$, $C_{2h}$, $C_2$, $C_s$, $S_2$, $C_1$.

The classification of electron and phonon states in crystals requires the knowledge of the full symmetry group of a crystal (space group) [17, 26] and irreducible representations of the space groups. In elastic media, the strain tensor, $\epsilon$, can be given in form of irreducible representations of strain of the corresponding point group.

Using the linearized stress-strain relation, which is the phenomenological Hooke's law, one can calculate the elastic energy density from the work done due to the deformation. The elastic energy density can be written as:

$$F = \frac{1}{2} C_{ijkl} \epsilon_{ij} \epsilon_{kl} = \frac{1}{2} C_{mn} \epsilon_m \epsilon_n. \tag{2.7}$$

As an example, we consider the case of cubic symmetry. Using the equation above, the elastic energy density for cubic symmetry can be written as

$$F = \frac{1}{2} C_{11}(\epsilon_x^2 + \epsilon_y^2 + \epsilon_z^2) + C_{12}(\epsilon_x \epsilon_y + \epsilon_x \epsilon_z + \epsilon_y \epsilon_z) + \frac{1}{2} C_{44}(\epsilon_{yz}^2 + \epsilon_{zx}^2 + \epsilon_{xy}^2). \tag{2.8}$$

Here, the strains are dimensionless and the elastic constants can be expressed in GPa. The elastic energy density is quadratic in the strains. This equation can be rewritten as following:

$$\begin{aligned} F = \tfrac{1}{2} \tfrac{(C_{11}+2C_{12})}{3} (\epsilon_{xx} + \epsilon_{yy} + \epsilon_{zz})^2 + \tfrac{1}{2} \left\{ \tfrac{1}{2}(C_{11} - C_{12}) \right\} \\ \left\{ \tfrac{1}{3}(2\epsilon_{zz} - \epsilon_{xx} - \epsilon_{yy})^2 + (\epsilon_{xx} - \epsilon_{yy})^2 \right\} + \tfrac{1}{2} C_{44}(\epsilon_{yz}^2 + \epsilon_{zx}^2 + \epsilon_{xy}^2). \end{aligned} \tag{2.9}$$

Therefore, we have the desired symmetry strains and symmetry elastic constants composed from $\epsilon_{ij}$ and from $c_{11}$, $c_{12}$, and $c_{44}$. In Eq. (2.9), $\epsilon_{xx} + \epsilon_{yy} + \epsilon_{zz}$ is called volume strain, $\epsilon_B$, which is associated with the bulk modulus $C_B = (C_{11}+2C_{12})/3$. The symmetry strains $\epsilon_v = \epsilon_{xx} - \epsilon_{yy}$ and $\epsilon_u = (2\epsilon_{zz} - \epsilon_{xx} - \epsilon_{yy})/\sqrt{3}$ are associated with the transverse $(C_{11} - C_{12})/2$ mode. Also the symmetry strains $\epsilon_{xy}$, $\epsilon_{zx}$, and $\epsilon_{yz}$ are linked to the transverse $C_{44}$ mode.

Figure 2.3 shows the various symmetry strains and related elastic constants for a cubic symmetry. One can see from Fig 2.3, that some of these symmetry strains such as $\epsilon_{xy}$, $\epsilon_{zx}$, and $\epsilon_{yz}$ as well as the tetragonal distortions $\epsilon_u$ and $\epsilon_v$ are volume conserving, while $\epsilon_B$ is not [17]. This property of the symmetry strains is crucial for a number of phenomena. For example, the conservation of volume is an essential parameter in structural transitions, while the absence of volume conservation plays an important role in superconductivity.

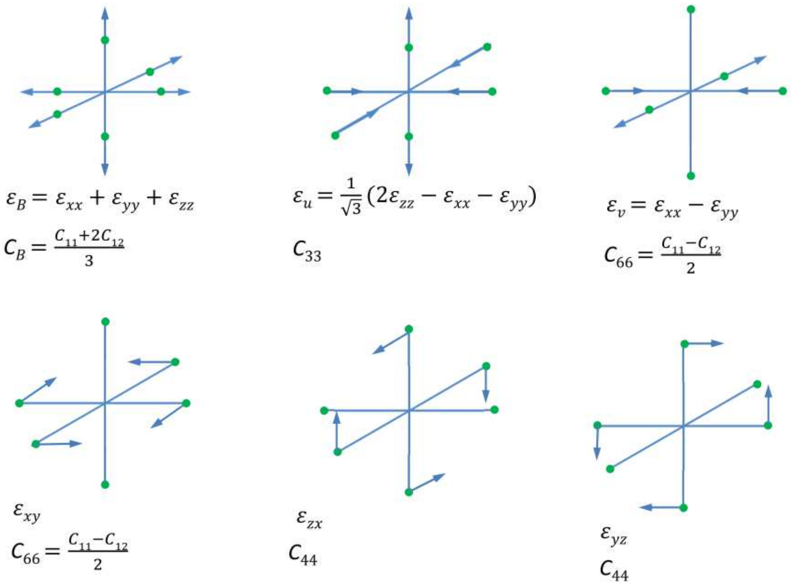

Figure 2.3: Symmetry strains for cubic symmetry and related elastic constants.

## 2.5 Sound-wave interaction with magnetic ions

There are various mechanisms by which sounds waves interact with magnetic ions [17]. Spin-lattice interactions can be generally described by single-ion or two-ion magneto-elastic coupling (exchange striction) [17, 26–30]. For example, systems with diluted magnetic ions or some rare-earth compounds at high temperatures can exhibit single-ion effects [17]. In some low-dimensional spin systems or ferromagnetic materials the exchange-striction mechanism plays an important role [17].

Both mechanisms of the spin–lattice interaction mentioned above can be used in one approach for conduction and localized electrons. In the first case, the sound velocity and attenuation can be strongly affected by the conduction electrons. Manifestations of this coupling can be for example an anomalous temperature dependence of certain elastic constants and magnetoacoustic quantum oscillations.

For insulating magnetic materials in single-ion approximation, Van Vleck [31], suggested that the interaction between the magnetic moment of an ion and lattice vibrations is indirect. Based on this theory, lattice vibrations change the CEF which can results in a change of the orbital state of the ion. The latter change then can be transferred to the magnetic moment by means of spin-orbit coupling

[31, 32]. In insulators, the spin-lattice coupling is responsible for a number of effects such as: an anomalous temperature dependence of elastic constants and the cooperative Jahn–Teller effect.

In this thesis, all compounds studied are insulators, and, therefore, spin–lattice interactions for localized electrons is only relevant. In the next two subsections, we will introduce two different mechanisms of spin–lattice interaction; single-ion-strain interaction and exchange-striction couplings.

### 2.5.1 Single-ion-strain interaction

As we mentioned above, the coupling of the strain to a magnetic ion can be considered as single ion–strain interaction. This interaction arises from the modulation of the crystal electric field by strain change.

Using symmetry strains of the irreducible representation of the crystal group symmetry, Γ, combined with quadrupole ($l = 2$ for $3d$ ions) and higher order multi–pole operators ($l = 4$ and 6 for $4f$ ions), the single-ion magneto–elastic Hamiltonian is given by

$$H_{me} = \sum_{\Gamma,n} g_{\Gamma,n} \epsilon_\Gamma O_{\Gamma,n}. \tag{2.10}$$

Here, $\mathrm{g}_\Gamma$ is the magneto–elastic coupling constant, $O_{\Gamma,n}$ is the multipolar operator with $n = 2$, 4, and 6 and $\epsilon_\Gamma$ is a symmetry strain. As an example, for the symmetry strains $\epsilon_\Gamma$ for cubic symmetry the quadrupolar operator for the same symmetry is $O_\Gamma$. The quadropolar operators can be expressed in terms of the Steven's operators $O_l^m$ [17]. The Steven's operators in turn can be written in terms of angular-momentum components $J_i$. The field and temperature dependence of the elastic constants in rare–earth compounds can be explained by single–ion-strain coupling mechanism [33]. Moreover, a softening of an elastic constant indicates the coupling of the magnetic ion to the strain in that elastic mode.

In this thesis, the results of some theoretical calculations based on the single-ion-strain interactions will be presented in section 6.2.1.

### 2.5.2 Exchange Striction

Two-ion magnetoelastic coupling or exchange striction arises from the modulation of exchange interactions by changes in the lattice configuration (see Fig. 2.4). This mechanism usually can be responsible for a number of elastic effects and interesting phenomena such as propagation of sound wave near some phase transitions e. g. an anomalous behavior in thermal conductivity [34]. The Hamiltonian describing exchange striction can be written as follows:

$$H_{exs} = \sum_{i,j} \left[ J(\boldsymbol{\delta} + \mathbf{u}_i - \mathbf{u}_j) - J(\boldsymbol{\delta}) \right] \mathbf{S}_i \cdot \mathbf{S}_j. \tag{2.11}$$

Here $\boldsymbol{\delta} = \mathbf{R}_i - \mathbf{R}_j$ measures the distance between two magnetic ions and $\mathbf{u}_i$ is the displacement vector for the ion $\mathbf{R}_i$. With a sound wave given by $\mathbf{u} = U\mathbf{e}_q exp(i(\mathbf{q} \cdot \mathbf{r} - \omega t)$ with $\mathbf{e}$ is the polarization vector, $\mathbf{U}$ amplitude of the wave and $\omega$ is the frequency of the sound wave, the exchange striction can be written as follows:

$$H_{exs} = \sum_{i,j} \left[ \frac{dJ}{dr} (\frac{\boldsymbol{\delta}}{\delta}).(\mathbf{u}_i - \mathbf{u}_j) \right] \mathbf{S}_i \cdot \mathbf{S}_J. \tag{2.12}$$

There are various experimental methods, to determine the derivative of the coupling constant. $dJ/dr$. Therefore, in special cases, such as for low-dimensional spin systems, one can determine it from the temperature and field dependence of the elastic constants [29, 35–41].

Another way to estimate $\frac{dJ}{dr}$ is from the pressure dependence of the Curie or N$\acute{e}$el temperatures or from thermal-expansion anomalies at these temperatures. Using the magnetic Grüneisen parameter, i.e. the logarithmic volume derivative of the exchange interaction which can be written in terms of the critical temperature ($T_c$), pressure, and bulk modulus [17] as

$$\Gamma_m = \frac{\partial \ln J}{\partial \ln V} = -c_B \frac{\partial \ln T_c}{\partial p}. \tag{2.13}$$

With $c_B$ the bulk modulus, an average exchange-striction constant can be determined from the pressure dependence of the magnetic transition temperature [17]. When the nearest-neighbor exchange interaction, $J_{nn}$, is antiferromagnetic (negative) and if the exchange interaction decreases with increasing separation between the magnetic ions, the system (magnetic plus elastic) will lower its energy by contracting. For positive $\frac{\partial \ln J}{\partial r}$ an expansion is energetically more favorable.

Magnetoacoustic studies of the spin-ice material DTO will be discussed in section 5.3 using the exchange-striction mechanism.

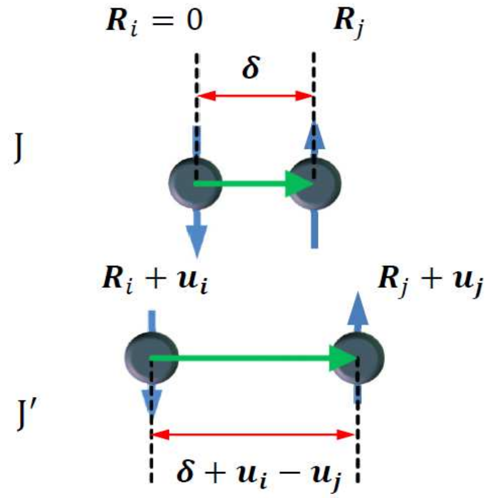

Figure 2.4: Schematic visualization of the exchange striction between two magnetic ions. The change of the distance between the two magnetic ions is shown by displacement vectors, $\mathbf{u}_i$, $\mathbf{u}_j$, for the ions in the positions $\mathbf{R}_i$ and $\mathbf{R}_j$. The exchange interactions before and after the displacement are $J$ and $J^{'} = J + \frac{dJ}{dr}(\frac{\boldsymbol{\delta}}{\delta}).(\mathbf{u}_i - \mathbf{u}_j)$ for the distances $\delta$ and $\delta + u_i - u_j$ between the ions, respectively.

# 3 Technical details of ultrasound studies

The ultrasound technique is an experimental method which can be favorably used for the investigation of magnetoelastic interactions by probing the bulk response of materials on sound-wave propagation. Typically, the sound velocity and sound attenuation are measured as a function of external parameters. The ultrasonic frequency range is normally regarded from about 20 kHz to 1000 MHz (although the upper limit of the ultrasound frequency in not very well defined). In the last few decades, different methods have been used to measure the sound velocity and sound attenuation [17, 18, 22]. In one approach, this technique can be classified based on methods which use ultrasound transducers and others which do not use it. For example, Raman scattering, vibrating reed, and Brillouin scattering belong to the transducer-free class of methods [17, 22]. For transducer-based methods, phase sensitive detection is most widely used to measure the sound velocity and attenuation. Another interesting method is the resonant ultrasound spectroscopy, where a rectangular shaped sample is placed between two piezoelectric plates [17, 18, 22].

In this thesis, I used the phase-sensitive detection method under static and pulsed high magnetic fields at low temperatures. For the measurements, piezoelectric transducers were bond to the sample under investigation. A pulsed electromagnetic signal is applied across the piezoelectric transducer. Due to the piezoelectric effect, an acoustic wave is excited and then propagates through the specimen.

In the next section, we discuss in detail the measurement of the sound velocity and sound attenuation. The basic elements of the pulse-echo method and the sample preparation are treated in section 3.2. The measurements under static and pulsed magnetic field will be addressed in sections 3.3 and 3.4.

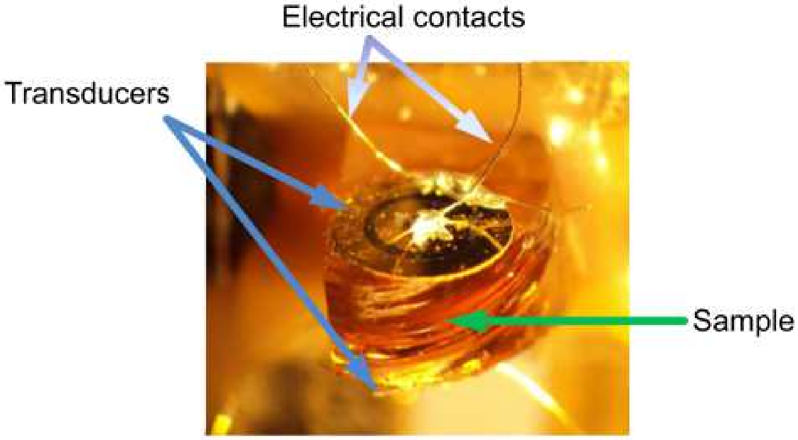

Figure 3.1: Sample–transducer arrangement for an ultrasound experiment. The electrical contacts are gold wires bond to the transducer with silver paste.

## 3.1 Measurement of sound velocity and sound attenuation

As we mentioned above, there are several methods of sound-velocity and sound-attenuation measurements using piezoelectric transducers. Here, one of these techniques based on the phase-comparison method will be explained. In this method, first an electric radio-frequency pulse generates acoustic waves in a piezoelectric transducer bond to the sample (see Fig. 3.1). Then, the acoustic wave passes through the sample experiencing multiple reflections. The time delay for an ultrasound pulse to travel from one transducer to another or to return to the same transducer as well as the ratio of the sound waves amplitude after each reflection can be measured. The obtained data yield, for a known path length, the absolute sound velocity and the sound attenuation.

Absolute measurements of the sound velocity can vary in accuracy as a function of several parameters, such as sample path length, acoustic impedance match between the sample and the transducer, thickness of the transducer, and thickness of the bond. The longer the sample path length, the better the resolution in ultrasound echo patterns. In addition, often the presence of cross talk effecting the echo patterns is inevitable. To obtain a better signal, the cross talk should be reduced. One of the advantages of this method is the low average energy input to the crystal, therefore, low–temperature measurements are easily possible.

## 3.2 Sample preparation

Single crystals used in this thesis were grown by G. Balakrishnan and A. Maljuk under oxygen-gas flow by the floating-zone method in an infrared furnace (for detailes of growing the pyrochlore rare–earth titanates refer to [42]). The samples were cut and polished leading to two parallel surfaces perpendicular to the high-symmetry crystallographic directions (this procedure is general for any kind of samples). The high-symmetry directions in cubic crystals are along the [111], [110] and [001] crystallographic axes. This orientations were controlled by X-ray Laue diffraction. Resonance $LiNbO_3$ or wide-band PVDF-film (polyvinylidene fluoride film) piezoelectric transducers glued on the polished surfaces of the sample were used to generate and detect ultrasound waves in the frequency range of 30 - 200 MHz. The quality and number of observable echoes after multiple reflections depends on a number of parameters, such as quality of the crystal and parallelism of the surfaces. The sample was fixed in a sample holder made out of brass in $^3$He, or $^4$He gas-flow cryostats or a dilution refrigerator.

Since the transducer is a very important part of the experiment, let us consider briefly the properties of transducers used in this technique. For ultrasonic applications, transducers constructed of piezoelectric materials are used most commonly. Transducers can be used both as transmitters and receivers of mechanical vibrations for a wide range of frequencies. To determine the ultrasonic properties of a specimen, the ultrasonic losses in the transducer should be small compared to those in the specimen. An essential feature of piezoelectricity is the validity of a linear relationship between applied electric field and mechanical stress or strain. Although piezoelectricity is a bulk property, the conversion of electrical to mechanical energy occurs principally at the surfaces of piezoelectric devices. There exist a number of crystals which can be used as piezoelectric transducers, such as quartz or $LiNbO_3$. Natural crystals such as quartz are inherently piezoelectric, with properties determined by their crystallographic features. Quartz exhibits a low ultrasonic attenuation (high mechanical quality factor Q) and a low electromechanical coupling coefficient. The electromechanical coupling coefficient is a parameter which describes how efficient the conversion of the electrical to the acoustic energy is.

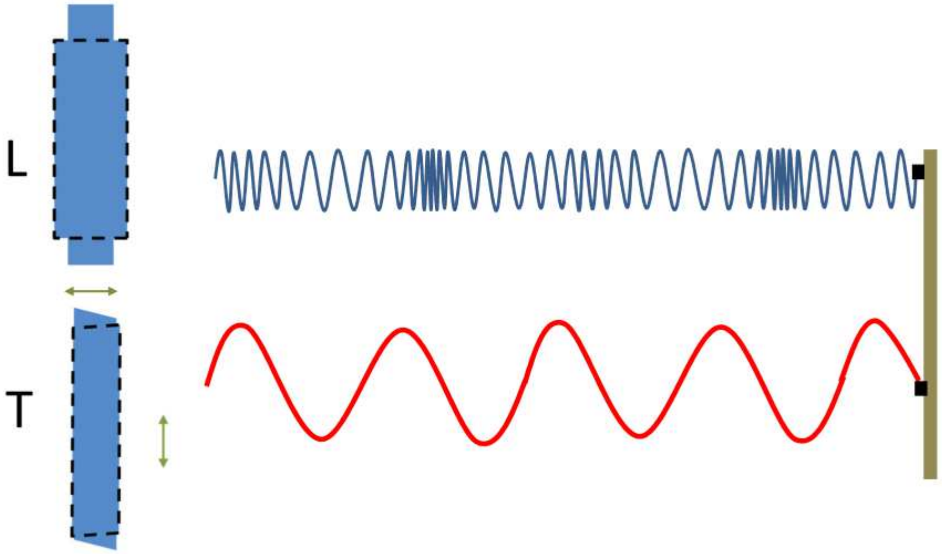

Figure 3.2: The response of a piezoelectric transducer to an alternating voltage and the generation of a longitudinal (L) or transverse wave (T).

The piezoelectric transducers can resonate in a thickness expander mode for the generation and detection of longitudinal waves or in a thickness shear mode for the generation and detection of transverse waves (see Fig. 3.2). In contrast to the transverse transducers, for longitudinal transducers the polarization and propagation directions of the sound waves are the same. A particular transducer must be chosen in accordance with the specific application. The longitudinal transducers used in this work are $\mathrm{LiNbO_3}$ thin films and the transverse ones are 41 deg X-cut lithium niobate overtone transducers with $2.8 \pm 0.08$ mm diameter.

## 3.3 Measurements in static magnetic fields

In this section, the setup used for the ultrasonic measurements is described. The phase-sensitive detection method, employed in this work, enables us to measure simultaneously the ultrasonic velocity, $\Delta v/v$, and the attenuation $\Delta\alpha$. These measurements can be carried out as a function of temperature and magnetic field.

Figure 3.3 shows a simplified electronic circuit of the setup. With the frequency generator a frequency between 30 and 500 MHz is chosen, depending on the signal quality monitored by an oscilloscope. The pulse generator sets all time intervals and triggers the whole setup with a pulse duration of 50 - 200 nsec and a typical repetition rate of 2 kHz. The pulses amplified by a power amplifier are converted to ultrasonic pulses and vice versa by the transducers on both sides of the sample. The transit time of a ultrasonic wave propagated through the sample is denoted by $\tau_0$ (see Fig. 3.4a). Each following echo with exponentially decaying intensity, is delayed by $2\tau_0$. Each transit gives a phase shift of the signal of $\phi = kL_0$. The $n$-th echo, therefore, has a phase shift of

$$\Phi_n = kL_0(2n+1) = \frac{\omega}{v}L_0(2n+1), \tag{3.1}$$

with respect to the reference signal. Here, $k$ is the wave number of the ultrasound wave, $L_0$ the length of the sample, $\frac{\omega}{2\pi}$ is the frequency $f$, and $v$ is the sound velocity.

In order to obtain the phase change, the received signal from the sample ($B = B_0 \cos(\omega t + \phi_n)$) is amplified and multiplied to the $90^0$ phase shifted signals received from a quadrature hybrid ($A_1$ and $A_2$) and then split into two channels (channels $I_n$ and $Q_n$). The change of the phase shift can be related to the relative change of the sound velocity in absence of any change in the sample length and ultrasound frequency (see Eg. (3.2)). According to this equation, the sound velocity can be measured by either locking the frequency or locking the phase. In the method used, there is a feedback loop (see Fig. 3.3) to keep the phase constant,

$$\frac{dv}{v} = \frac{d\omega}{\omega} - \frac{d\Phi_n}{\Phi_n} + \frac{dL}{L_0}. \tag{3.2}$$

The sound attenuation can be measured by taking the $90^0$ shifted Q channel. The sound attenuation has been discussed in Sec. 2.3. The sound attenuation in the unit $\frac{db}{cm}$ can be calculated for echo number n by:

$$\alpha = \frac{-20}{(2n+1)L_0} \log \frac{Q}{Q_0}, \tag{3.3}$$

where $Q_0$ is the signal $Q$ at the beginning of the measurement.

In this technique, the frequency range of $30 - 500$ MHz is covered and the duration of the ultrasonic pulse can be tuned from $10^{-7}$ sec up to a few $\mu$sec. The repetition rate may strongly affect the sample temperature and lies in order of a few hundred Hz for measurements in the mK temperature range. At higher temperatures, it can be increased up to 3 kHz or even up to 50 kHz for measurements in pulsed field (see next section).

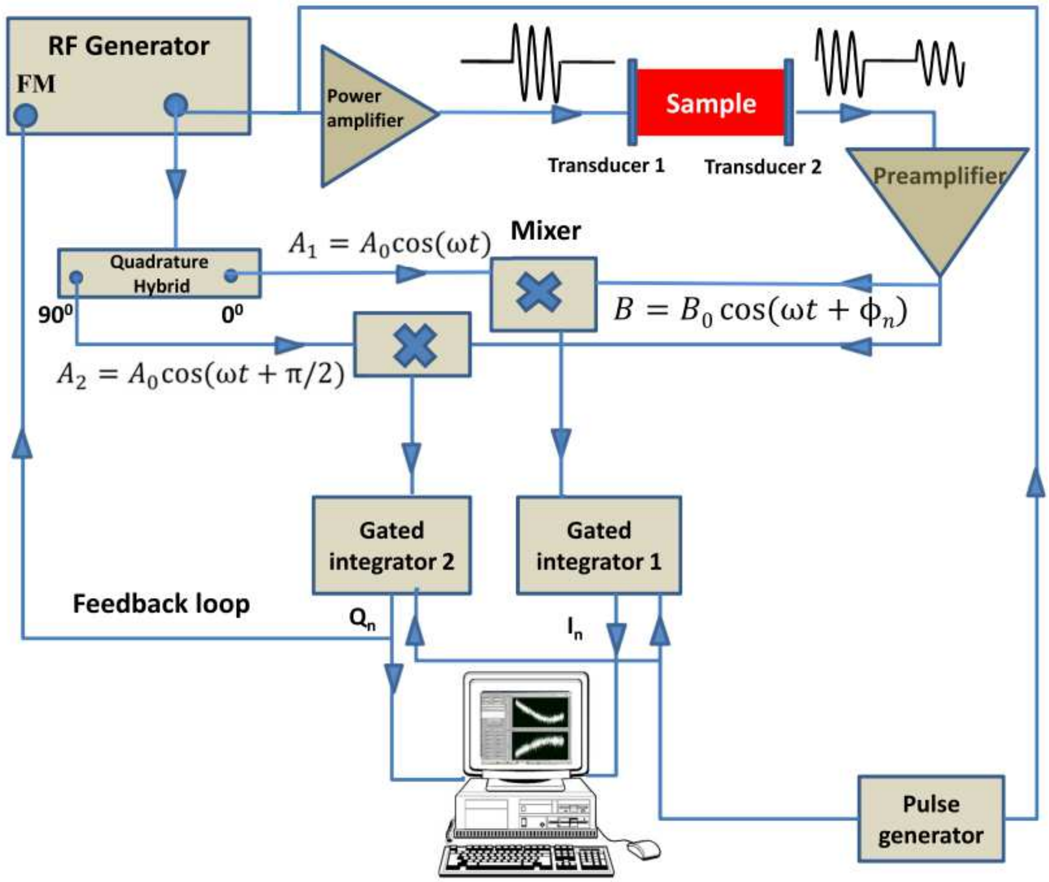

Figure 3.3: Experimental setup for measuring the sound velocity and attenuation. Here we show the apparatus with frequency feedback control.

## 3.4 Measurements in pulsed magnetic fields

For the measurements in pulsed magnetic fields the same setup as for static fields can be used with small differences in the data-acquisition system. The feedback loop described for the measurements in static magnetic fields is too slow to follow the changes in pulsed magnetic fields. Therefore, the experiments have to be performed at a locked-frequency mode. The signals $I_n$ and $Q_n$ for a typical echo pattern are shown in Fig. 3.4a. The phase and amplitude changes from both channels can be extracted. The change in the sound velocity is inversely proportional to the change [see Eq. 3.1] in the phase which must be determined from the data of the two channels.

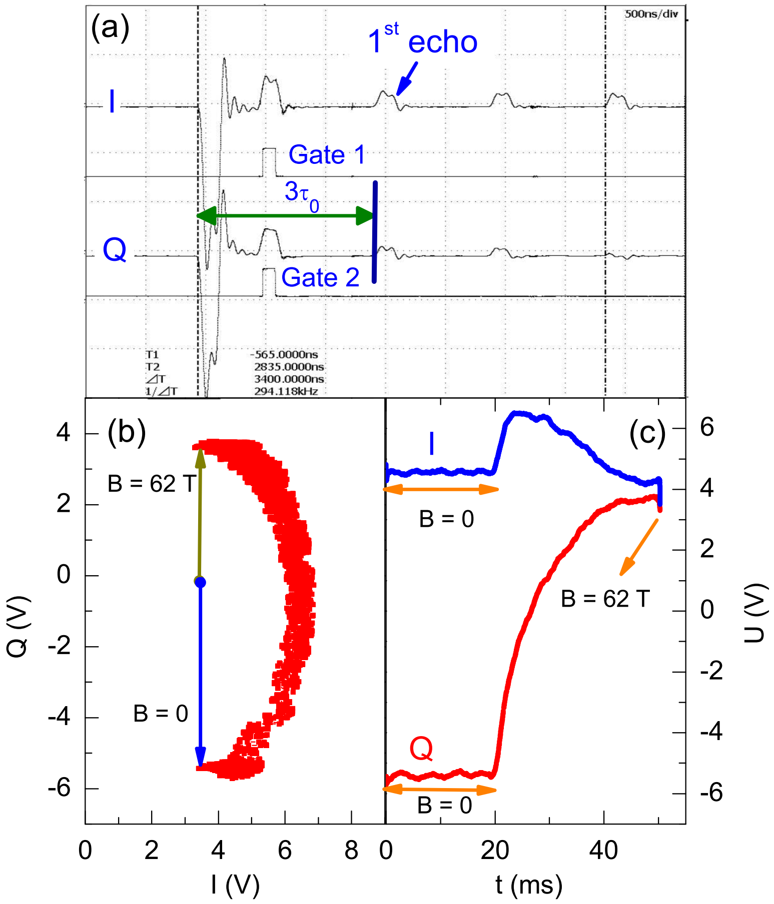

Figure 3.4: (a)Sound-echo trains versus time for the channels $I$ and $Q$ with $90^0$ phase shift between them. The 1st echo is denoted by an arrow. Gate 1 and gate 2 determine the time for signal integration in both channels. (b) Evolution of $I$ with respect to $Q$ under an applied field. (c) Amplitude change of $I$ and $Q$ versus time. The applied field in this case was up to 62 $T$.

The change of sound the velocity leads to a rotation of a vector in the $I-Q$ plane. With increasing field the vector moves from the position for $B=0$ to the position with $B=62$ T (Fig. 3.4b). From Eq. 3.1 one can write:

$$\Phi_n = \frac{\omega}{v} L_0(2n+1) = 2N\pi + \arctan(\frac{Q_n}{I_n}), \tag{3.4}$$

in which $N$ is an integer number. From above, the relative change of the sound velocity in pulsed-field measurements can be written as:

$$\frac{\Delta v}{v} = -\left[\frac{\arctan(\frac{Q}{I}) - \arctan(\frac{Q_0}{I_0})}{2\pi f(2n+1)\tau_0}\right]. \tag{3.5}$$

The sound attenuation can be calculated from the length of the vector ($A_n = \sqrt{I_n^2 + Q_n^2}$ shown in Fig. 3.4b), where the vector length is proportional to the sound amplitude

$$\Delta\alpha = -\frac{20}{L_0} \log \frac{\sqrt{|Q|^2 + |I|^2}}{\sqrt{|Q_0|^2 + |I_0|^2}}. \tag{3.6}$$

The repetition rate of the ultrasonic pulses has to be higher in the pulsed-field experiments. For a pulse duration of 100 ms a repetition frequency of the order of 50 kHz is desirable. The resolution of the sound-velocity measurements for the setup shown in Fig. 3.3 is of the order of $10^{-6}$ for static-field measurements. For pulsed fields this reduces to about $10^{-5}$.

For the generation of pulsed magnetic fields at the Dresden High magnetic Field Laboratory (HLD), there is an energy discharge of a capacitor bank through a specially designed coil (see Fig. 3.5). The maximum stored energy in the capacitor bank is about 50 MJ. The discharge is triggered by optically driven switches. This coil is cooled by liquid nitrogen. The experiments have been carried out using $^4$He cryostats down to 1.4 K. In Fig. 3.6 we show the typical time dependence of a pulsed field used for ultrasound experiments. The rise time to maximum magnetic field is about 25 ms and the complete pulse duration is about 150 ms (see Fig. 3.6). Detailed information about the capacitor bank, discharge processes, and coil design can be found in the references [43, 44].

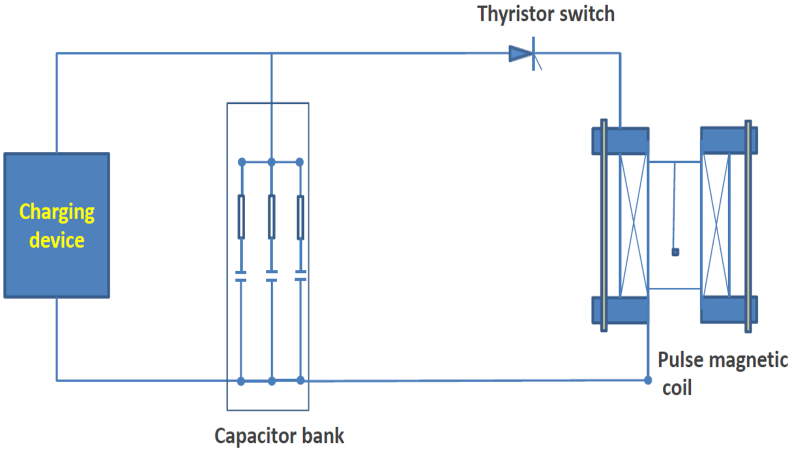

Figure 3.5: Simplified electric circuit of the pulsed field instrument. The coil is energized by capacitor bank.

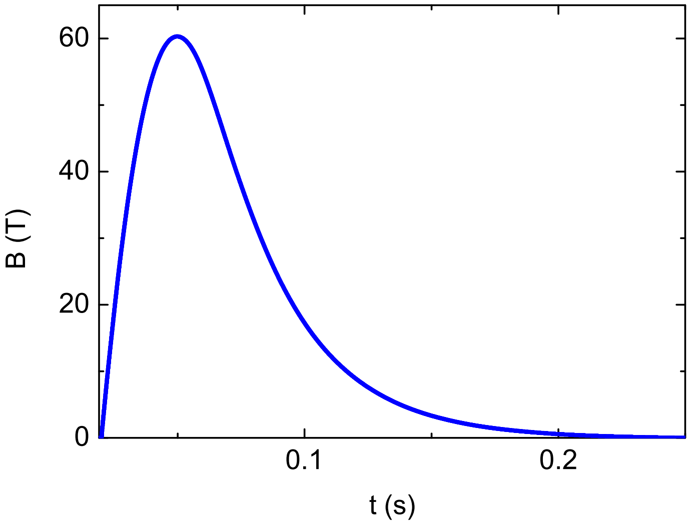

Figure 3.6: Time dependence of a pulsed magnetic field used for ultrasound experiment.

# 4 Spin ice and magnetic monopoles

In this chapter, I review some properties of spin-ice materials with particular attention to magnetic monopoles occurring in spin-ice materials. In the history of physics, the hypothesis about the possible existence of a magnetic monopole (as a fundamental particle), has remained the focus of intensive research by generations of physicists. Investigations in solid state physics, have recently addressed the presence of magnetic monopoles in some pyrochlore oxides. Materials with the general formula $R_2Ti_2O_7$ where R is a rare-earth ion, exhibit various properties ranging from spin liquid, spin ice, quantum spin liquid to quantum spin ice. The magnetic monopoles in the pyrochlores arise from local fractionalization of dipole moments [4]. This chapter reviews their properties, mainly from an experimental perspective.

This chapter is organized in the following way. In the next two sections I introduce some basic features of the theory of spin ice. The third section reports on the properties of DTO and HTO. The forth section is a review on magnetic monopoles. Finally, the magnetic monopoles in spin ice will be discussed.

## 4.1 Theory of spin ice

For more than a decade, the pyrochlore rare–earth titanates $R_2Ti_2O_7$ have been intensively studied experimentally and theoretically as model systems of spin ice [5, 10, 11, 45]. These materials have a face-centered cubic structure and space group $FdN\bar{3}m$ and there are eleven ions per unit cell. In the 1960s, Anderson [46] considered the direct mapping of the pyrochlore lattice onto the water-ice lattice. The spin-ice state in which two spins of a tetrahedron are directed inward and two spins are directed outward , was mentioned in a paper on geometrical frustration in the pyrochlore compound HTO by M. J. Harris *et al.* in 1997 [47]. In 1999, A. P. Ramirez *et al.* noticed that there is an analogy between the properties of the geometrically frustrated Ising pyrochlore compounds HTO and DTO [5, 10, 45].

According to an argument of Pauling [48], the residual entropy of water ice at 0 K is $S_0 = k_B \log\Omega_0 = \frac{Nk_B}{2}\ln(\frac{3}{2})$. This entropy arises from the special tetrahedron- shaped arrangement of the hydrogen and oxygen ions in water ice.

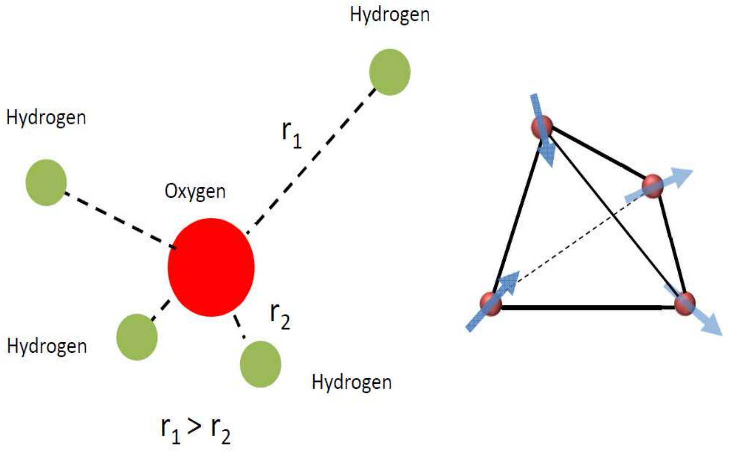

Figure 4.1: Configuration of protons and oxygen in water ice (left) and magnetic moments in spin ice (right). In water ice, each oxygen is bond to four hydrogens in a tetrahedral structure by two covalent ($r_2$) and two hydrogen ($r_1$) bonds in which $r_1 > r_2$. In spin ice the hydrogen atoms are replaced by magnetic ions and the distances $r_1$,$r_2$ are mapped to the direction of the magnetic moments.

In this arrangement, each oxygen ion is surrounded by four hydrogen ions, where two hydrogen ions are located closer to the oxygen than the other two (see Fig. 4.1).

In spin-ice materials, six of the $2^4 = 16$ possible spin configurations in each tetrahedron satisfy the spin-ice condition (2 in - 2 out state) (see Fig. 4.2). The calculated entropy from these spin configurations is similar to the entropy of water ice. Experimentally, it has been found, using specific-heat measurements that the entropy in spin-ice materials exhibits a residual entropy at 0 K similar to the entropy in water ice. Figure 4.3 displays the typical temperature dependence of the entropy of spin-ice materials. Over the past decade, it has been well

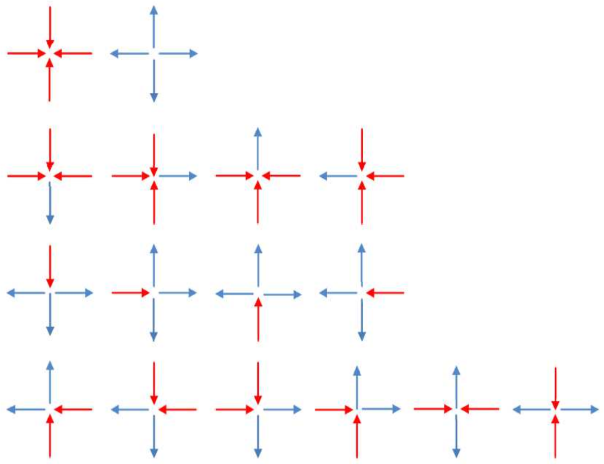

Figure 4.2: All possible spin configurations in the tetrahedral structure of spin ice. There are 6 equivalent configuration of 2 in - 2 out states, 8 configurations of 3 in - 1 out or 3 out - 1 in, and 2 configurations with all spins in or all spins out.

established that spin-ice materials obey the Pauling entropy, although recent investigations suggest that there exist some deviations [49].

The properties of spin ice are well described by a Hamiltonian with exchange, $J_{nn}$, and dipolar, $D_{nn}$, interactions [50] (Mathematical details of this Hamiltonian can be found in [4]). The effective interaction, $J_{eff}$, can be written as

$$J_{eff} = J_{nn} + D_{nn}. \tag{4.1}$$

The effective interaction in this kind of materials is dominanted by dipole-dipole interaction [5]. Nearest-neighbor-exchange interaction, $J_{nn}$, for HTO and DTO are –0.52 K and –1.24 K, respectively, and $D_{nn}$ is 2.35 K for both compounds [5]. Thus, $J_{eff}$ is positive for both materials with $J_{eff}$(HTO) = 1.8 K and $J_{eff}$(DTO) = 1.1 K. An Ising system can display spin-ice properties even for antiferromagnetic nearest–neighbor exchange interactions, $J_{nn} < 0$, as long as $J_{eff} > 0$. The theoretical phase diagram for spin ice, introduced by den

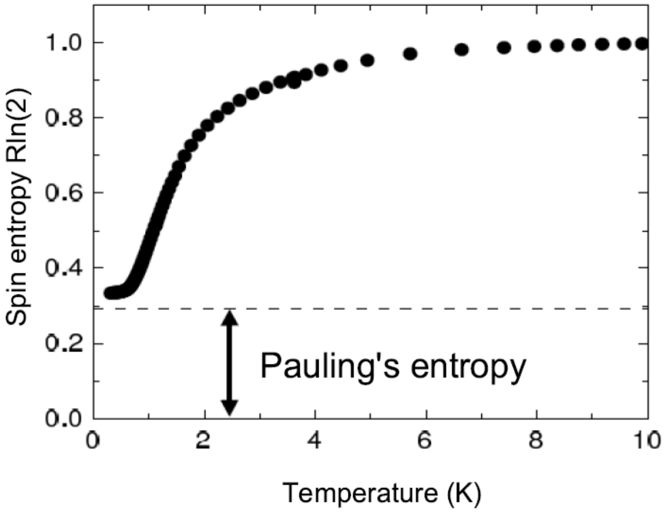

Figure 4.3: Temperature dependence of the magnetic entropy of spin-ice DTO obtained from specific-heat measurements exhibiting a Pauling residual entropy at 0 K [10]. If there would be no Pauling entropy, the entropy change from 0 to 10 K should be $R\ln(2)$.

Hertog and Gingras [50], indicates that for $\frac{J_{nn}}{D_{nn}} > -0.91$ a spin-ice state is stable. In HTO and DTO this ratio is –0.22 and –0.52, respectively. The magnetic dipole–dipole interactions dominate the exchange interaction and, therefore, the materials do not show long–range ordering even down to 50 mK [51, 52].

Spin-ice materials exhibit a number of peculiar low-temperature properties related to excitations out of the spin-ice ground state, which will be discussed in the next chapter.

## 4.2 Quantum effects in spin ice

In spin-ice materials with quantum fluctuations, there is a quantum–mechanical tunneling between different spin configurations of the spin-ice state (see Fig. 4.4) [6, 7, 53–55]. Such a state has a vanishing entropy at zero temperature, and so satisfies the third law of thermodynamics. In quantum spin ice quantum fluctuations are strong and, therefore, elementary excitations exhibit a different

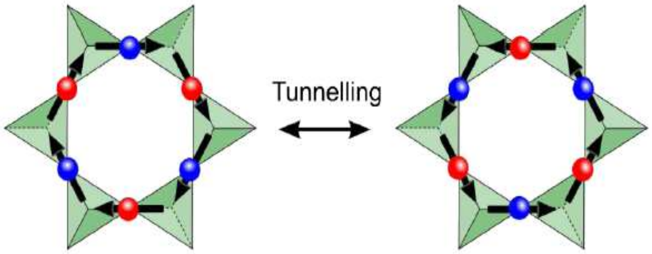

Figure 4.4: Quantum tunnelling of the system from one spin configuration to another. The main tunnelling is the reversal of a set of Ising spins with closed circulation on a 6–link hexagonal plaquette[6].

behavior than the ones in the spin ice. In the next section, we will discuss in more detail these excitations.

In spin ice, it has been shown that a magnetic field along [001] can cause a Kasteleyn transition from the Coulomb phase to an ordered phase where the spins are aligned with the field and fluctuations are suppressed [56–58]. For the corresponding quantum spin ice, this becomes a quantum phase transition from a Bose condensate to a vacuum state. The Kasteleyn transition in the spin-ice materials DTO and HTO will be discussed in the next section.

Neutron scattering and muon spectroscopy provide evidence that $Tb_2Ti_2O_7$ and $Yb_2Ti_2O_7$ are examples for quantum spin-ice materials [59]. Muon spin rotation reveals spin fluctuations down to the lowest temperatures.

## 4.3 $Dy_2Ti_2O_7$ and $Ho_2Ti_2O_7$

In recent years, several experimental studies have been performed in order to better understand the magnetic properties of HTO and DTO [60–72]. Concomitantly, some theoretical models have been developed to describe the obtained results. In this section, I briefly discuss on the reported experimental results using different experiments to probe various properties of spin ice. The spin-ice materials mostly have been studied using neutron scattering, specific-heat measurements, optical Raman spectroscopy, magnetization, ac susceptibility, thermal conductivity, Muon spectroscopy and magnetostriction.

Among the experiments listed above, multiple experimental techniques have been used to study relaxation processes in the spin ice. The spin-relaxation process in DTO shows an anomaly between approximately 5 - 13 K [73, 74]. At these temperatures, the magnetic-relaxation time is temperature independent (shows a plateau behavior) and deviates from the Arrhenius law [75, 76]. Recent investigations on the spin-ice material DTO have revealed that this deviation arises from diffusion of magnetic monopoles (the experimental data which have been explained in the context of magnetic monopoles is discussed separately in section 4.5) [74]. The relaxation of the magnetization at very low temperatures below 1 K, shows some freezing process [77]. The relaxation properties of HTO have been studied by use of AC-susceptibility measurements [78]. These measurements show with varying frequency two different processes on different time and energy scales.

The essential importance of dipolar interactions ( mentioned in the previous section) beyond the nearest neighbors in DTO and HTO has been suggested by susceptibility and neutron-scattering measurements [50, 51]. Moreover, magnetization and AC susceptibility of single crystals of the spin-ice compound DTO for field applied along [111] confirm a spin freezing below 0.5 K [66].

Non-equilibrium conditions and dynamics in spin ice have been studied by magnetization [79], ultrasound [80], and thermal-conductivity measurements [81]. However, the role of the lattice degrees of freedom in spin–ice materials has still to be thoroughly investigated. In the next chapter, non-equilibrium processes will be discussed in more detail.

Figure 4.5 exhibits the phase diagram of DTO extracted from magnetocaloric-effect measurements [60]. The zero-field state at low temperatures is 2 in-2 out (spin ice), also called frozen state. At non-zero fields, a Kagome-ice state exists up to 0.9 T for DTO and up to 1.5 T for HTO [57]. In this state, a conversion from the three-dimensional spin-ice configuration to a two-dimensional Kagome spin arrangement take place [82], where the applied field pins one spin per tetrahedron along the [111] direction, but since the field still is not strong enough, the three other spins rearrange in a way not to violate the ice rule. Therefore, in the Kagome-ice state the produced entropy by applying the magnetic field is finite [57]. The solid line in Fig. 4.5 shows a first–order transition from a low concentration of 3 in–1 out or 3 out–1 in states to a high concentration of 3 in-1 out or 3 out-1 in states in DTO. This ends at about 0.4 K. For HTO, a metamagnetic transition was found at the first-order transitions [83]. According to this experiment, a magnetization plateau is characteristic for Kagome ice.

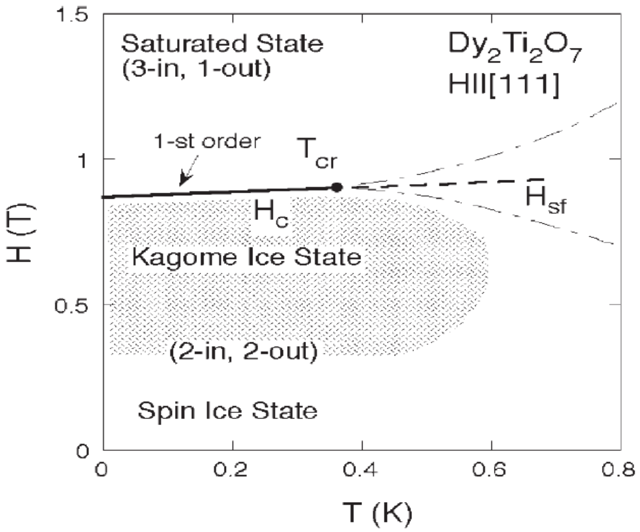

Figure 4.5: $T - \mu_0 H$ phase diagram of DTO for magnetic field along [111] [60].

As mentioned before, another transition occurring, when applying a magnetic field along the [100] direction in spin-ice materials is the symmetry-preserving Kasteleyn transition. This was concluded from analyzing magnetization data [56]. This has also been evidenced by neutron-scattering measurements [57].

The HTO and DTO display different properties in some experiments, due to strong hyperfine interactions in HTO. These interactions provide an additional heat bath in HTO, which can be identified by specific-heat measurement. Figure 4.6 shows measured specific heat data for HTO (open square) together with the estimated nuclear contribution (solid line) to the specific heat [52]. The nuclear component of the measured specific heat is estimated from the nuclear contribution obtained for $Ho_2GaSbO_7$ [52]. In this figure, open circles display the electronic component of the specific heat which is in agreement with theory (closed circle). The experimental data show that below 5 K the hyperfine interactions play an important role. Compared to HTO, such interactions are of importance in DTO only at much lower temperatures [84]. $\mu$SR results obtained on a polycrystalline DTO sample evidence remanent spin fluctuations at 20 mK, inside the spin–ice state. This phenomenon was attributed to the hyperfine interaction with the $^{161}$Dy and $^{163}$Dy nuclear spins [84].

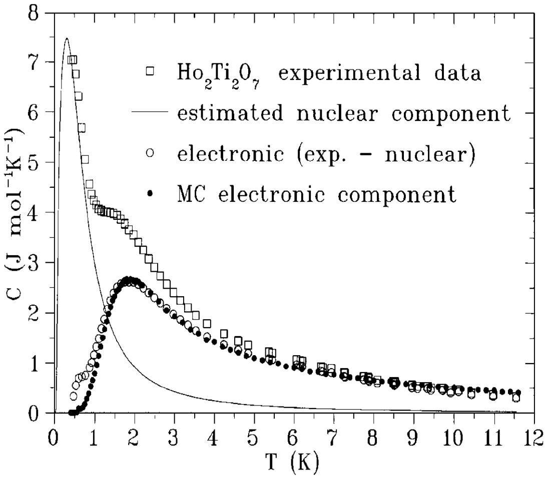

Figure 4.6: Experimental results and numerical simulation of the electronic and nuclear components of the specific heat in HTO [52].

In HTO and DTO the strong crystal electric field acting on the magnetic ions gives rise to an almost ideal classical Ising spin [85]. In spin-ice materials the spin–orbit coupling is dominant, so that free rare–earth ions are very well described in the basis of $|J, m_J\rangle$. In the cubic compound HTO, the $J = 8$ multiplet of the Ho$^{3+}$ ($4f^8$) ion splits into ten levels due to the D$_{3d}$ local symmetry [86, 87]. The ground state is known to be a $E_g$ doublet. Neutron scattering and optical experiments show that the first excited state of the CEF multiplet is well separated from the ground state. This separation from optical measurements is 104 cm$^{-1}$ or 150 K which is smaller than the 230 K obtained from neutron-scattering measurements. For DTO, the first excited state is separated from the ground state as observed for HTO. For this compound, the ground state is a $|15/2, \pm 15/2\rangle$ Kramers doublet [88, 89].

## 4.4 Magnetic monopoles

The theory of magnetic monopole started with a 1931 paper by Paul Dirac [8]. In this paper, Dirac showed that the existence of magnetic monopoles is consistent with Maxwell's equations only if electric charges are quantized. Dirac demonstrated the consistency of magnetic monopoles with quantum electrodynamics and some other physicists showed the necessity of monopoles in grand unified gauge theories [90, 91]. In later theories, magnetic monopoles appear in spontaneously broken unified gauge theories. Almost all theories agree that, if magnetic monopoles exist, they are too massive to have been produced in manmade radiation. Potentially, the existence of magnetic monopoles as a fundamental particle can be proved only by the detection of their signals from cosmic rays [90, 92–95]

After a few decades of searching for magnetic monoples in cosmic rays [8, 9, 90–100] or in lunar materials [101, 102], physicists have turned their attention to the search for monopoles in condensed matter. Magnetic monopoles in condensed matter are mainly considered as emergent quasiparticles. Topological insulators [103] and spin-ice materials were chosen as most promising candidates [4].

The monopoles in spin ice do not require a modification of Maxwell's equations. They do interact similar to the electric charges through Coulomb's law, but with magnetic origin. Therefore, it is called magnetic Coulomb's law [4].

## 4.5 Magnetic monopoles in spin ice

The most elementary excited state out of the spin–ice ground state can be achieved by a spin flip in a tetrahedron which violates the ice rule by a transition from a 2 in - 2 out state to 3 in - 1 out (or 3 out – 1 in) state (see Fig. 4.7). This excitation can be well described by a stretched magnetic dipole resembling solenoidal tubes (so called Dirac string) made of magnetic flux. At the ends of these tubes the resulting defects look like magnetic monopoles (see Figs. 4.7 and 4.8). These emergent quasiparticles are located in tetrahedra with 3 in - 1 out or 3 out – 1 in state and are connected via a Dirac string. One of the most prominent theoretical explanations of the Dirac string and this kind of magnetic monopoles (in spin-ice materials) is based on a dumbbell model. Figures 4.8 and 4.7 visualize magnetic monopoles and Dirac strings using the dumbbell picture of magnetic moments from different views. In this model, the magnetic dipoles located on a pyrochlore are replaced by dumbbells consisting of equal and opposite magnetic charges that sit at the ends of the dumbbell (The distance between the ends of a dumbbell is $a_d = \sqrt{3/2}a$, where $a = 3.54$ $\mathring{A}$ is the lattice constant for DTO) [4]. The magnetic charge can be calculated using the dumbbell model in spin-ice materials by $q_m = \pm 2\mu/a_d$, where $\mu$ is the magnetic moment[4]. Calculations based on the dumbblle model have revealed that the energy cost of separating of monopoles from one another approaches zero when the magnetic charges are separated by a few tetraheda in the crystal (see Fig. 4.9). Consequently, the magnetic monopoles in spin ice (in zero applied field)

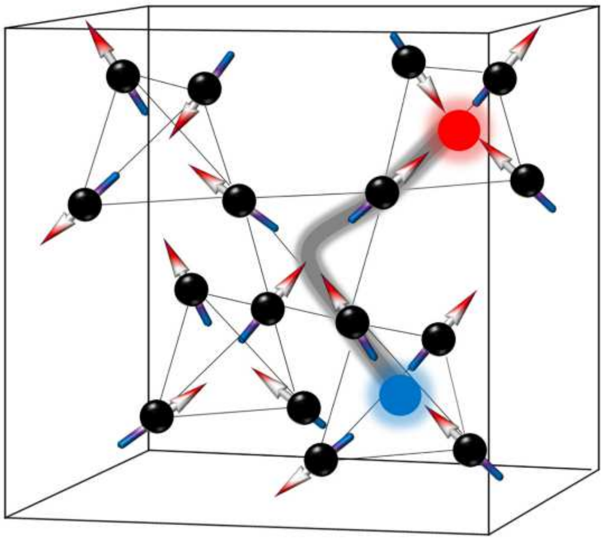

Figure 4.7: Cubic structure of spin ice and arrangement of magnetic monopoles connected to a Dirac string in tetrahedra with three spins pointing inward and one outward or vice versa. The intermediate tetrahedra between two monopoles, where the Dirac strings passes, remain in the spin-ice state (with two spins pointing inward and two spins outward of the tetrahedra).

can act as free particles on a random walk and Dirac strings have no preferential direction.

As mentioned above, a pair of magnetic monopoles in spin-ice materials, separated by the distance $r$, interact through a Coulomb law in the form of $\frac{-\mu_0 q_m^2}{4\pi r}$. The Coulomb interaction in the dumbbell model for spin ice is comprised of the magnetic Coloumb interaction and an entropic Coulomb interaction [4]. Entropic Coulomb interactions or entropic forces are phenomenological rather than microscopical forces which arise from the statistical tendency of the internal system to increase the entropy. This interaction vanishes at low temperatures. Therefore, the Coulombic interaction of magnetic monopoles has only a magnetic origin.

The Coulomb interaction of magnetic monopoles explains the results of heat-capacity measurements [4, 104]. Theoretical studies propose that two types of magnetic monopoles (free and bound magnetic monopoles) are created when the spin-ice state is entered from high temperatures. The free magnetic monopoles have a short lifetime as annihilation takes place when two monopoles meet each other, whereas the bound magnetic monopoles have a longer lifetime due to their confinement.

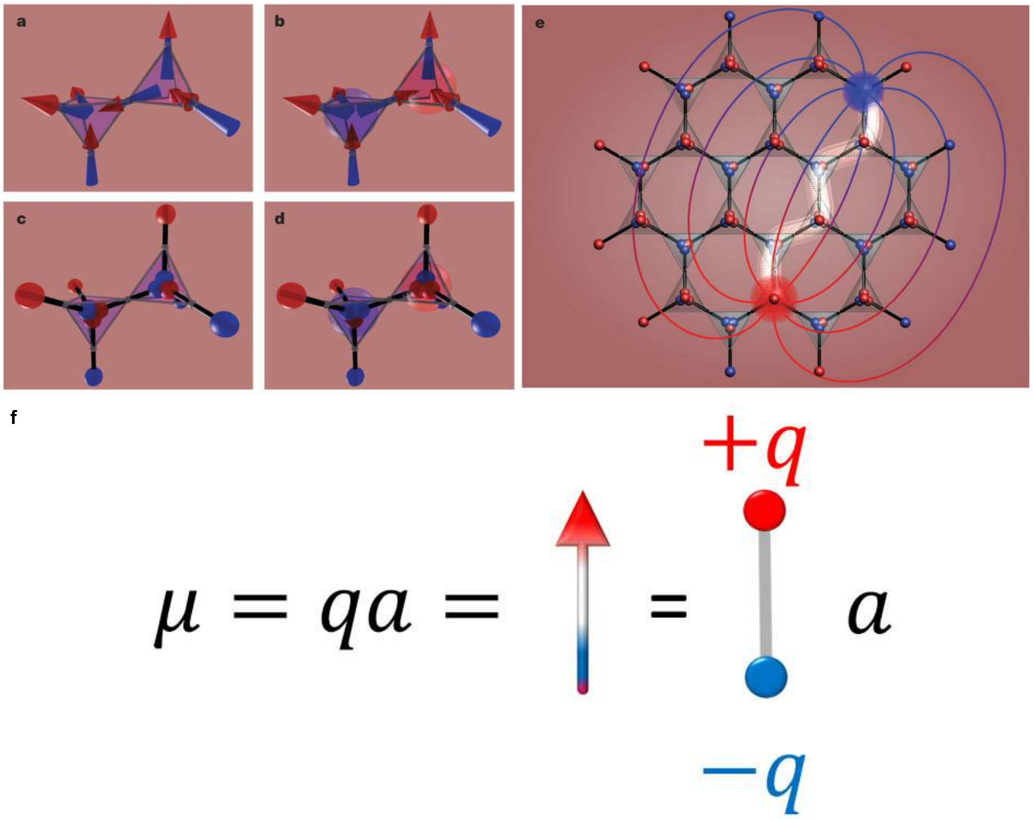

Figure 4.8: Magnetic moments in a pyrochlore lattice before and after a spin flip in two neighboring tetrahedra (a and b) replaced by dumbbells with oppositely signed magnetic charges (c and d). The terahedra before the spin flip in (a and c) are in the ice state, with two spins pointing in and two out, giving zero net charge on each tetrahedron. Inversion of the shared spin change the spin configurations to three spins pointing in and one out (or three spins pointing out and one in) generates a pair of magnetic monopoles (b and d). This configuration has a net magnetic moment on each tetrahedron. (e)The Dirac string and a pair of separated monopoles shown in a Kagome lattice (large red and blue spheres). Mapping of the magnetic moment to the dumbbell picture is shown in (f). $a$ is the dumbbell length or lattice constant [4].

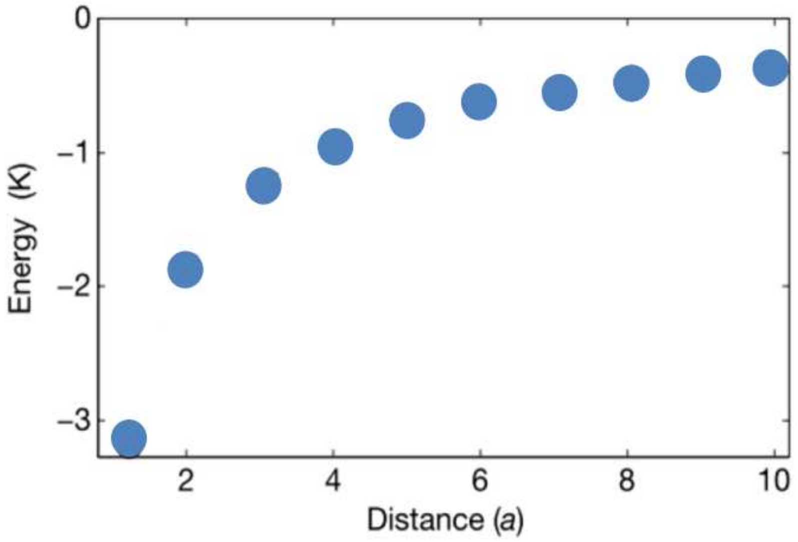

Figure 4.9: Numerical evaluation of the monopole-interaction energy in spin ice as a function of monopole separation in units of the lattice constant $a$ [4].

Some experimental studies and numerical calculations show that in spin ice the magnetic flux through the surface is nonzero [105]. Consequently, the divergence of the magnetization is also nonzero, i.e., $\nabla \cdot M \neq 0$, which implies that this region contains a positive or negative magnetic charge. The magnetic field produced by the magnetic charges is determined by an equation similar to Poisson's equation in electrostatics: $\nabla \cdot H + 4\pi \nabla \cdot M = 0 \Rightarrow \nabla \cdot H = 4\pi q_m$, where $q_m$ is a magnetic charge.

In addition, the presence of magnetic monopoles and Dirac strings in spin ice has been verified, by polarized neutron scattering [64]. It is worth to note that, Dirac strings are made out of magnetic flux and can interact with the magnetic moment of neutrons. Effects of this interaction can be seen as broadening of pinch-point features in the Brillouin zone at the points such as (0,0,2), (1,1,1) and (2,2,2) and so on (see Fig. 4.10) [64]. In addition, the Coloumb interaction of monopoles results in a dipolar-like decay of spin-spin correlations which can be Fourier transformed into pinch points as shown in Fig. 4.10. This experiment indicates that the mean free path of monopoles is restricted by proliferation of bond monopoles at finite temperatures (above 1.7 K) and free monopoles

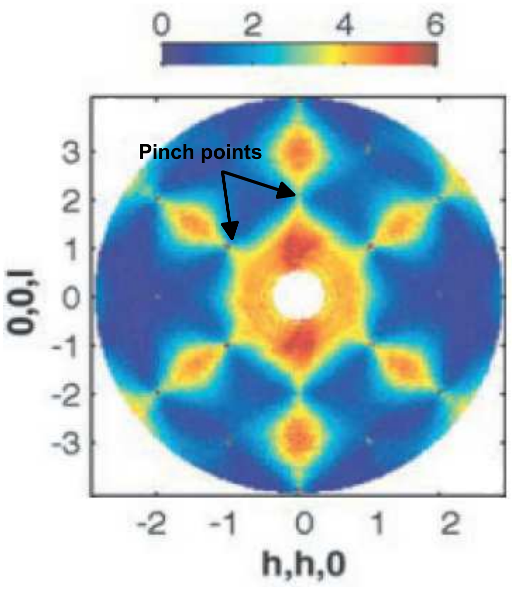

Figure 4.10: Polarized neutron-scattering map of spin ice, $Ho_2Ti_2O_7$. Arrows indicate two pinch points at (0,0,1) and (-1,-1,1) [64].

dominate at lower temperatures [64]. In addition, it can be inferred that the length of a Dirac string related to free monopoles can reach up to few hundred $\mathring{A}$ at lower temperatures.

### 4.5.1 Magnetic monopoles in the presence of quantum effects

The magnetic monopole behavior in quantum spin ice is puzzling, according to the obtained results on some quantum-spin ice compounds. As we discussed before, the effective interaction in spin ice is dominanted by dipolar interactions, while in quantum spin ice, the dipolar interaction is comparable to the exchange interaction. In quantum spin ice the phase transitions cannot be described by the gas-liquid transition paradigm. Instead, some possible phases and transitions may be explained by the Bose-Einstein condensation of magnetic monopoles. Another characteristic suggested for magnetic monopoles in quantum spin ice is the presence of an electric field and dynamical emergent photons due to the fluctuation of magnetic monopoles in the quantum-spin liquid phase (QSL). A magnetic monopole in this state corresponds to a “spinon” (or anti–spinon) excitation in the spin liquid [59].

Quantum strings in quantum spin ice, are reminiscent of Dirac strings in spin ice, that is the manifestation of weak quantum spin fluctuations with monopoles at their ends. In contrast to the Dirac strings in spin ice which are tensionless, strong quantum fluctuations in quantum spin ice make the strings tension negative and give rise to the deconfinement of monopoles [106]. In chapter 7 properties of magnetic monopoles in one of the quantum spin-ice compounds, $Yb_2Ti_2O_7$, will be discussed.

# 5 Low-field results

From this chapter to the end of the thesis, results of the ultrasound experiment on the spin-ice materials and their analysis will be discussed. This chapter is devoted to the investigation of low-energy field-induced properties of DTO and HTO in the context of magnetic monopoles with particular attention to some surprising phenomena such as non-stationary field-driven processes in DTO. In addition, we have analyzed the effects of a dynamical steady state on the field dependence of the sound attenuation in DTO.

I have studied the $c_{11}$ ($\mathbf{k} \parallel \mathbf{u} \parallel [001]$), $c_L = (c_{11} + 2c_{12} + 4c_{44})/3$ ($\mathbf{k} \parallel \mathbf{u} \parallel [111]$), and $c_T = (c_{11} + c_{44} - c_{12})/3$ ($\mathbf{k} \parallel [111]$, $\mathbf{u} \perp \mathbf{k}$) acoustic modes. I have also performed ultrasound measurements for the [112] direction ($\mathbf{k}\|\mathbf{u}\|[112]$). The applied magnetic field was directed along the sound-propagation direction. Most of the field dependences of the sound velocity and attenuation are reported for zero–field–cooled (ZFC) conditions.

The non-stationary processes observed in field sweeps in spin ice have been argued [79] to arise from the inability of the phonons to carry away the Zeeman energy released by the flipping spins when thermal runaway is triggered due to "supercooling". The supercooling arises when the sparseness of defects (monopoles) at low temperatures induces an exponentially slowdown of the dynamics [74, 79, 107]. I find that the sound velocity exhibits sets of well-defined spikes as the field is swept. Analyzing the shape of these peaks, which are highly asymmetric, taking into account the fundamentally distinct non-equilibrium mechanisms involved shows an "intrinsic" rise followed by an "extrinsic" fall, evidenced by a data collapse for various combinations of peak positions and sweep rates. The former involves the release of (Zeeman) energy from the spin system, the latter transfer of energy out of the sample.

In addition, for the case of an applied field in the [111] direction, we have found a very clear signature of a first-order gas-liquid-type transition, including the onset of hysteresis at the monopole "liquid-gas" transition [108]. Interestingly, the sound attenuation of the acoustic $c_T$ mode exhibits a sharp dip at this transition, manifesting a negative relaxation processes. This relaxation happens to some dynamical steady-state configuration of spins having higher energy than the lowest energy of the spins in the absence of sound waves. Such phenomena resemble an inverted pendulum in classical mechanics.

The chapter starts with a consideration of the field dependence of non–stationary processes in DTO. The sweep–rate effect in non–stationary properties of DTO is then discussed. A larger part of this chapter is devoted to the intrinsic and extrinsic processes in DTO. In the last section, anomalies of the acoustic characteristics at the first-order gas-liquid transition will be analyzed in the context of exchange-striction mechanism.

## 5.1 Results for $Dy_2Ti_2O_7$

As we discussed in section 2.5 the sound waves interact with magnetic ions mainly by two mechanisms, the exchange-striction and single-ion magnetoelastic interaction. In this section, the field dependence of the magneto-elastic interactions are explained by the exchange-striction mechanism. Non-stationary field-driven processes and the dynamical steady state at the phase transition will be described in the context of magnetic monopoles and exchange striction.

Figure 5.1 shows field-sweep data of the sound velocity and the sound attenuation for the acoustic $c_T$ mode measured at various temperatures. Several peaks appear in both acoustic characteristics below 0.5 T in the temperature range between 0.29 and 0.45 K. (The acoustic $c_{11}$ and $c_L$ modes show similar features). In addition, there is an abrupt drop of the sound velocity and an anomaly in the attenuation occurring at 1.25 T. It turns out that the attenuation of the longitudinal mode $c_L$ (see the inset in the lower panel of Fig. 5.2) does not reveal any feature at 1.25 T, while the low–field peaks are present. All features disappear completely at higher temperatures, $T \geq 0.5$ K.

In a next step, I measured the field dependence of the sound velocity using sweep rates in the range from 0.015 to 0.15 T/min at $T=$ 0.29 K (see Fig. 5.2). This reveals a changeover from narrow peaks to broad peaks by increasing the sweep rate. The maximal height of the peaks for various sweep rates was quite comparable for all peaks. The number of peaks varies little for different sweep rates (Fig. 5.2). With increasing sweep rate (and thus peak width), the separation between the peaks decreases, so that peaks merge for large sweep rates; also the positions of the maxima are shifted in field; a clear sign for their non-equilibrium nature. A further indication that we are not probing equilibrium spin configurations is provided by a thermometer installed on the sample which shows a change of temperature at the values of the field where the peaks of the sound velocity appear [80] (inset of Fig.5.2). Due to the nature of the thermometer's contact, the absolute scale of the temperature spikes is likely to be understated. The change of sound velocity, thus, in large part arises from the change in the temperature of the sample at these values of the magnetic field.

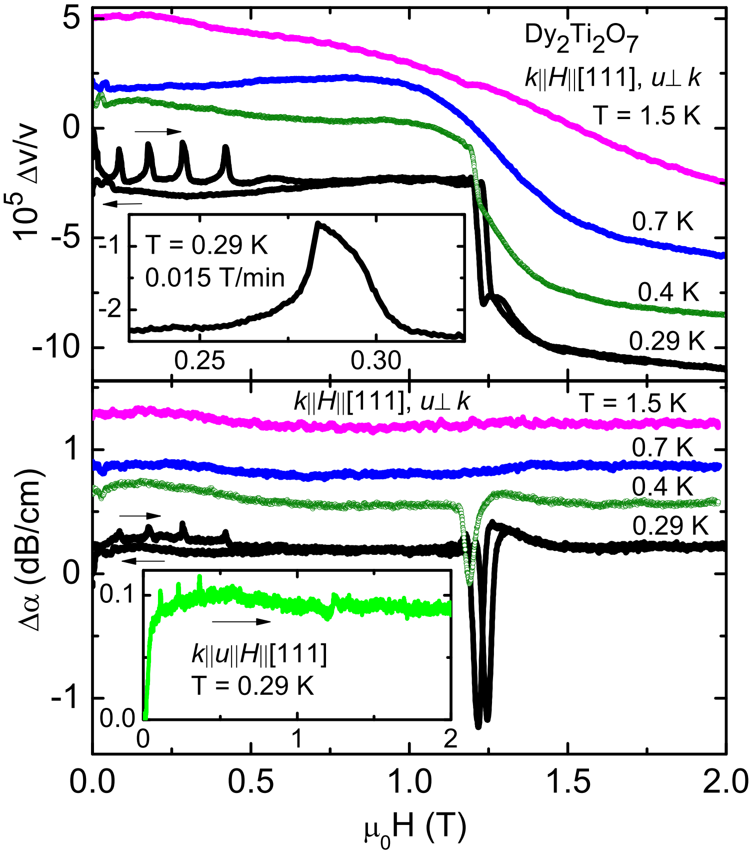

Figure 5.1: Field dependence of the sound velocity, $\Delta v/v$, (top) and the sound attenuation, $\Delta\alpha$ (bottom) of the transverse ultrasonic wave propagating along the [111] ($k\|H\|[111]$ and $u\perp k$) direction (acoustic $c_T$ mode) at different temperatures measured for zero-field-cooled ZFC condition. Results for up and down field sweeps (indicated by arrows) are shown for the lowest temperature of 0.29 K. The data for different temperatures are arbitrarily shifted along the y axis for clarity. The upper inset shows some details for a single peak in the sound velocity. The field dependence of the sound attenuation for the longitudinal mode (acoustic $c_L$ mode) at 0.29 K is given for comparison in the lower inset. Only the $c_T$ mode demonstrates a sharp attenuation anomaly at about 1.25 T.

The phonons thus provide an in–situ thermometer. However, additional experimental and theoretical work is required in order to convert the sound–velocity change quantitatively into a temperature change.

In the previous chapter, some properties of magnetic monopoles in spin ice have been described. Tetrahedra violating the ice rules appear as point-like defects experiencing a mutual *magnetic* Coulomb interaction $\frac{\mu_0 q_m^2}{4\pi r}$, where $q_m \approx 4.6\mu_B/\text{Å}$ is the effective magnetic charge of the monopoles. Single spin flips are only possible at low temperature when they correspond to the motion of monopoles - otherwise they are suppressed by an exponentially small Boltzmann factor, $\exp[-\Delta/T]$, with $\Delta \approx 4.3$ K. This leads to a strong slowdown of the dynamics below $T_f \approx 500 - 600$ mK [56, 64, 107].

As a result, at low $T$, field sweeps drive the system out of equilibrium: The magnetization change demanded by the changing field cannot be established sufficiently fast. Instead, "reequilibration" can occur in the form of avalanches with the temperature rising up to $T_f$ [79], which show up as the peaks in the measurements of the sound velocity. Figure 5.3 depicts schematically the avalanche process of the magnetic monopoles in two dimensions.

With this at hand, let us analyze these peaks in more detail. As a starting point, note that when the peaks are well developed (e.g., for the slow sweep rate, 0.015 T/min), their overall shape is almost independent of the field at which the peak is triggered (Fig. 5.4, bottom). Although I have observed the sound-velocity and the sound-attenuation peaks already at 0.015 T/min (the magnetization jumps were detected only above 0.025 T/min [79]) stopping a field sweep exactly at the sound-velocity peak position leads to a relaxation of the sound velocity (and the temperature) to the value characteristic of the valleys between the peaks (not shown), meaning that for much slower sweep rates the peaks should disappear (in agreement with Ref. [79]). This can also explain the broadening of the ultrasound features for the faster field sweeps when the relaxation time approaches the sweep time between the adjacent peaks (see Fig. 5.4).

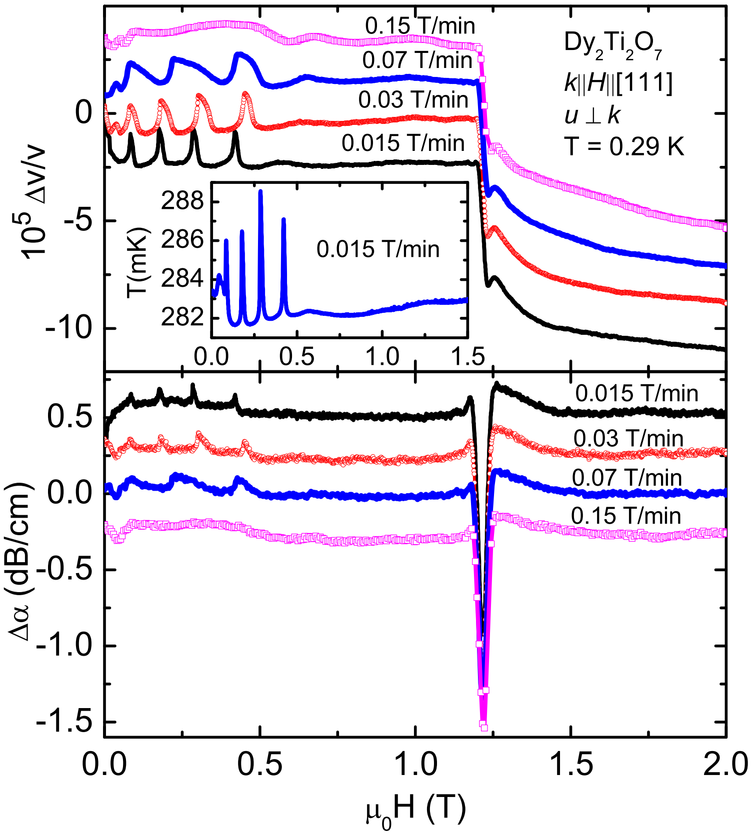

Figure 5.2: The sound velocity (top) and the sound attenuation (bottom) of the $c_T$ acoustic mode measured at 0.29 K and various field-sweep rates. All data were obtained under ZFC condition. The data curves are arbitrarily shifted along the y axis for clarity. The inset shows the temperature change, measured during an up field sweep by a $RuO_2$ thermometer directly attached to the sample.

## 5.2 Intrinsic and extrinsic nature of the non-stationary processes

Comparing different sweep rates unearths a surprising feature: there appear to exist two qualitatively different regimes. To illustrate this statement the left panels of Fig. 5.4 show the rising parts of the sound-velocity peaks with different field-sweep rates (top) and for different peaks (bottom) as a function of the applied field, while in the right panels the descending parts of peaks and the temperature are plotted as a function of time. The rising parts for the $c_T$ mode are plotted as well as the descending part for the $c_L$ mode for different sweep rates, for which the collapse is most prominent; the peak shapes of the two modes behave a little different from each other. Scaling is evident in both panels.

The explanation of the scalings is as follows. The external magnetic field drives the motion of a small number of thermally activated monopoles in DTO (which leads to a small response rate). For the system's state to keep up with the changing field, more monopoles need to be created so that spins can be flipped at a higher rate. However, energy barriers arise, from a competition between the Zeeman energy gain and the cost of creating and separating monopoles, and perhaps also from disorder. Hence, the response has mostly intrinsic character in that it involves a distribution of magnetic energy barriers and not other degrees of freedom such as phonons. The energy released due to the growing number of monopoles moving along the field does not leave the sample quickly, leading to local heating (cf. Fig. 5.2) resulting in an avalanche [79]: More monopoles get thermally activated, more Zeeman energy is thus released etc.

On the other hand, the descending parts of the peaks in the sound velocity, i.e., the release of the energy to the outside world, are different in nature: The collapse of the curves as a function of time (regardless of field strength) is consistent with the heat simply disappearing through a thermal contact. Indeed, the tail of the peak fits well to an exponential fall-off with a timescale of roughly a minute. Crucially, the shape of the temperature traced by the thermometer follows this peak decay quite closely, much more so than on the rising side, where the temperature notably lags behind the sound velocity's rise.

Two final remarks on the low-field regime are in order. First, the ultrasound results crisply complement neutron scattering [72] and the recent magnetization [79] results on non–stationary field sweeps, particularly by providing a detailed and time-resolved focus on the nature of the thermal runaway and subsequent cool–down.

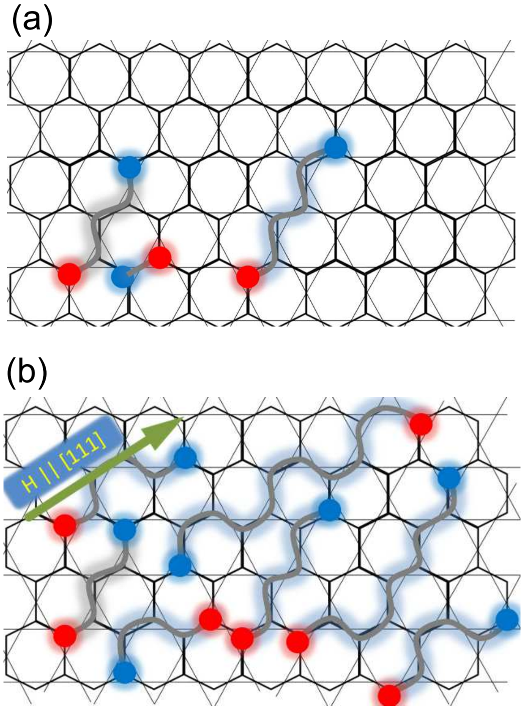

Figure 5.3: Schematically shown monopoles in a Kagome plane (a) before and (b) after triggering an avalanche of monopoles.

Second, recent studies [4, 109] of the monopole dynamics in DTO at low temperature suggest that there exist several regimes of monopole relaxation in spin ice, in particular, with slow dynamics below $T_f$. From Fig. 5.4, we observe that the relaxation of the sound velocity to the value characteristic of the valleys between peaks is about a minute, in the same ballpark but somewhat shorter than the monopole lifetime extracted in Ref. [109], $\sim 150$ s. Notice, however, that relaxation times are observed to be field dependent

Next, I turn to the strong-field regime, where there is a monopole liquid-gas transition in spin ice. This takes place between the Kagome-ice regime and the saturated state, which have a low and high density of monopoles, respectively, see Refs. [4, 67, 110] for details. For our purposes it is enough to note that the magnetic field applied along the [111] direction acts as a staggered chemical potential for the monopoles [4]. At low temperature, the monopole density exhibits the discontinuous jump of a first-order transition, whereas there is a continuous crossover at higher temperature. A critical endpoint separates the two phases [60].

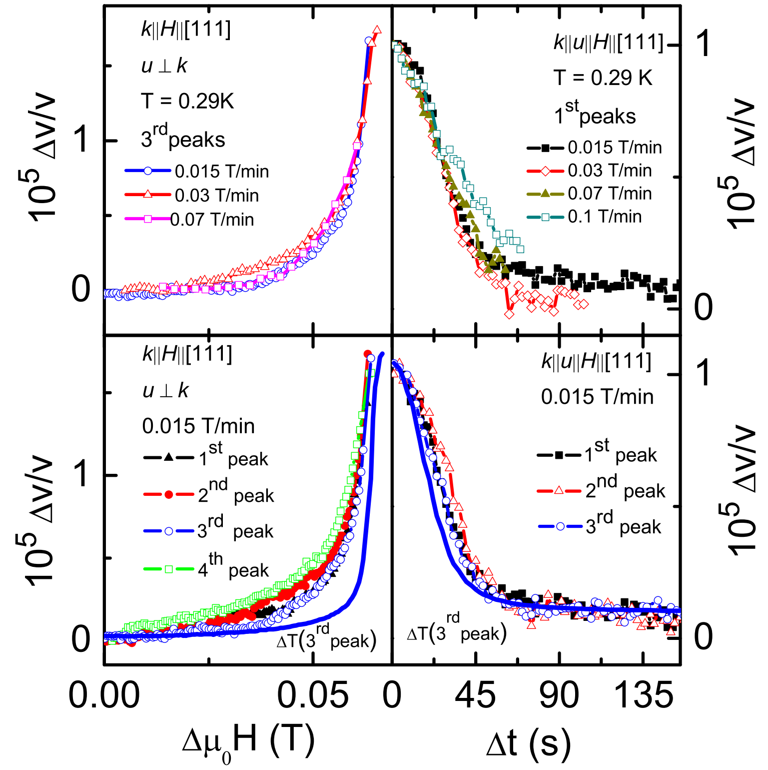

Figure 5.4: Behavior of the rising parts (left) of the sound-velocity peaks of the acoustic $c_T$ mode for different sweep rates (upper panel) and different peaks (lower panel) as a function of magnetic field at $T = 0.29$ K. The right panels show the descending parts of the velocity peaks for the acoustic $c_L$ mode as a function of time. The blue solid lines are uncalibrated temperature traces.

The values measured here values for the critical field, $H_c$, agree with the value $H_c \sim 1.25$ T, observed via neutron scattering [57], however, they disagree with $H_c \sim 0.93$ T, observed in magnetocaloric and magnetization experiments [60, 108]. Anomalies are detected in specific-heat measurements at both $\sim 1$ T and $\sim 1.25$ T for $T < 0.3$ K [51]. A careful estimation of the demagnetization effect in my experiments leads to a corrected value of $H_c = 0.96 \pm 0.04$ T which is very close to that obtained in [60, 108]. We also see an onset of the hysteresis, clearly visible at $T = 0.29$ K (Fig. 5.1) but not at $T = 0.7$ K. In between, at $T = 0.4$ K, $\Delta v/v$ is very steep, suggesting proximity to the critical endpoint.

In passing, it is noted that our results indicate that the exchange interaction in DTO is not direct. This is suggested by the fact that the sound attenuation at $H_c$ is stronger in the transverse mode than in the longitudinal one, given that

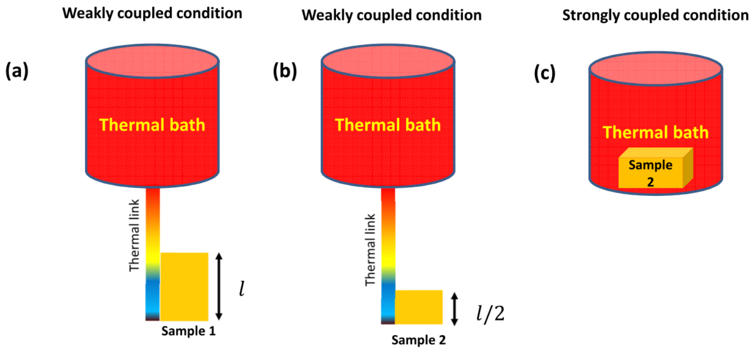

Figure 5.5: Schematic picture of the experiment under weak and strong coupling to the thermal bath for sample 1 and sample 2. These samples have different demagnetization factors for different lengths of $l$ and $l/2$. In (a) and (b), both samples 1 and 2 were investigated in a weakly coupled condition and in (c) the experiment has been carried out with sample 2 under strongly coupled condition.

the leading contribution to the exchange-striction coupling is proportional to the scalar product of exchange gradient and the sound polarization [111].

So far, I investigated the non-stationary processes in the spin-ice state in DTO at various temperatures with sweeping the magnetic field at different rates. It is known that the appearance of these processes strongly depends on the adiabatic conditions during the experiment. To explore the influence of the heat exchange between sample and environment, I performed experiments for two different sample-bath coupling conditions (see Fig. 5.5). In one experiment, the sample was located in the $^3$He-$^4$He liquid of a dilution refrigerator as shown in Fig. 5.5c (strong thermal coupling) and in the second experiment, the sample was attached to a $^3$He chamber via a thermal link (Figs 5.5a and b). The latter case leads to a weaker coupling to the bath, still providing a reliable temperature control of the sample. I further took into account the demagnetization factors of the samples to trace how they affect the obtained results.

In Fig. 5.6, the sound velocity and sound attenuation of the acoustic $c_T$ mode in two DTO samples with different demagnetization factors and for the described bath-coupling conditions are shown as a function of magnetic field. The data were collected at 20 mK (strong-thermal coupling condition) and 0.29 K (both strong and weak thermal coupling). In addition, at 0.29 K, data for two samples

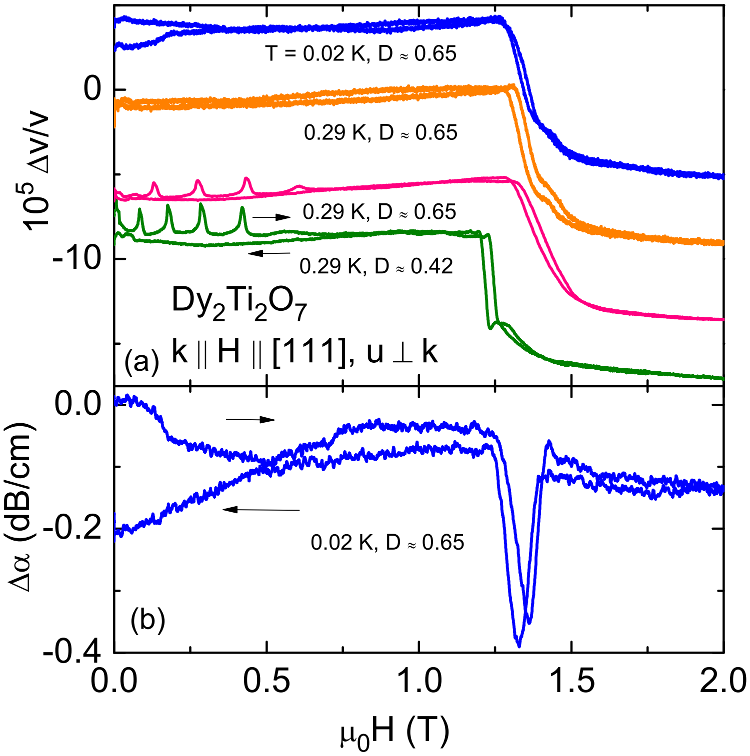

Figure 5.6: Field dependence of (a) the sound velocity, $\Delta v/v$, and (b) the sound attenuation of the $c_T$ mode. The upper two curves in (a) were obtained in dilution refrigerator, whereas the lower two curves were measured in a $^3$He cryostat (see text for details). Up and down sweeps are indicated by arrows. The ultrasound frequencies were 108, 108, 183, and 170 MHz from the upper to lower curve, respectively. The field sweep-rate was 0.015 T/min except for the sample with $D = 0.65$ at 0.29 K, which was 0.03 T/min. The curves are arbitrarily shifted along the $y$ axis for clarity.

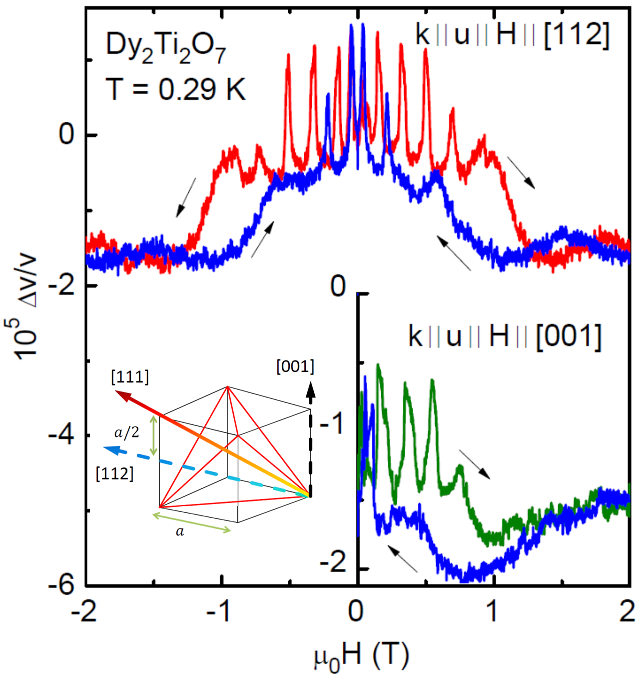

Figure 5.7: Field dependence of the sound velocity, $\Delta v/v$, for different field- and sound-propagation directions at 0.29 K. The upper curve shows, $\Delta v/v$, for a longitudinal ultrasonic wave propagating along [112] ($c'_L$ mode). The magnetic field first was swept to 2 T, then to -2 T and back to 0. The lower right panel shows demonstrates, $\Delta v/v$, for the $c_{11}$ mode propagating along the [001] direction. The sound frequencies in case of [001] and [112] were 64.5 and 86 MHz, respectively. Inset: Various crystallographic directions mapped on a single tetrahedron of the pyrochlore structure are shown.

with 2 different demagnetization factors, $D = 0.42$ (sample 1, also used in Ref. [80]) and 0.65 (sample 2) are shown. The second sample was prepared from the first one by cutting the crystal parallel to the (111) plane. The corresponding demagnetization factors are estimated for the magnetic field applied along the [111] axis.

For the weaker thermal coupling (lower two curves in Fig. 5.6a), a number of quasi-periodic peaks in the sound velocity appear similar to the peaks presented in Figs. 5.1 and 5.2 [80] which signal non-equilibrium processes in the spin-ice state. For the different demagnetization factors, the peaks are somewhat shifted in field and reduced in amplitude (mainly due to the different masses

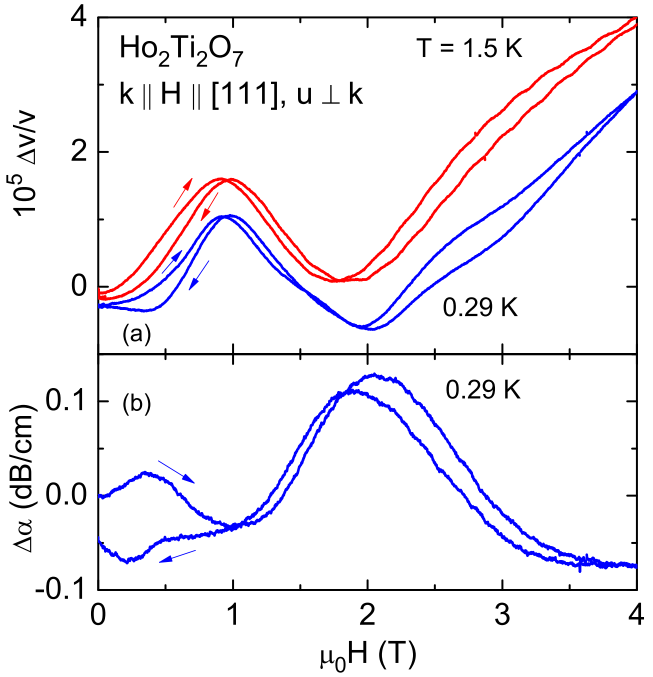

Figure 5.8: Field dependence of (a) the sound velocity, $\Delta v/v$, and (b) sound attenuation, $\Delta\alpha$, of the transverse $c_T$ mode propagating along the [111] direction for 0.29 and 1.5 K. The ultrasound frequency was 181 MHz. Arrows indicate field-sweep directions.

and heat capacities), but the overall picture is unchanged. The main effect of the increased demagnetization factor is the expected slight increase of the gas-liquid-type transition in field from about 1.25 T for $D = 0.42$ to approximately 1.35 T for $D = 0.65$.

The non-equilibrium peaks disappear when sample 2 is strongly coupled to the thermal bath (upper two curves in Fig. 5.6a). Obviously, here the heat release caused by the field-induced monopole avalanches is thermalized much faster than our sound-velocity measuring time.

At the lowest temperatures (0.02 K), we observe a pronounced hysteresis below 0.3 T, that is absent at 0.29 K (Fig. 5.6a). A strong hysteresis also appears in the sound attenuation at 0.02 K (Fig. 5.6b). In addition, a sharp and quite unique dip occurs at the gas-liquid transition at 1.35 T. This may be considered as a kind of sound amplification and is discussed in section 5.3.

In order to explore the nature of the field induced phase transition and the non-equilibrium features appearing in the spin-ice state further, I have measured other acoustic modes in DTO. Figure 5.7 shows the field-dependent sound velocities at 0.29 K of the $c_{11}$ and $c'_L$ modes for the magnetic field applied along [001] and [112], respectively. For the latter case, the magnetic field was first swept up to 2 T, then reversed to -2 T and back to 0. The experimental curves are very symmetric with respect to $H = 0$ T. For both sound modes, large hystereses are found. The gas-liquid transition is not so clearly resolved as for the $H \| [111]$ mode (Fig. 5.6). The non-equilibrium peaks, however, are nicely observed also for these modes and field directions in the weak thermal-coupling condition ($^3$He cryostat). Indeed, the same number of peaks appear in the up sweeps for all field directions.

For comparison, we investigated the field-dependent sound velocity and attenuation of the $c_T$ mode in HTO as well (Fig. 5.8). For 0.29 K and 1.5 K, the sound velocity exhibits a maximum at 1 T and a minimum at higher fields. This minimum shifts from about 2 T at 0.29 K to 1.8 T at 1.5 K. Concomitantly, the sound attenuation shows a noticeable peak at about 2 T at 0.29 K associated with the gas-liquid transition. The corresponding critical fields are in good agreement with the transition obtained by Fennell *et al.* [64] from neutron-scattering and magnetization measurements performed at 0.51 K. Sharp slope changes in the magnetization are also observed at approximately the same magnetic field (see below) [63, 65].

In HTO, however, we do not observe any non-equilibrium peaks due to monopole avalanches. If present, relaxation to equilibrium is too fast to be detected in our experiment; such fast relaxation channels maybe provided by nuclear Ho spins in HTO [5].

The static-field measurements of the sound velocity and attenuation for the acoustic $c_L$ mode were extended to higher fields up to 10 T (see Fig. 5.9). Comparison of the results reveals some additional anomalies for both compounds. Between 2 and 7 T, only a weak oscillatory behavior in the sound velocity of DTO is found. Above this field the sound velocity drastically shows hardening resembling the hardening behavior of the sound velocity in HTO above 2 T.

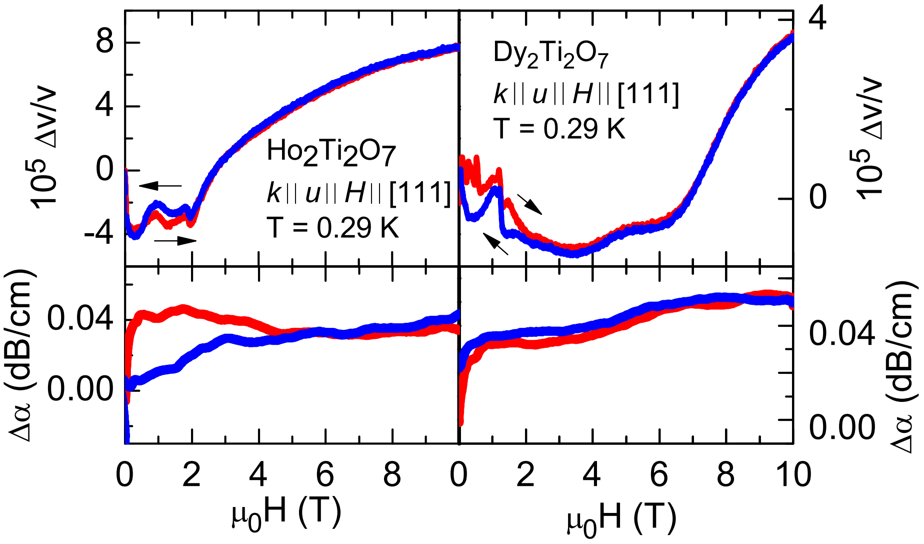

Figure 5.9: Field dependence of the sound velocity and the sound attenuation up to 10 T in DTO (tight)and HTO (left) for $c_L$ mode.

## 5.3 Analysis based on the exchange-striction coupling

The renormalization of phonon velocities and sound attenuations in magnetic media for a stationary situation are caused mostly by two reasons [17]. First, sound waves change the ligand positions, and, therefore, the crystalline electric field of the ligands is affected. Due to strong spin-orbit interaction, the latter produces changes of the single-ion magnetic anisotropy of the rare-earth ions (detailed description can be found in Sec. 2.5.1). This should also change the effective $g$-factors of the rare-earth ions and thus, due to magneto-elastic interactions, the sound waves can change the directions of the magnetic anisotropy slightly, and vice versa, the magnetic anisotropy modifies the sound-wave parameters, such as the sound velocity and attenuation. This interaction between the sound wave and the magnetic properties exists at all temperatures lower than the characteristic energy of the single-ion magnetic anisotropy.

On the other hand, sound waves change the magnetic-ion positions themselves and/or the positions of nonmagnetic ions involved in the superexchange between magnetic ones. In this case, the sound waves renormalizes the effective exchange (as well as dipolar) interactions between magnetic ions. The manifestation of this effect is more pronounced compared to the influence of the sound on the single-ion magnetic properties, because the inter-ionic magnetic and exchange interactions predominantly determine magnetic phase transitions.

In DTO and HTO, the single-ion anisotropy is of the order of 300 K (The results related to this effect will be discussed in the next chapter). This is why we expect that the sound-mode changes at low temperatures are mostly related to the renormalization of inter-ionic magnetic interactions due to the spin-phonon coupling. To describe the features of the sound in DTO and HTO the approach used in Refs. [112, 113] is adapted. It should be mentioned, that the calculations in this section kindly have been done by A. A. Zvyagin. The relative renormalization of the longitudinal sound velocity can be written as (in this section the notations in which $g_{\mathrm{J}}\mu_{\mathrm{B}} = k_{\mathrm{B}} = \hbar = 1$ are used)

$$
\begin{aligned}
\frac{\Delta v}{v} &= -\frac{(2|G_0(\mathbf{k})|^2\langle S_0\rangle^2\chi_0 + T\sum_{\mathbf{q}}\sum_{\alpha=x,y,z}|G^{\alpha}_{\mathbf{q}}(\mathbf{k})|^2(\chi^{\alpha}_{\mathbf{q}})^2}{(N\omega_{\mathbf{k}})^2} \\
&-\frac{H_0(\mathbf{k})\langle S_0\rangle^2 + \frac{T}{2}\sum_{\mathbf{q}}\sum_{\alpha=x,y,z}H^{\alpha}_{\mathbf{q}}(\mathbf{k})\chi^{\alpha}_{\mathbf{q}})}{(N\omega_{\mathbf{k}})^2}.
\end{aligned}
\tag{5.1}
$$

Here, $N$ is the number of spins in the system, $\omega_{\mathbf{k}} = vk$ is the low-$k$ dispersion relation for the phonon with sound velocity $v$ in the absence of spin-phonon interactions, $\langle S_0\rangle$ is the average spin moment (related to the magnetization) along the direction of the magnetic field, $H$, $\chi^{x,y,z}_{\mathbf{q}}$ are non-uniform magnetic susceptibilities, and the subscript 0 corresponds to $q = 0$. The renormalization is proportional to the spin-phonon coupling constants (which have to be determined independently),

$$
\begin{aligned}
G^{\alpha}_{\mathbf{q}} &= \frac{1}{m}\sum_{n} e^{i\mathbf{q}\mathbf{R}_{nm}}\left(e^{i\mathbf{k}\mathbf{R}_{nm}}-1\right)\mathbf{e}_{\mathbf{k}}\frac{\partial J^{\alpha}_{mn}}{\partial \mathbf{R}_m}\ , \\
H^{\alpha}_{\mathbf{q}} &= \frac{1}{m}\sum_{n} e^{-i\mathbf{q}\mathbf{R}_{nm}}\left(e^{i\mathbf{k}\mathbf{R}_{nm}}-1\right)\left(e^{-i\mathbf{k}\mathbf{R}_{nm}}-1\right)\times \\
&\mathbf{e}_{\mathbf{k}}\mathbf{e}_{-\mathbf{k}}\frac{\partial^2 J^{\alpha}_{mn}}{\partial \mathbf{R}_n \partial \mathbf{R}_m}\ .
\end{aligned}
\tag{5.2}
$$

Here, $m$ is the mass of the magnetic ion, $J^{\alpha}_{mn}$ denote (generally anisotropic) effective exchange integrals, $\mathbf{e}_{\mathbf{k}}$ is the polarization of the phonon with wave vector $\mathbf{k}$, $\mathbf{R}_n$ is the position vector of the $n$-th site, and $\mathbf{R}_{nm} = \mathbf{R}_n - \mathbf{R}_m$. Following Refs. [112, 113] we can calculate the attenuation coefficient

$$
\begin{aligned}
\Delta\alpha(\equiv \Delta\alpha_k) &= \frac{1}{Nv}\Big[2|G_0(\mathbf{k})|^2\langle S_0\rangle^2\chi_0\frac{\gamma^z_0}{(\gamma^z_0)^2+\omega^2_{\mathbf{k}}} \\
&+T\sum_{\mathbf{q}}\sum_{\alpha=x,y,z}|G^{\alpha}_{\mathbf{q}}(\mathbf{k})|^2(\chi^{\alpha}_{\mathbf{q}})^2\frac{2\gamma^{\alpha}_{\mathbf{q}}}{(2\gamma^{\alpha}_{\mathbf{q}})^2+\omega^2_{\mathbf{k}}}\Big]\ ,
\end{aligned}
\tag{5.3}
$$

where $\gamma_{\mathbf{q}}^{\alpha}$ are the relaxation rates, which can be approximated by $\gamma_{\mathbf{q}}^{\alpha} = B/T\chi_{\mathbf{q}}^{\alpha}$, where $B$ is a material-dependent constant (see Ref. [111]). In the calculations the approximation was used, in which the relaxation rates do not depend on the direction and on the wave vector.

Hence, according to this approach, the renormalization of the sound velocities and attenuation due to the magneto-elastic interaction, is related to the behavior of the magnetization (total spin moment) and the magnetic susceptibility, affected by the effective exchange interactions between the rare-earth magnetic ions in DTO and HTO. One can calculate the temperature and magnetic-field dependences of the total spin moment and magnetic susceptibility of DTO and HTO using a recently developed approach, [114] in which the Bethe-Peierls approximation on a Bethe lattice was used.

Obviously, in this approximation one can use only homogeneous contributions from the spin moment and susceptibility to the renormalization of the sound velocity and attenuation.

Let us consider two directions of the magnetic field, related to the experiments, namely [111] and [100] (the direction of the field along [112] has properties, very similar to the one along [111]). It is important to note that for both field directions the results depend [114] on the thermal history ("field cooling" or "zero-field cooling").

Let us start with the field direction along [111]. To find the temperature dependence of the renormalization of the sound velocity and sound attenuation in zero magnetic field (i.e., zero-field cooling), one can take into account that under such condition $\langle S_0 \rangle = 0$ and $\chi \equiv \chi_0 = 2/3T$. Then, Eqs. (5.1)-(5.3) yield

$$\begin{aligned} \frac{\Delta v}{v} &\approx -\frac{1}{3(N\omega_{\mathbf{k}})^2}\left(\frac{4|G_0(\mathbf{k})|^2}{3T} + H_0(\mathbf{k})\right) , \\ \Delta\alpha &\approx \frac{48|G_0(\mathbf{k})|^2 B}{9NvT(36B^2 + 4\omega\mathbf{k}^2)} , \end{aligned} \tag{5.4}$$

i.e., both the renormalization of the sound velocity and attenuation are inversely proportional to the temperature. Of course, Eqs. (5.2) imply that changes in the velocity of the longitudinal sound have to be, generally speaking, larger than for the transverse sound. Notice, that one has to take the numerator of the second term in Eq. (5.1) as a negative value to describe the experiments.

A qualitative explanation of the "negative relaxation" can be the following. For spin-ice systems in the absence of an external field the ground state is highly degenerate. Under the influence of the sound the degeneracy can be locally lifted. It is possible then that the relaxation is not to the configuration with

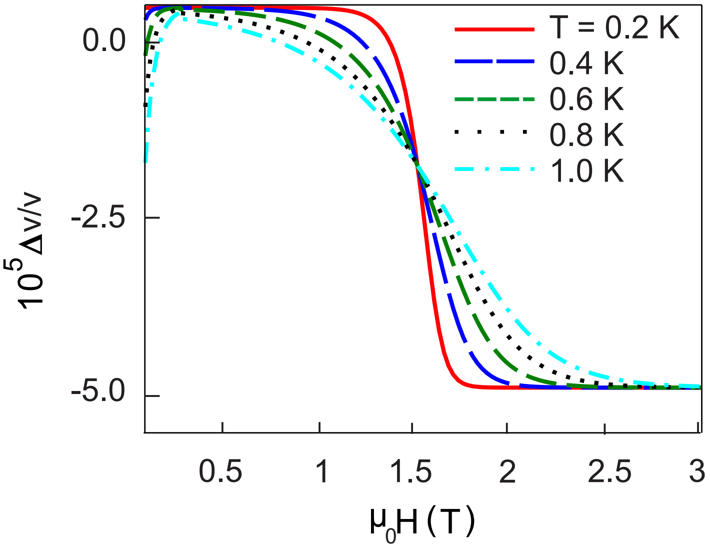

Figure 5.10: Calculated magnetic-field dependence of the relative change of the sound velocity, $\Delta v/v$, at different temperatures for the field applied along the [111] direction.

the lowest energy, which has to be positive, but to some dynamical steady-state configuration of spins with energy higher than the lowest energy of spins in the absence of sound (cf. Ref. [115], where the relaxation of parametrically excited magnons in the spin system was to the dynamical steady-state configuration of spins, which had higher energy in the absence of parametric pumping), which can yield effective "negative relaxation".

Figures 5.10 and 5.11 show the calculated magnetic-field dependences of the sound velocity and attenuation at several temperatures. The sound velocity shows a step-like feature at a critical magnetic field, while the attenuation shows a deep minimum, in agreement with our experiment (Fig. 5.6).

At about 1.5 T, directed along [111], the magnetization jumps from 1/3 to 1/2 of the saturation value. As the temperature increases, these features smears out and, their positions shift slightly to higher fields. The features near $H = 0$ are related to the step-like field-induced magnetization, observed in DTO and HTO. This, in fact, is the manifestation of the transition between the spin-ice and Kagome-ice phases for the magnetic field directed along [111]. In the absence of field, all states are degenerate (with the lowest-energy configuration "two in - two out"), which yields the large residual Pauling entropy $\mathcal{S} = (1/2)\ln(3/2)$ per spin. On the other hand, the small nonzero magnetic field fixes the "out" direction of

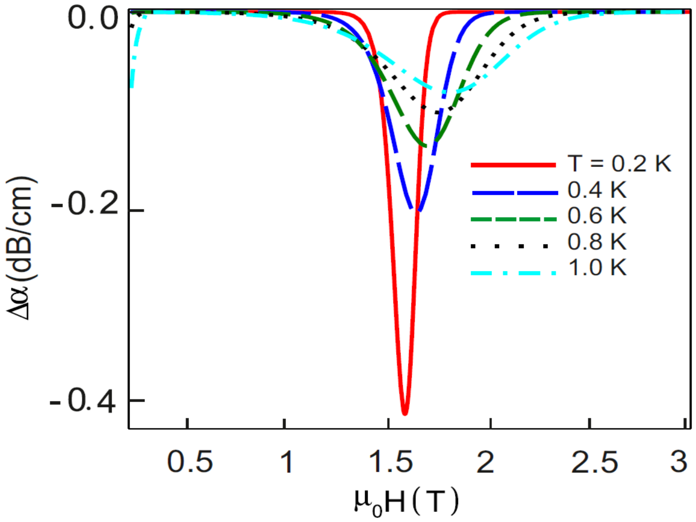

Figure 5.11: Calculated magnetic-field dependence of the sound attenuation, $\Delta\alpha$, at different temperatures for the field applied along the [111] direction.

one spin, while the three other spins in the tetrahedron are free to choose, which of them is directed "out" to fulfill the spin-ice rule. In this case, the entropy of the system becomes smaller than the Pauling value, $\mathcal{S} = (1/4)\ln(4/3)$.

Now, let us consider a magnetic field applied along the [100] direction. At $H = 0$, we have $\langle S_0 \rangle = 0$ and $\chi = 2/3T$, Eq. (5.4) as before. For $H > 0$ applied along the [100] direction, however, the so-called Kasteleyn transition takes place at $H = H_K = \sqrt{3}\ln(2)T/2$. At this magnetic field a transition from the spin-ice to a pseudo-ordered phase with zero entropy and 1/2 of the saturation magnetization occurs. In this pseudo-ordered phase one of the six possible "2-in 2-out" spin configurations becomes distinguishable lifting completely the ground-state degeneracy. At $H_K$ or at the corresponding temperature, $T = T_K = 2H/\sqrt{3}\ln(2)$, the magnetization jump leads to characteristic features in the sound velocity (Fig. 5.12) and attenuation (Fig. 5.13)

Experimentally, we observed some anomalies in the acoustic properties at very low magnetic field where the Kasteleyn transition should happen. These anomalies are affected by sample-history effects and are irreversible. That is why it is challenging to compare directly the model predictions with the experimental observations.

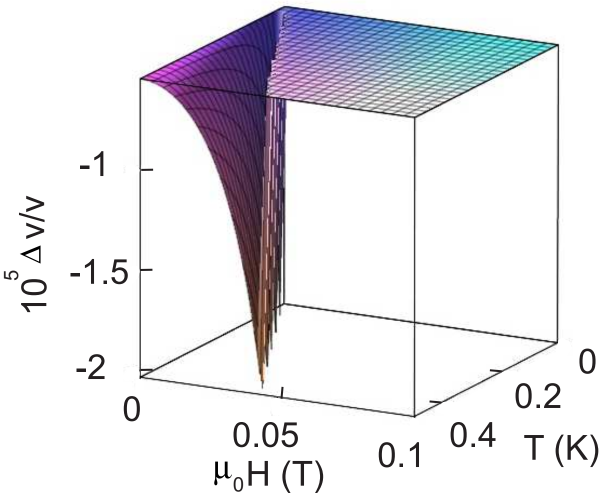

Figure 5.12: Calculated magnetic field and temperature dependence of the relative change of the sound velocity, $\Delta v/v$, for the field applied along the [100] direction.

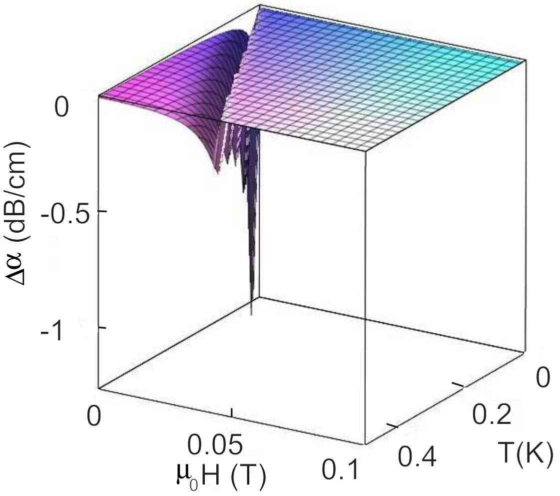

Figure 5.13: Calculated magnetic field and temperature dependence of the sound attenuation, $\Delta\alpha$, for the field applied along the [100] direction.

# 6 Temperature dependent and pulsed-field studies

In this chapter, I discuss some experimental results and theoretical considerations of temperature-dependent and pulsed field magnetoacoustic properties of HTO and DTO. First, the temperature dependence of the acoustic properties of HTO and DTO is explained. Then, the field dependence properties of these compounds in pulsed-field measurements will be considered. The simulation of the sound characteristics in the framework of single-ion magnetoelastic couplings will be discussed in the last section.

## 6.1 Temperature-dependentacoustic properties of spin ice

With decreasing temperature, the sound velocities of DTO and HTO first increase, due to the common anharmonicity of the ionic potential [89, 116] and become nearly constant at lower temperatures (Fig. 6.1). There are some irregular features (change of curvature) for most of the acoustic modes which presumably are caused by crystal-electric-field (CEF) states partly populated at these temperatures. The absolute values of the sound velocities and elastic constants in DTO and HTO for some acoustic modes at 1.3 K are listed in Table 6.1.

Table 6.1: Absolute values of the sound velocity (elastic constant) in m/s (GPa) measured at $T = 1.3$ K.

| Mode | $v$(DTO) | $v$(HTO) | $c_{ij}$(DTO) | $c_{ij}$(HTO) |
|---|---|---|---|---|
| $c_{11}$ | 7190 | 6960 | 293 | 354 |
| $c_L$ | 6980 | 6705 | 326 | 312 |
| $c_T$ | 3670 | 4040 | 90 | 113 |

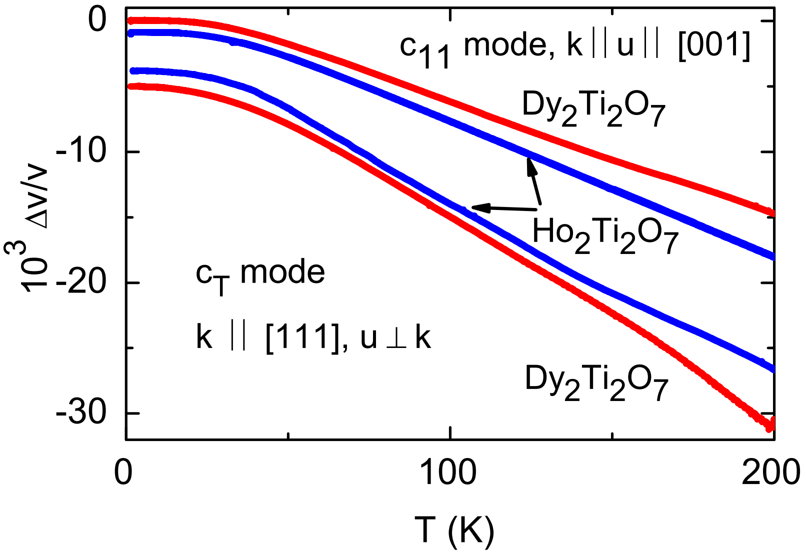

Figure 6.1: (Color online) Temperature dependence of the sound-velocity changes, $\Delta v/v$, in HTO and DTO for transverse, $c_T$, (lower two curves) and longitudinal, $c_{11}$, (upper two curves) acoustic modes. The curves are offset along the $y$ axis for clarity. For DTO, the ultrasound frequencies of 97.7 and 171 MHz were used for the $c_{11}$ and $c_T$ modes, respectively. For HTO, 50 and 109.5 MHz were used for $c_{11}$ and $c_T$, respectively.

Figure 6.2 shows the temperature dependences of the sound velocity and sound attenuation between 1.5 K and 40 K for the $c_L$ modes in HTO and DTO. The sound attenuation, $\Delta\alpha$, exhibits a slight maximum at 20 K in HTO, whereas $\Delta\alpha$ in DTO displays a smooth increase towards low temperatures. The total attenuation change for DTO is an order of magnitude larger. Presumably, CEF effects lead to the changes of the sound attenuation at these temperatures.

Data for the $c_L$ mode down to 0.29 K are shown in Fig. 6.3. In DTO, the sound velocity first grows with increasing temperature up to $T_f \approx 0.5$ K, followed by a plateau and a maximum at approximately 1.7 K. A small hysteresis is observed here. Above this temperature, the sound velocity starts to decrease. In HTO, the sound velocity decreases rapidly from the lowest temperatures showing a drastic change of the slope near 2 K, in which the spin-ice freezing regime terminates in this compound. Various techniques revealed $T_f$ slightly below 2 K in HTO and below about 0.5 - 0.6 K in DTO. [5, 66, 75, 78, 117]

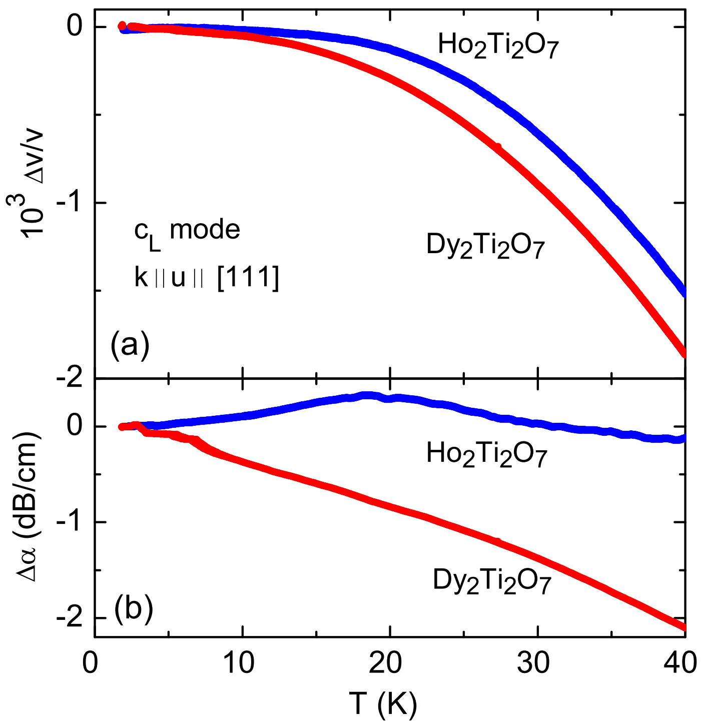

Figure 6.2: (Color online) Temperature dependence of (a) the sound-velocity change, $\Delta v/v$, and (b) the sound attenuation, for the longitudinal $c_L$ mode measured at 49 (HTO) and 96.5 MHz (DTO) between 1.5 and 40 K.

In both compounds, the sound attenuation increases first followed by an anomaly at the freezing point (a kink in DTO and a maximum in HTO) and a smooth change towards higher temperatures (Fig. 6.3b). In case of HTO, the hysteresis in the vicinity of the freezing point is less pronounced (not shown). Both the rapid change in the sound velocity and the decrease in the sound attenuation below the freezing temperature shows the important role of magneto-elastic interactions in these spin-ice materials.

Figure 6.4 shows the temperature dependence of the sound velocity and attenuation for the $c_T$ mode in HTO below 7 K. Remarkably, the sound velocity decreases with temperature reduction. At 2 K, that is slightly above $T_f$ a clear change of slope both in the sound velocity and in the sound attenuation occurs. Presumably due to a stronger spin-lattice interaction and coupling to spin degrees of freedom, the $c_T$ mode begins to soften at temperatures much higher than the $c_L$ mode (Fig. 6.3). The insets of Fig. 6.4 show the sound velocity and

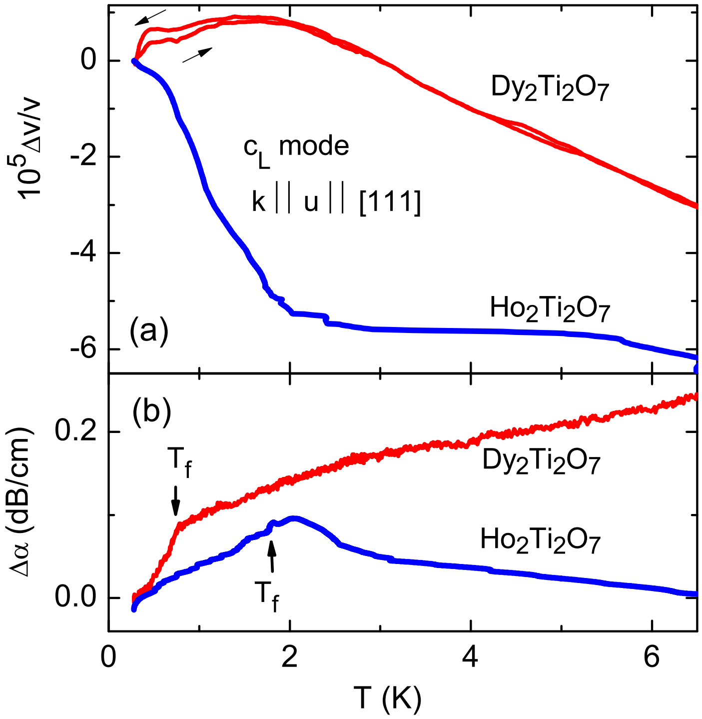

Figure 6.3: Temperature dependence of (a) the sound-velocity change, $\Delta v/v$, and (b) the sound attenuation measured at 52 MHz for HTO and 86 MHz for DTO between 0.29 and 6.5 K. The data at the lowest temperatures were set to zero on the ordinates. Arrows indicate temperature-sweep directions.

attenuation measured in a dilution refrigerator below 0.6 K. Well-pronounced anomalies in both acoustic characteristics appear at about 0.15 K. The origin for such behavior is not clear at present. Note, that possible ordered phases at very low temperatures in spin-ice materials have been discussed previously [104, 118].

The elastic properties at high-temperatures are qualitatively similar for DTO and HTO (see Figs. 6.1 and 6.2). Towards lower temperatures, however, they exhibit remarkably different temperature dependences (Fig. 6.3). These differences probably arise from details of the exchange-striction interactions (see section 5.3) as well as an involvement of nuclear spins in the case of HTO.

Figure 6.5 shows the temperature dependence of the sound velocity and attenuation measured in different fields for the $c_L$ mode in DTO in the temperature region where the spin freezing occurs. At 0.03 T, the anomaly around 0.5 K is most pronounced, and becomes suppressed gradually with increasing magnetic

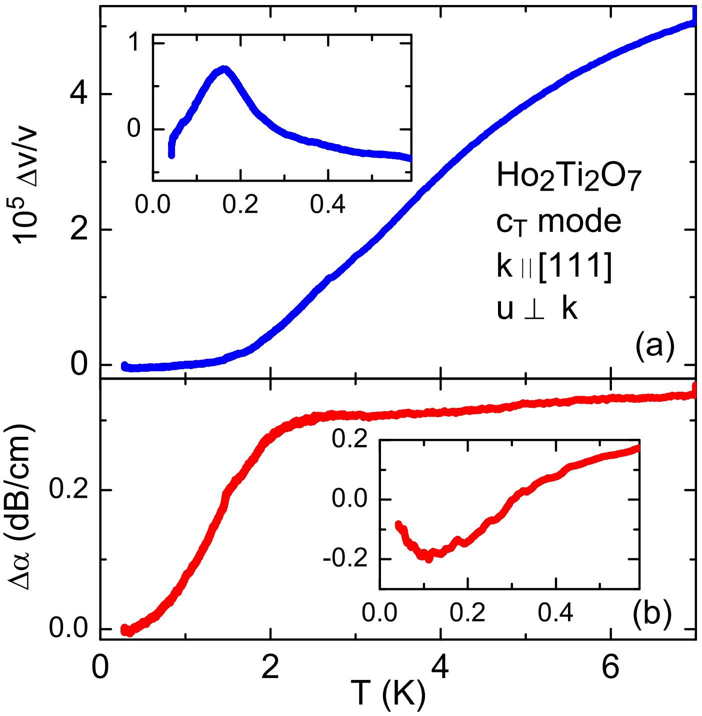

Figure 6.4: Temperature dependence of (a) the sound velocity, $\Delta v/v$, and (b) the sound attenuation of the transverse ultrasonic wave propagating along the [111] direction (acoustic $c_T$ mode) in HTO. The ultrasound frequency was 181 MHz. The insets show low-temperature data at 28 MHz obtained using the dilution refrigerator.

field. one may suggest that this behavior below 1 K, is due to the freezing processes in spin ice, in which the dynamics are found to have a temperature-activated behavior [66]. In the attenuation, a kink-like behavior at about 0.75 K, shifts towards higher temperatures as the magnetic field increases.

Additionally, the influence of CEF effects were found in the temperature dependence of the sound velocity and attenuation at different frequencies in the acoustic $c_{11}$ mode (see Fig. 6.6). The results obtained in the frequency range from 38 to 182 MHz show that by increasing the frequency the slope of the sound velocity decreases by lowering the temperature from 250 to around 50 K. The sound attenuation exhibits, a number of anomalies above 150 K which is most probably related to the first excited CEF state.

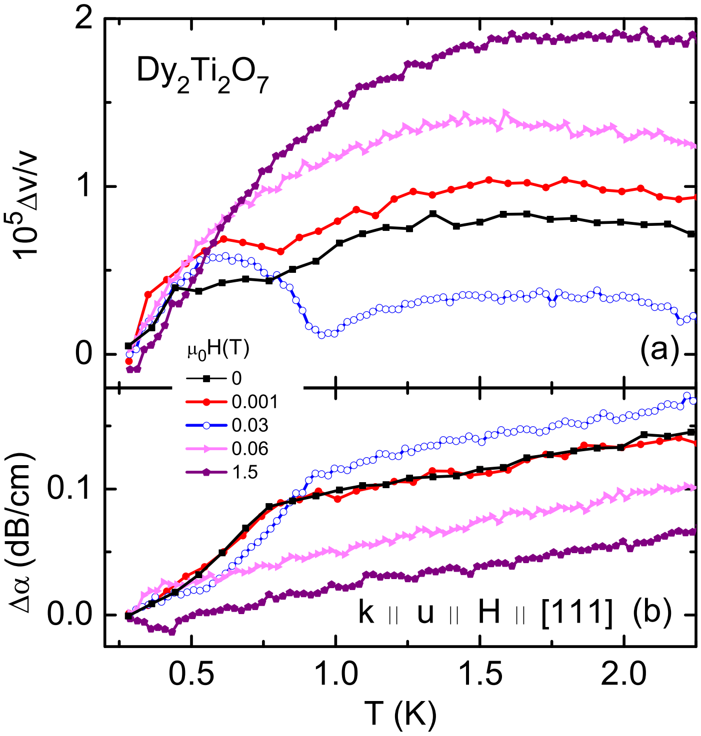

Figure 6.5: Temperature dependence of (a) the sound velocity, $\Delta v/v$, and (b) the sound attenuation of the acoustic $c_L$ mode for different magnetic fields. The data were measured at an ultrasound frequency of 86.34 MHz under ZFC condition with increasing temperature. The data are shifted along the $y$ axis to merge at the lowest temperature.

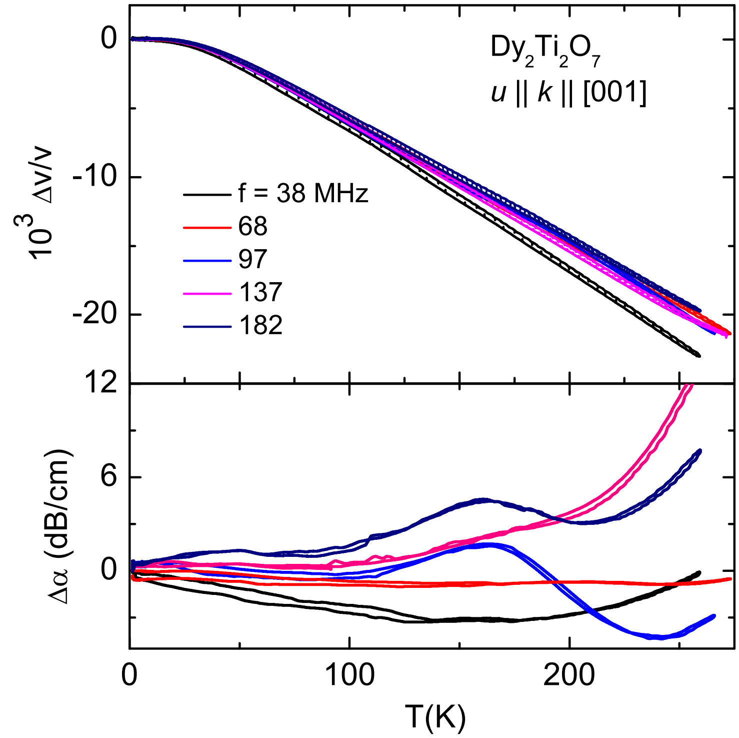

Figure 6.6: Temperature dependence of the sound velocity, $\Delta v/v$, (top) and the sound attenuation, $\delta\alpha$, (bottom) of the longitudinal ultrasonic wave propagating along the [001] direction (acoustic $c_{11}$ mode) at different frequencies.

## 6.2 Pulsed-field results

To study CEF effects in the spin-ice materials in more detail, we performed ultrasound and magnetization experiments in pulsed magnetic fields up to 60 T. Figures. 6.7 and 6.8 show field dependences of the sound velocity and sound attenuation of the $c_L$ modeas well as the magnetization in DTO and HTO measured at 1.5 and 1.4 K, respectively. The sound velocity decreases in both compounds with increasing magnetic field. For HTO, pronounced anomalies appear in the sound velocity and sound attenuation around 50 T. These anomalies can be attributed to CEF energy-level crossings (see section 6.2.1). For DTO the magnetization exhibits a plateau around 2 T in the up sweep accompanied by a pronounced hysteresis. The high-field data show that the magnetization in these compounds does not saturate even at 60 T (see the discussion in section 6.2.1).

In Fig. 6.9, the field dependence of the sound velocity and sound attenuation of the $c'_L$ mode in DTO is shown. Strong field-dependent changes appear above 35 T. Both the sound velocity and attenuation show strong hystereses and pronounced minima at about 53 T. Around 53 T these minima are sharper at the lower temperature of 1.6 K compared to 4.2 K. These anomalies are discussed later by a CEF model (compare with Fig. 6.13).

### 6.2.1 Single-ion magnetoelastic coupling

The purpose of this section is to provide an explanation for the pronounced changes in the sound velocity at high fields applied along the [111] (Fig. 6.8) and [112] (Fig. 6.9) directions. The fields attained in the experiments are on the scale of $\mu_{\mathrm{B}}\langle J\rangle H/k_{\mathrm{B}} \sim O(100)$ K which is much larger than the scale of the interactions (which are of the order of 1 K) but comparable to the CEF splittings. Therefore, in contrast to section 5.3, one may ignore the exchange couplings and consider instead the coupling between the lattice degrees of freedom and the single-ion anisotropy mediated by deformations of the crystal-field environment surrounding the magnetic ions. It is worth to mention that the calculations in this section and Figs. 6.10 to 6.13 were made kindly by Paul. Mc. Clarty.

The model studied is

$$H = H_{\mathrm{el}} + H_{\mathrm{CF}} + H_{\mathrm{Z}} + H_{\mathrm{mag-el}}.$$

The first term, $H_{\mathrm{el}}$, is the energy cost of deforming the crystal. The second part, $H_{\mathrm{CF}}$, is the single-ion crystal-field Hamiltonian on each site with Zeeman term $H_{\mathrm{Z}}$. The magneto-elastic interaction is $H_{\mathrm{mag-el}}$.

As described in Sec. 2.4 for cubic systems, there are three independent elastic moduli by symmetry, so

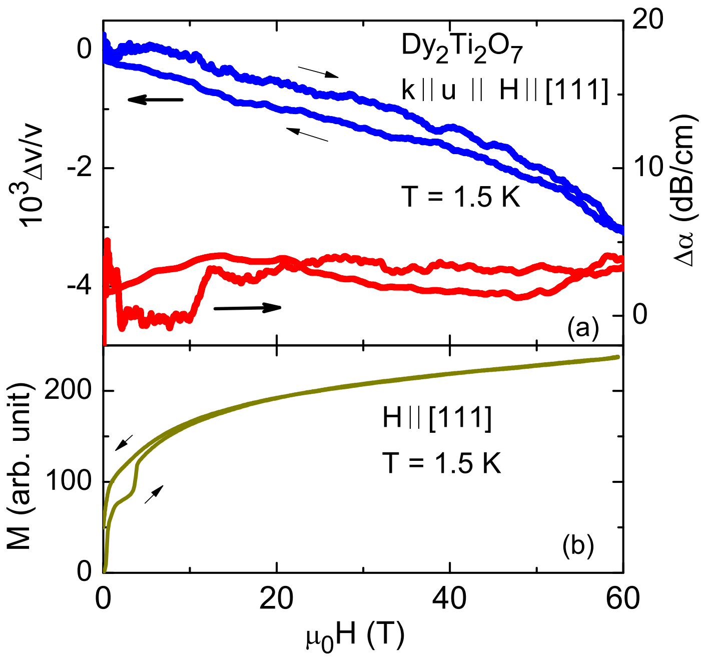

Figure 6.7: Field dependence of (a) the sound velocity, $\Delta v/v$, and sound attenuation, $\Delta\alpha$, of the $c_L$ mode and (b) the magnetization measured in DTO in pulsed magnetic fields up to 60 T at 1.5 K. The ultrasound frequency was 63 MHz. Thin arrows indicate field-sweep directions.

$$\begin{aligned}
H_{\mathrm{el}} &= \frac{1}{2} c_{11} \left(\epsilon_{xx}^2 + \epsilon_{yy}^2 + \epsilon_{zz}^2\right) \\
&+ c_{12} \left(\epsilon_{xx}\epsilon_{yy} + \epsilon_{xx}\epsilon_{zz} + \epsilon_{zz}\epsilon_{yy}\right) \\
&+ 2c_{44} \left(\epsilon_{xy}^2 + \epsilon_{xz}^2 + \epsilon_{yz}^2\right) \ , \qquad (6.1)
\end{aligned}$$

where the strains $\epsilon_{\alpha\beta}$ are dimensionless and the elastic moduli $c_{\alpha\beta}$ expressed in GPa.

The crystal-field and Zeeman terms are

$$\begin{aligned}
H_{\mathrm{CF}} &= \sum_i B_0^2 O_0^2(i) + B_0^4 O_0^4(i) \\
&+ B_3^4 O_3^4(i) + B_0^6 O_0^6(i) + B_3^6 O_3^6(i) + B_6^6 O_6^6(i) \ , \\
H_{\mathrm{Z}} &= -g_{\mathrm{J}} \mu_{\mathrm{B}} \sum_i \mathbf{J}_i \cdot \mathbf{H} \ . \qquad (6.2)
\end{aligned}$$

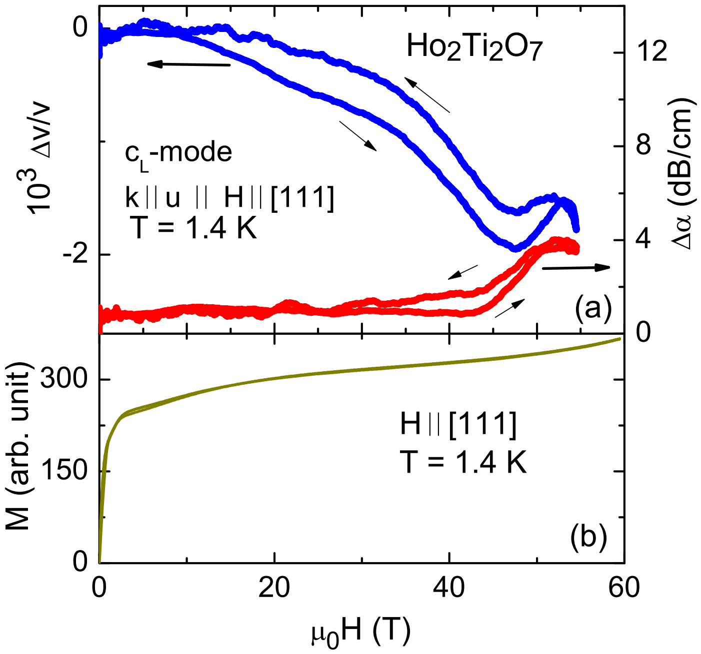

Figure 6.8: Field dependence of (a) the sound velocity, $\Delta v/v$, and sound attenuation, $\Delta\alpha$, for the $c_L$ mode and (b) the magnetization in HTO measured at 1.4 K. The ultrasound frequency was 70.9 MHz. Thin arrows indicate field-sweep directions.

Here, $O^l_m(i)$ are Stevens operators on site $i$. The crystal-field Hamiltonian is written in local coordinate frames - one for each of the four sublattices in the tetrahedral basis - in which the local $z$ axes are aligned along the respective [111] directions. The Stevens operators are restricted to $l = 2$, 4 and 6 because the magnetic ions have orbital angular momentum $L = 3$. The further restriction to the six operators given above comes about because the crystal-field environment is symmetric under the operations of point group $D_{3d}$. In the following, the parameters $B^l_m$ for HTO ($J_{\mathrm{Ho}} = 8$) obtained by fitting the spectrum of Eq. (6.1) to inelastic neutron data were taken [87].

The magneto-elastic coupling results from the crystal-field Hamiltonian by expanding in small displacements arund the equilibrium ionic positions. It is convenient to separate these displacements into macroscopic strain, macroscopic rotations, and microscopic strains coming from displacements of the sublattices. In the following, it (i) is considered the material to be completely homogeneous and (ii) include only the effect of macroscopic strains from which the sound

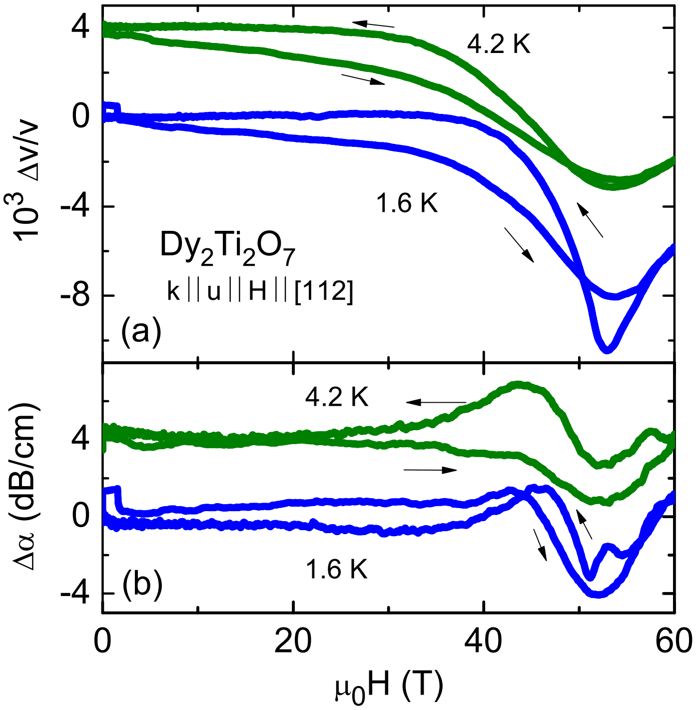

Figure 6.9: Field dependence of (a) the sound velocity, $\Delta v/v$, and (b) sound attenuation, $\Delta\alpha$, of the $c_L'$ mode in DTO at 1.6 and 4.2 K. The ultrasound frequency was 53.4 MHz. Arrows indicate field-sweep directions. The data for different temperatures are arbitrarily shifted along the $y$ axis for clarity.

velocities are to be computed. Even with these simplifications, the magnetoelastic couplings are

$$\begin{aligned} H_{\mathrm{mag-el}} &= \sum_i \sum_{l,m} \left[g_m^l\right]_{\alpha\beta} \bar{\epsilon}_{\alpha\beta} O_m^l \\ &= \sum_{i,\Gamma} \sum_{l,m} \left[g_m^l\right]_\nu (\Gamma) \bar{\epsilon}_\nu (\Gamma) O_m^l \ , \end{aligned} \tag{6.3}$$

where $\Gamma$ denotes an irreducible representation of the group of local crystal-field symmetry, $D_{3d}$, and $\nu$ runs over the basis states of the irreducible representation.

Since the number of parameters, $\left[g_m^l\right]_{\alpha\beta}$, is large, they are computed from first principles using a point-charge model including the distorted cube of oxygen ions surrounding the magnetic ions. Then a handful of the parameters was varied in order to explore the typical behavior of the sound velocities as a function of field. However, it is noted that while the point-charge approximation alone does not very successfully reproduce the known single-ion anisotropies and crystal-field gaps for the series of rare-earth pyrochlores the interest is in establishing which features are only weakly dependent on the choice of parameters.

The calculation of the sound velocity proceeds by evaluating the change in the strains produced by a given magnetic field and then computing the change in energy brought about by these strains. Minimizing the free energy with respect to the strain leads to

$$\begin{aligned}\Delta\epsilon(G) = -\frac{1}{V}\frac{1}{C(G)}\sum_{n}\sum_{l,m}\sum_{\Gamma,\nu}\left[g^{l}_{m}\right]_{\nu}(\Gamma)T^{\Gamma}_{G,n} \\ \times\left\{\langle O^{l}_{m}\rangle_{n} - \langle O^{l}_{m}\rangle_{n,\mathbf{B}=0}\right\}. \qquad (6.4)\end{aligned}$$

Here, $V$ is the volume of the FCC unit cell and $T$ is a matrix of derivatives to convert from the frame of strains in some representation to the strains in the global frame. The sum is taken over four sublattices labeled $n$. The self-consistent strain is obtained iteratively.

The changes to the elastic moduli upon coupling the crystal field to the lattice degrees of freedom may be computed by observing that the elastic moduli are equivalent to susceptibilities to lattice distortions. In other words, one computes the second derivative of the free energy with respect to the strain ensuring that the moduli are evaluated about the self-consistent solution for the strain. The second derivative is evaluated by computing the change to the magnetoelastic energy under a small change in the strain.

$$\begin{aligned}\Delta C(G) = \frac{1}{V}\frac{1}{\delta\epsilon(G)}\sum_{n}\sum_{l,m}\sum_{\Gamma,\nu}\left[g^{l}_{m}\right]_{\nu}(\Gamma)T^{\Gamma}_{G,n} \\ \times\left\{\langle O^{l}_{m}\rangle_{n} - \langle O^{l}_{m}\rangle_{n,\delta\epsilon=0}\right\}. \qquad (6.5)\end{aligned}$$

Changes in the moduli as a function of field are obtained from this formula by diagonalizing the single-ion Hamiltonian on each sublattice in the presence of the self-consistent solution for the strain.

One can compute the change in the longitudinal sound velocity in a magnetic field applied along the [112] direction for DTO. The temperature is set to 4.2 K. Whereas in zero field all four sublattices of the pyrochlore lattice are equivalent, the [112] magnetic field results in three inequivalent directions with the moments on one of the sublattices (in our convention, sublattice 3) perpendicular to the

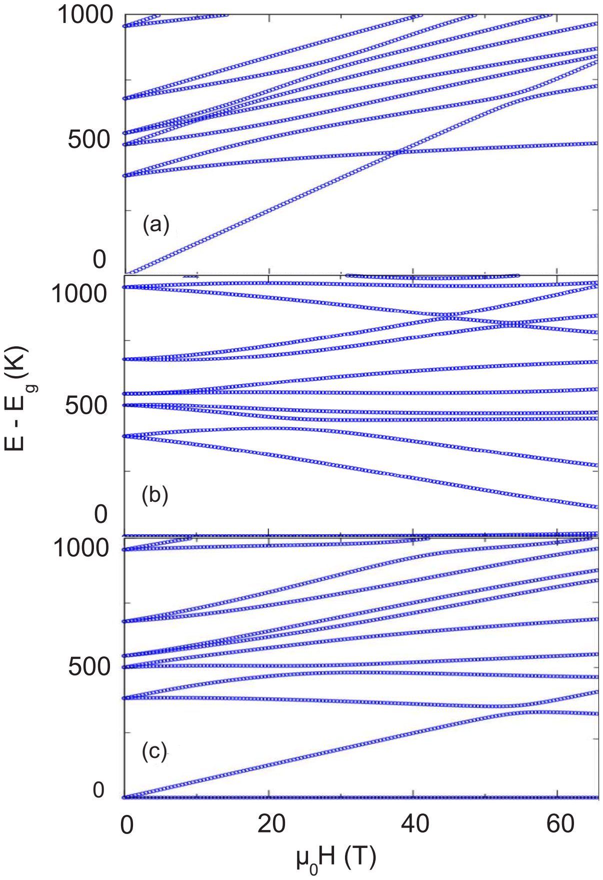

Figure 6.10: Field dependence of the crystal-field spectra for DTO in a field aligned along [112] for (a) sublattice 0 (b) sublattice 3, and (c) sublattices 1 and 2. On the vertical axis, the energy measured relative to the ground-state energy, $E_g$, is plot.

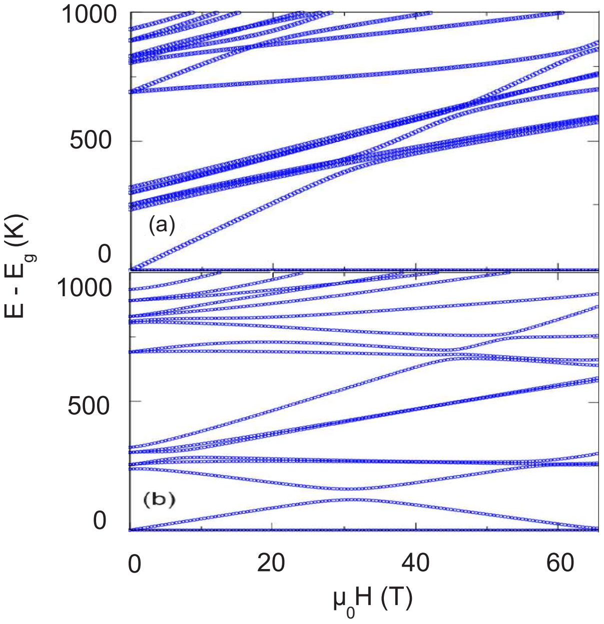

Figure 6.11: Plot of the crystal-field spectra for $Ho_2Ti_2O_7$ in a field aligned along the [111] direction for (a) sublattice 0 and (b) sublattices 1, 2, and 3. On the vertical axis the energy measured relative to the ground state energy, $Eg$, is plot.

field. The inequivalent spectra are shown in Fig. 6.10. Also spectra for sets of parameters computed from first principles using the point-charge approximation were examined. The generic features of the low-lying crystal-field levels are as follows. The degeneracy of the lowest Ising doublet is split at the smallest fields but only weakly on sublattice 3 as a result of admixing with excited levels. There are level crossings of the first-excited levels above the low-lying doublet at the fields probed by experiment and a ground state level crossing on sublattice 3 between 80 and 90 T which is associated with a gradual upturn in the magnetization.

The sound velocity as a function of field was studied for many choices of magnetoelastic couplings. Typically, one observes two principal features in $\Delta v/v$. The first is a peak or trough which is associated with the thermal depopulation of the first excited level. This correspondence is based on the fact that the temperature is set to a value between 1.6 and 4.2 K and, at these low temperatures, the feature is found to shift to lower fields at lower temperatures. In contrast, the experimental data reveal an anomaly with a minimum at about 52 T at both 1.6 and 4.2 K (Fig. 6.9). The second main feature in the calculation of $\Delta v/v$ is a large anomaly at the ground-state level crossing that occurs at about 80 T in the spectrum computed from the parameters obtained (i) from the point-charge approximation, (ii) by converting parameters from those obtained in Ref. [87], and (iii) the parameters reported in Ref. [119]. However, these sets of crystal-field parameters are not taken directly from experimental measurements. One might consider the sound-velocity data reported here to indicate a ground-state level crossing on sublattice 1 at around 60 T. If this is the case then the available crystal-field parameters either overestimate the crystal field gap or underestimate the moment of the first excited levels.

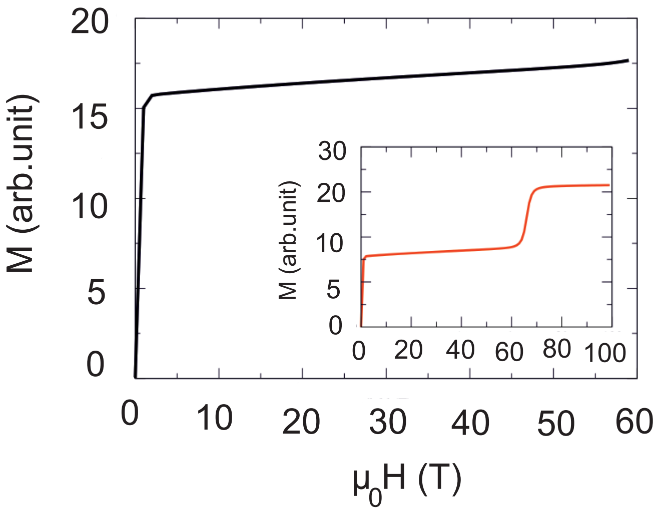

Figure 6.12: The total moment as a function of field calculated for HTO using crystal-field spectra shown in Fig. 6.11.

For a field aligned along the [111] direction in HTO the longitudinal sound velocity decreases showing a minimum at about 47 T (Fig. 6.8). This field direction has the characteristic of creating two inequivalent magnetic sites - one with the field aligned along the direction of the zero-field anisotropy (sublattice 0 in our convention) and the second (belonging to tetrahedral sublattices 1, 2, and 3) at an angle of about 54.7 degrees to it. Looking at the crystal-field spectra for these sublattices (and for various sets of crystal-field parameters) one observes that the degeneracy of the ground-state Ising doublet is lifted in arbitrarily weak fields as one expects - the moments are pinned, as far as possible given the anisotropy, along the field direction (Fig. 6.11). For sublattice 0, there is a succession of excited-state level crossings - the ground state being pinned along

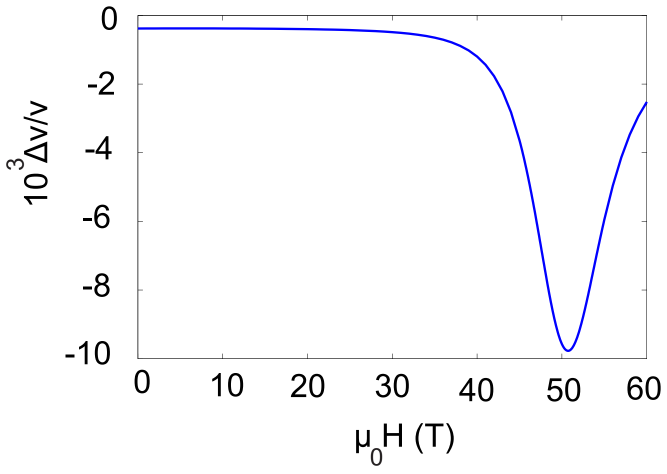

Figure 6.13: Calculated magnetic-field dependence of $\Delta v/v$ in DTO from field parameters of Ref. [87]. The dip in the sound velocity is a typical feature - only weakly dependent on the choice of magnetoelastic couplings.

the field direction. For the other sublattices, there is a ground-state level crossing (at about 62 T for the parameters of Ref. [87]) and a crossing of the first-excited level at about half of this field. The ground-state level crossing is associated with a step in the magnetization which is not present in the experimental data up to 60 T although there is an upturn in the magnetization at the highest fields (Fig. 6.8) which is also present in the calculated magnetization up to 60 T (Fig. 6.12). It is expected that an exploration of the magnetization at higher field would reveal the predicted step in the magnetization within a few Tesla of 60 T.

$\Delta v/v$ was calculated for DTO for the parameters obtained from the point-charge approximation. For a large number of choices of magnetoelastic couplings, the picture presented by these calculations is that a single feature dominates $\Delta v/v$ with a minimum at fields below the ground-state level crossing by up to 10 T (Fig. 6.13). It is, therefore, likely that the ground-state level crossing on magnetic sites belonging to sublattices 1, 2, and 3 is responsible for the form of the high-field sound-velocity data (Fig 6.9).

Theoretical explanation presented in this section bases on single ion-strain interaction agrees well with the pulsed-field experimental data of the ultrasound and magnetization measurements.

# 7 Magneto-acoustic studies of $Yb_2Ti_2O_7$ (YbTO)

Various fascinating physical phenomena have recently been identified in a class of rare-earth titanates known as quantum spin ice [120–125]. In these materials, there is a quantum tunneling between different configurations (2 spins in and 2 spins out) of the spin ice ground state (see Sec. 4.2). It seems to be now well established that the quantum spin ice state occurs at low temperatures in $Yb_2Ti_2O_7$ (YbTO) [120, 121, 125]. There is no long-range magnetic ordering in this state, due to the frustration and quantum fluctuations [126, 127]. In YbTO, there are some short-range correlations at low temperatures which develop below 0.4 K. Moreover, various experimental measurements, such as neutron scattering and specific heat, have indicated the entering to an exotic ground state below $T$ = 0.25 K [128]. The nature of this phase transition is not clear yet, while some reports indicate a kind of deconfined to confined states of spinons at zero field [129]. Other investigations claim a Bose-Einstein condensation of monopoles via a Higgs mechanism during the transition [125]. In latter case, the resultant phase would contain monopole carrying spinons and emergent photons.

It is generally known that quantum fluctuations allow the creation of particle-antiparticle pairs. In case of YbTO, it has been reported that quantum fluctuations lead to spin excitations consisting of spinon-antispinon pairs [120]. These quasiparticles are created after mass acquisition of magnetic monopoles in a Bose-Einstein condensation via a Higgs mechanism. Therefore, the resultant phase containing deconfined mixtures of spinon-antispinon pairs has been interpreted as superconducting behavior of magnetic monopoles [125]. Here, I report on the possible phases at low temperatures and low fields in YbTO.

## 7.1 Experimental results

The ultrasound experiments have been carried out for two acoustic modes: (i) the longitudinal $c_L$ mode, $c_L = (c_{11} + 2c_{12} + 4c_{44})/3$ ($\mathbf{k}\|\mathbf{u}\|[111]$), (ii) the transverse $c_T$ mode, $c_T = (c_{11} + c_{44} - c_{12})/3$ ($\mathbf{k}\|[111]$, $\mathbf{u}\perp\mathbf{k}$). The relative change of

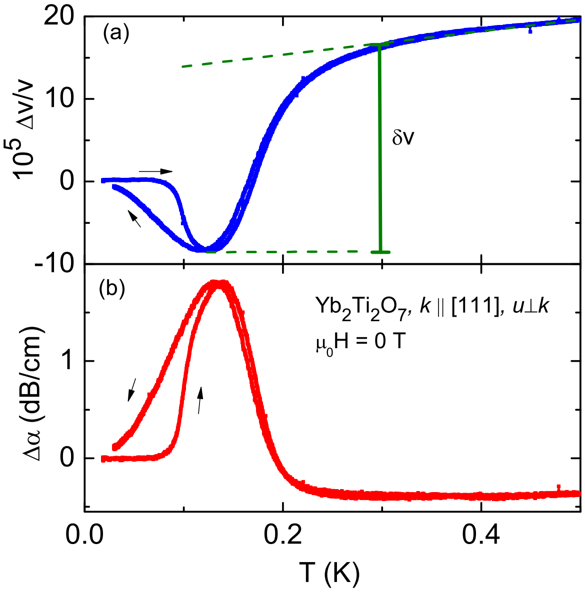

Figure 7.1: Temperature dependence of (a) the sound velocity, $\Delta v/v$, and (b) sound attenuation, $\Delta\alpha$, for the transverse acoustic $c_T$ mode, propagating along the [111] direction. The magnetic field is applied along the propagation direction.

the sound velocity, $\Delta v/v$, and the sound attenuation, $\Delta\alpha$, were measured. All measurements have been performed under zero-field-cooled (ZFC) conditions.

AS shown in Fig.7.1, the sound velocity of the $c_T$ mode exhibits a smooth decrease when lowering the temperature from 0.6 K down to approximately 0.3 K. In this temperature range, the sound attenuation is temperature independent with an almost constant value. Below about 0.3 K, the sound velocity decreases rapidly down to a minimum at about 150 mK (Fig.7.1). At lower temperatures, $\delta v/v$ increases again and shows a hystereses.

The sound velocity at low temperatures in the absence of other factors, usually exhibits a temperature independent behavior. Quantum fluctuations can cause a softening of the sound velocity. The observed behavior between 0.15 and 0.3 K can arise when entering the magnetic Coulomb-liquid phase (MCL) with pronounced quantum fluctuations. In this temperature range, quantum fluctuations may develop. The notable Hysteresis below 0.15 K accompanied by the increase in the sound velocity and decrease in the sound attenuation may be attributed to the Coulomb-ferromagnet state in which the fluctuations are almost suppressed.

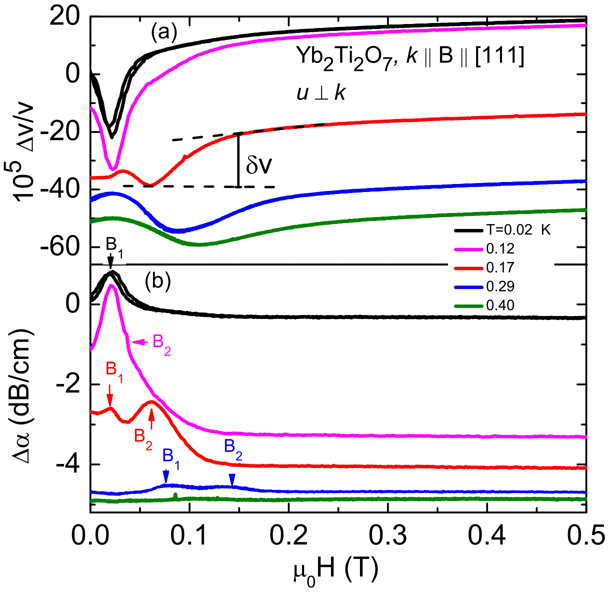

Figure 7.2: Field dependence of (a) the sound velocity, $\Delta v/v$, and (b) sound attenuation, $\Delta\alpha$, for the transverse acoustic $c_T$ mode, propagating along the [111] direction. The magnetic field is applied along the same direction. The fields $B_1$ and $B_2$ indicate crossover lines. The results for all temperatures except for 0.02 K are shown for up sweeps. The curves are arbitrarily shifted along the y axis for clarity.

Indeed, the softening $\delta v$ shown in Fig 7.1 may indicate the presence of quantum fluctuations. The fluctuation frequency between equivalent configurations of the ground state of YbTO is approximately 10 GHz [130] in the MCL phase. This frequency is at the order of MHz in the Coloumb ferromagnetic phase.

Figure 7.2 shows the field dependence of the sound characteristics at different temperatures for the $c_T$ mode. Pronounced anomalies appear at about 0.025 T at the base temperature of 0.02 K. With increasing temperature, this anomaly shifts to higher fields, i.e., up to about 0.11 T at 400 mK. Above these fields the sound velocity saturates and shows an almost field-independent behavior up to 5 T (not shown here). Interestingly, the depth of the minimum in $\delta v/v$ increases when increasing the temperature from 0.02 to 0.12 K. Above these temperatures, the minimum decreases and $\delta v/v$ becomes almost flat at 0.4 k. The same trend can be observed in the sound-attenuation peak. Above 0.12 K, the peak starts to broaden and splits in two peaks. A $\mu_0 H - T$ phase diagram obtained from these anomalies in the sound attenuation is shown in Fig. 7.3. The triangle in Fig.

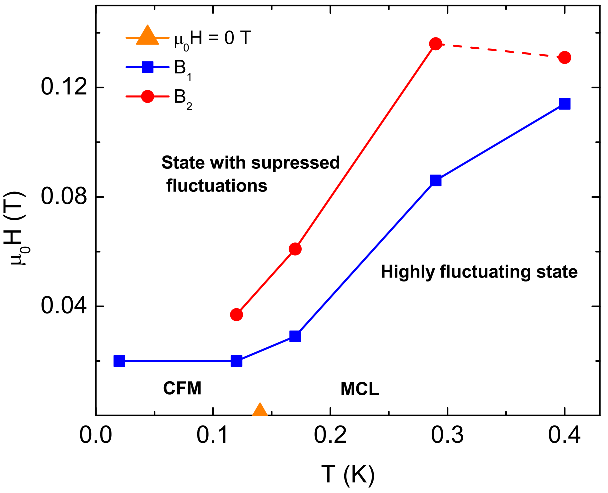

Figure 7.3: $\mu_0 H - T$ phase diagram based on the ultrasound data shown in Figs. 7.1 and 7.2.

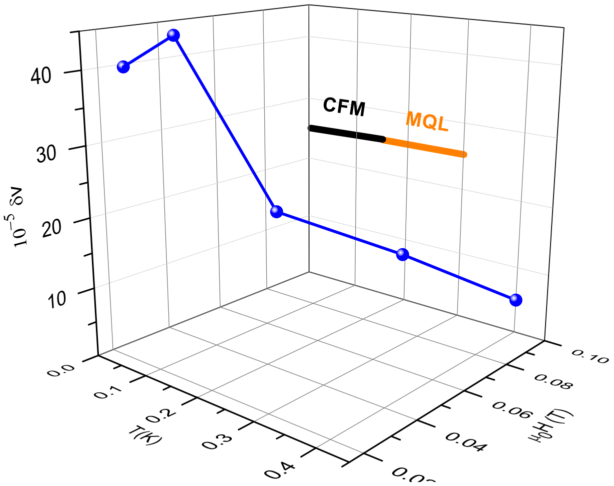

Figure 7.4: $v(T, \mu_0 H)$ Three dimensional plot of $\delta v$ as function of $\mu_0 H$ and T obtained from field-dependent measurements of the sound velocity at different temperatures. The MCL and CFM phases are shown in the $\delta v$-T plane (see text for details).

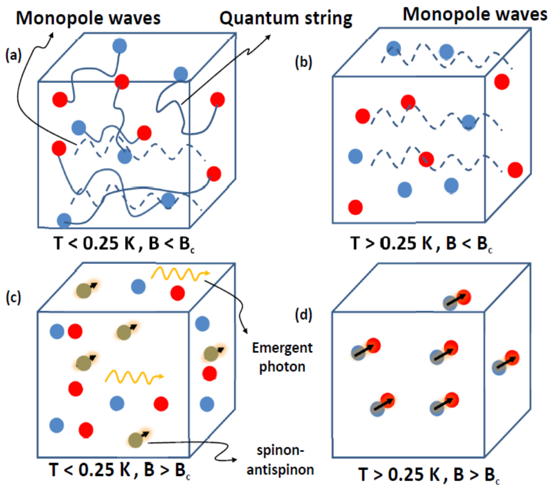

Figure 7.5: (a) Monopole waves and quantum strings, (b) monopole waves, (c) and (d) Spinon-antispinon, emergent photons in various phases with different behaviors.

7.3 indicates the sound attenuation maximum in the temperature-dependent measurement shown in Fig. 7.1. The origin of these phases are not clear yet, but we speculate these are transitions from a highly fluctuating state to a state with suppressed fluctuations.

Figure 7.4 displays the sound velocity change, $\delta v$, reflecting quantum fluctuations, versus field and temperature. Black and yellow lines show the Coloumb-ferromagnet and magnetic Coloumb-liquid phases, respectively with the presumed Higgs phase transition at approximately 0.15 K .

Bose-Einstein condensation of magnetic monopoles via a Higgs mechanism has been discussed in Ref. [125]. The resultant phase after condensation contains monopoles carrying spinons and emergent photons. Figure. 7.5 shows schematically such spinon-antispinon carrying magnetic monopoles, quantum strings, and spin waves in different phases in terms of fields and temperatures. At temperatures below 0.25 K and fields below $B_c$ (Fig. 7.5a) there are spinon-antispinon quasi-particles accompanied by monopole waves [125]. At the same field range ($B < B_c$) but, above 0.25 K (Fig. 7.5b) fluctuating magnetic monopoles exist although spinon-antispinons and quantum strings are not well defined. At $T < 0.25\ K$ and $B > B_c$, (Fig. 7.5c) fluctuating monopoles are connected with

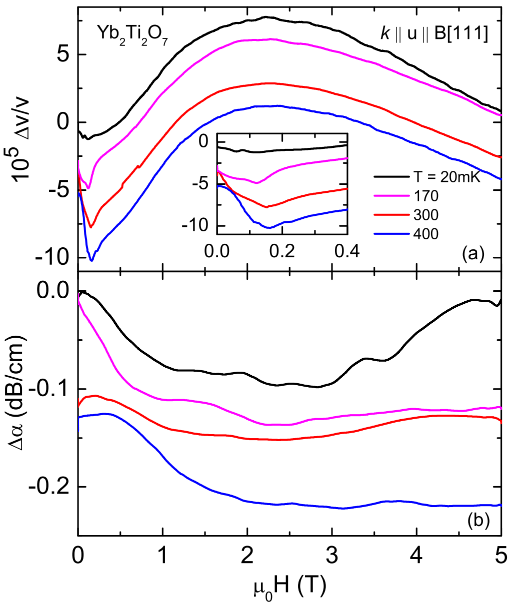

Figure 7.6: Field dependence of the sound velocity (a), $\Delta v/v$, sound attenuation, $\Delta\alpha$, (b) for longitudinal acoustic $c_L$-mode, propagating along the [111] direction in $Yb_2Ti_2O_7$. Magnetic field is applied along the same direction. Inset shows anomalies of sound velocity at low field region.

suppressed monopole waves, spinons, and gapless photons which arise from fluctuations of the electric field. (This electric field is produced by the movement of magnetic monopoles and described by Faraday's law [129]). These effects are too small to be detected by neutron-scattering measurements. In the temperature and field range for $T > 0.25$ K and $B > B_c$ (Fig. 7.5d), there are fluctuating monopoles without quantum strings and monopole waves.

The field and temperature dependence of the sound characteristics were also measured down to 20 mK for the longitudinal $c_L$ mode propagating along the [111] direction. The sound velocity and sound attenuation exhibit a number of anomalies in the low-field region (Fig. 7.6). Between 0.15 and 0.2 T, there is a minimum in the sound velocity at all measured temperatures. It turns out that the origin of this features is the same as the anomalies shown in Fig. 7.2. However, the low-field anomalies become sharper for the $c_L$ at higher temperatures, whereas the anomalies decrease with temperature for the $c_T$ mode. The nature of the maximum in the sound velocity at 2 T is not clear. It may be related to the suppression of quantum fluctuations.

# Conclusions

In conclusion, we have studied nonequilibrium processes and the role of magneto–acoustic interactions in the spin-ice materials DTO, HTO, and YbTO by means of ultrasound measurements. Unusual anomalies have been detected in all acoustic modes studied. The correlation between a magnetization plateau and sound-velocity anomalies (quasi-periodic peaks) in DTO shows that magneto-acoustic interactions play an important role in this spin-ice compound. The ultrasound technique is particularly sensitive to these effects, where the periodicity, shape, width, number, and distance between the peaks can be crisply extracted. Interestingly, the temperature of the sample follows the sound-velocity change at the peak positions, where the system has been driven out of equilibrium and avalanches of magnetic monopoles occur to re-equilibrate the system. The phonons eventually carry the released energy during the avalanche process out of the system. We, thus, observe a quasi–periodic change between thermodynamically unstable states through non–equilibrium processes, like in the "bottleneck" effect. It will be interesting to contrast this in detail to the two–dimensional magnetic arrays [131], where the role of monopoles and avalanche processes in a non-thermal ensemble have been a recent focus of attention [132].

The ultrasound investigations performed on the spin-ice materials HTO and DTO show a number of features that are common to both systems. However, differences occur in the low-temperature region. At high temperatures (7–250 K) the temperature dependent change of the sound velocity in DTO and HTO is quite similar for different acoustic modes. At low temperatures, signatures of spin freezing in DTO and HTO are observed at around 0.6 and 2 K as anomalies in the sound velocity and sound attenuation. There are a number of peculiarities in the field-dependent acoustic properties at low temperatures. Detailed information of the field-induced non-equilibrium processes in the spin-ice state of DTO show that they are independent of the demagnetization factor of the sample and appear for various sound-propagation directions, but vanish when there is a strong thermal coupling to the bath. At the gas-liquid-type phase transition in DTO, we have observed a sharp dip in the attenuation. The experimental results agree reasonably well with theoretical modeling of the sound velocity and the sound attenuation, based on exchange-striction coupling and single-ion-type interactions. The high-magnetic-field data are described reasonably well by a CEF approach.

In YbTO, the coupling of the sound wave to quantum fluctuations was investigated by sound-velocity and sound-attenuation measurement. A number of anomalies in temperature and field-dependent measurements of the sound velocity and attenuation was observed. These anomalies are attributed to a first-order phase transition, although the nature of these transitions are still under investigation.

# Bibliography

[1] J. F. Sadoc and R. Mosseri, *Geometrical frustration*, (Cambridge University Press, Cambridge, 1999).

[2] H.T. Diep, *Frustrated spin systems*, (World Scientific, Singapore, 2004).

[3] R. Moessner and A. P. Ramirez, *Geometrical frustration*, Physics Today **7**, (2006).

[4] C. Castelnovo, R. Moessner, and S. L. Sondhi, *Magnetic monopoles in spin ice*, Nature **451**, 42 (2008).

[5] S. T. Bramwell and M. J. P. Gingras, *Spin ice state in frustrated magnetic pyrochlore materials*, Science **294**, 1495 (2001).

[6] N. Shannon, O. Sikora, F. Pollmann, K. Penc, and P. Fulde, *Quantum ice: A quantum Monte Carlo study*, Phys. Rev. Lett. **108**, 067204 (2012).

[7] L. Savary and L. Balents, *Coulombic quantum liquids in Spin-1/2 Pyrochlores*, Phys. Rev. Lett. **108**, 037202 (2012).

[8] P. A. M. Dirac, *Quantised singularities in the electromagnetic field*, Proc. R. Soc. Lond. A **133**, 860-72 (1931).

[9] B. Cabrera, *In search of the magnetic monopole*, Science, **216**, 20 (1982).

[10] A. P. Ramirez, A. Hayashi, R. J. Cava, R. Siddharthan, and B. S. Shastry, *Zero-point entropy*, Nature **399**, 333 (1999).

[11] J. Snyder, J. S. Slusky, R. J. Cava, and P. Schiffer, *How spin ice freezes* Nature. **413**, (2001).

[12] R. Hooke, *Lecture de potentia restitutiva, or of spring, explaining the power of springing bodies to which are added some collections.* L.: Martin, p. 56, (1678).

[13] J. Rychlewski, PMM U.S.S.R. *On Hooke's law* **48** No.3, 303-314, (1984)

[14] R. S. Krishnax und E. S. Rajagupal, *The atomistic and the continuum theories of crystal elasticity*, Annalen der Physik. **7**, (1961).

[15] Friedrich W. Hehl and Yakov Itin, *The cauchy relations in linear elasticity theory*, Journal of Elasticity **66**, 185-192 (2002).

[16] Kun Huang, *On the atomic theory of elasticity* Proc. R. Soc. Lond. A **203**, 178-194 (1950).

[17] B. Luethi, *Physical Acoustics in the Solid State*, (Springer, Berlin, 2005).

[18] R. Truell, Charles Elbaum and Bruce B. Chick, *Ultrasonic methods in solid state physics*, (Academic press, New York and London, 1969).

[19] A. G. Every, *General, Closed-form expressions for acoustic waves in cubic crystals*, Phys. Rev. B **42**, 1065 (1979).

[20] A. J. E. Foreman, *Anharmonic specific heat of solids*, Proc. Phys. Soc., **79**, 1124 (1962).

[21] R. F. Wallis, *Lattice Dynamics*, Proceedings of the International Conference held at Copenhagen, Denmark, (1963).

[22] J. W. Tucker, and V. W. Rampton, *Microwave ultrasonics in solid state physics*, (North-Holland Publishing Company, Amsterdam, 1972).

[23] M. S. Dresselhaus, G. Dresselhaus and A. Jorio, *Group Theory: Application to the Physics of Condensed Matter*, (Springer, Verlag Berlin Heidelberg, 2008).

[24] D. F. Johnston, *Group theory in solid state physics*, Rep. Prog. Phys **23**, 66 (1960).

[25] W. A. Runciman, *Stark-splitting in crystals*, Philosophical Magazine **1**, 1075-1077 (1956).

[26] V. Dohm, *Magnetoelastic interaction in rare earth systems*, Z. Physik B **21**, 369-379 (1975).

[27] T. J. Moran and B. Luethi, *High-frequency sound propagation near magnetic phase transitions*, Phys. Rev. B **4**, 122 (1971).

[28] M. Niksch, I. Kouroudis, W. Assmus and B. Luethi, *Electron-phonon coupling in cerium compounds*, J. Magn. Magn Mat, **47&48**, 97-298 (1985).

[29] M. Yoshizawa, B. Luethi, T. Goto, T. Suzuki, B. Renker, A. de Visser, P. Frings and J. J. M. Franse, *Electron-phonon coupling in uranium compounds*, J. Magn. Magn. Mat. **52**, 413-417 (1985).

[30] P. Thalmeier, *Theory of elastic properties of heavy-fermion compounds*, J. Phys. C: Solid State Phys, **20**, 4449-4466 (1987).

[31] J. H. Van Vleck, *Paramagnetic relaxation times for titanium and chrome alum*, Phys. Rev. **57**, 426 (1940).

[32] R. B. Hemphill, P. L. Donoho, and E. D. McDonald, *Spin-lattice interaction in Ruby measured by electron spin resonance in uniaxially stressed crystals*, Phys. Rev. **146**, 329 (1966).

[33] G. A. Gehring and K. A. Gehring, *Co-operative Jahn-Teller effects*, Rep. Prog. Phys., **38**, 1-89 (1975).

[34] H. Stern: *Thermal conductivity at the magnetic transition*, J. Phys. Chem. Solids **26**, 153 (1965).

[35] C. F. V. Doorn, P. de V. du Plessis, *Anomalies in the elastic constants of antiferromagnetic uranium mononitride*, J. Magn. Magn. Mat. **5**, 164-166 (1977).

[36] J. P. Attfield, *Exchange striction and exchange constants in* $Bi_2CuO_4$, J. Phys.: Condens. Matter **1**, 7045-7053 (1989).

[37] B. Morison, *Exchange striction effects in MnO and MnS*, Phys. Rev. B, **1**, 1 (1970).

[38] M. E. Lines, *Exchange striction in magnetic cluster complexes*, Sol. State Commun, **11**, 1615-1618 (1972).

[39] L. C. Bartel and B. Morosin, *Exchange striction in NiO*, Phys. Rev. B, **3**, 3 (1971).

[40] Xiaoyan Yao, Veng Cheong Lo, and Jun-Ming Liu, *Magnetoelectric coupling induced by exchange striction in frustrated Ising spin chain: Monte Carlo simulation*, Phys. Rev. B **105**, 033907 (2009).

[41] S. Maekawa and M. Tachiki, *Ultrasonic attenuation and exchange striction in rare earth metals*, Phys. Rev. B **18**, (1978).

[42] G. Balakrishnan, O. A. Petrenko, M. R. Lees, and D. McK. Paul, J. Phys. Condens. Matter **10**, L723 (1998).

[43] T. Herrmannsdörfer, H. Krug, F. Pobell, S. Zherlitsyn, H. Eschrig, J. Freudenberger, K. H. Mueller, and L. Schultz, *The High Field Project at Dresden/Rossendorf: A pulsed 100 T/10 ms laboratory at an infrared free-electron-laser facility*, J. Low Tempe. Phys. **133**, 41 (2003).

[44] S. Zherlitsyn, B. Wustmann, T. Herrmannsdörfer, J. Wosnitza, *Magnet-technology development at the Dresden high magnetic field laboratory*, J. Low Temp. Phys. **170**, 447-451, (2013).

[45] S.V. Isakov, R. Moessner and S. L. Sondhi, *Why spin ice obeys the ice rules*, Phys. Rev. Lett. **95**, 217201 (2005).

[46] P. W. Anderson , *Ordering and antiferromagnetism in ferrites*, Phys. Rev. **102**, 1008 (1956).

[47] M. J. Harris, S. T. Bramwell, D. F. McMorrow, T. Zeiske, and K. W. Godfrey, *Geometrical frustration in the ferromagnetic pyrochlore* $Ho_2Ti_2O_7$, Phys. Rev. Lett. **79**, 2554 (1997).

[48] L. Pauling,*The Structure and entropy of ice and of Other crystals with some randomness of atomic arrangement*, J. Am. Chem. Soc., **57**, 2680-2684 (1935).

[49] D. Pomaranski, L. R. Yaraskavitch, S. Meng, K. A. Ross, H. M. L. Noad, H. A. Dabkowska, B. D. Gaulin and J. B. Kycia,*Absence of Pauling's residual entropy in thermally equilibrated* $Dy_2Ti_2O_7$, Nat. Phys. **9**, 353 (2013).

[50] B. C. den Hertog and Michel J. P. Gingras, *Dipolar interactions and origin of spin ice in Ising pyrochlore magnets*, Phys. Rev. Lett. **84**, 3430 (2000).

[51] R. Higashinaka and Y. Maeno, *Field-induced transition on a triangular plane in the spin-ice compound* $Dy_2Ti_2O_7$, Phys. Rev. Lett. **95**, 237208 (2005).

[52] S. T. Bramwell, M. J. Harris, B. C. den Hertog, M. J. P. Gingras, J. S. Gardner, D. F. McMorrow, A. R. Wildes, A. L. Cornelius, J. D. M. Champion, R. G. Melko, and T. Fennell, *Spin correlations in* $Ho_2Ti_2O_7$*: A dipolar spin ice system*, Phys. Rev. Lett. **87**, 047205 (2001).

[53] S. Powell and J. T. Chalker,*Classical to quantum mappings for geometrically frustrated systems: Spin-ice in a [100] field*, Phys. Rev. B **78**, 024422 (2008).

[54] S. Lee, S. Onoda, and Leon Balents, *Generic quantum spin ice*, Phys. Rev. B **86**, 104412 (2012).

[55] E. Fradkin and S. H. Shenker, *Phase diagrams of lattice gauge theories with Higgs fields*, Phys. Rev. D **19**, 12 (1979).

[56] L. D. C. Jaubert, J. T. Chalker, P. C. W. Holdsworth, and R. Moessner, *Three-dimensional Kasteleyn transition: Spin ice in a [100] Field*, Phys. Rev. Lett. **100**, 067207 (2008).

[57] T. Fennell, S. T. Bramwell, D. F. McMorrow, P. Manuel and A. R. Wildes, *Pinch points and Kasteleyn transitions in Kagome ice*, Nat. physics. **3** 566 - 572 (2007).

[58] L. D. C. Jaubert, J. T. Chalker, P. C. W. Holdsworth, and R. Moessner, *The Kasteleyn transition in three dimensions: Spin ice in a [100] field*, J. Phys: Conf. Series **145**, 012024 (2009).

[59] S. Powell, *Higgs transitions of spin ice*, Phys. Rev. B **84**, 094437 (2011).

[60] H. Aoki, T. Sakakibara, K. Matsuhira and Z. Hiroi, *Magnetocaloric Effect Study on the Pyrochlore Spin Ice Compound $Dy_2Ti_2O_7$ in a [111] Magnetic Field*, J. Phys. Soc. Jpn. **73**, 2851-2856 (2004).

[61] H. Kadowaki, Y. Ishii, K. Matsuhira, and Y. Hinatsu, *Neutron scattering study of dipolar spin ice $Ho_2Sn_2O_7$: Frustrated pyrochlore magnet*, Phys. Rev. B **65**, 144421 (2002).

[62] A. V. Shlyakhtina, S. N. Savvin, A. V. Levchenko, I. V. Kolbanev, O. K. Karyagina, and L. G. Shcherbakova, *Synthesis and High-Temperature Electrical Conductivity of $Ln_2Ti_2O_7$ and $LnYTi_2O_7$ (Ln = Dy, Ho)*, Inorg. Mat. **44**, 3 (2008).

[63] O. A. Petrenko, M.R. Lees and G. Balakrishnan, *Magnetization process in the spin-ice compound $Ho_2Ti_2O_7$*, Phys. Rev. B **68**, 012406 (2003).

[64] T. Fennell, P. P. Deen, A. R. Wildes, K. Schmalzl, D. Prabhakaran, A. T. Boothroyd, R. J. Aldus, D. F. McMorrow, and S. T. Bramwell, *Magnetic Coulomb Phase in the Spin Ice $Ho_2Ti_2O_7$*, Science **415**, 326 (2009).

[65] O. A. Petrenko, M.R. Lees and G. Balakrishnan, *Titanium pyrochlore magnets: how much can be learned from magnetization measurements?*, J. Phys.: Condens. Matter **23**, 164218 (2011).

[66] J. Snyder, B. G. Ueland, J. S. Slusky, H. Karunadasa, R. J. Cava, and P. Schiffer, *Low-temperature spin freezing in the $Dy_2Ti_2O_7$ spin ice*, Phys. Rev. B **69**, 064414 (2004).

[67] K. Matsuhira, H Sato, T. Tayama, Z. Hiroi, S. Takagi, and T. Sakakibara, *Observation of a novel phase transition induced by a magnetic field in the pyrochlore spin ice compound*, J. Phys.: Condens. Matter **19**, 145269 (2007).

[68] M. Saito, R. Higashinaka, and Y. Maeno, *Magnetodielectric response of the spin-ice $Dy_2Ti_2O_7$*, Phys. Rev. B **72**, 144422 (2005).

[69] P. Que'merais, P. McClarty, and R. Moessner, *Possible quantum diffusion of polaronic muons in $Dy_2Ti_2O_7$ spin ice*, Phys. Rev. Lett **109**, 127601 (2012).

[70] R. Moessner and S. L. Sondhi, *Theory of the [111] magnetization plateau in spin ice*, Phys. Rev. B **68**, 064411 (2003).

[71] T. Katsufuji and H. Takagi, *Magnetocapacitance and spin fluctuations in the geometrically frustrated magnets $R_2Ti_2O_7$ $R$ = rare earth*, Phys. Rev. B **69**, 064422 (2004).

[72] T. Fennell, O. A. Petrenko, B. Fak, J. S. Gardner, S. T. Bramwell, B. Ouladdiaf, *Neutron scattering studies of the spin ices $Ho_2Ti_2O_7$ and $Dy_2Ti_2O_7$ in applied magnetic field*, Phys. Rev. B **72**, 224411 (2005).

[73] J. Snyder, B. G. Ueland, J. S. Slusky, H. Karunadasa, R. J. Cava, A. Mizel, and P. Schiffer, *Quantum-classical reentrant relaxation crossover in $Dy_2Ti_2O_7$ Spin Ice*, Phys. Rev. Lett. **91**, 10 (2003).

[74] L. D. C. Jaubert and P. C. W. Holdsworth, *Signature of magnetic monopole and Dirac string dynamics in spin ice*, Nat. Phys. **5**, 258 (2009).

[75] J. P. Clancy, J. P. C. Ruff, S. R. Dunsiger, Y. Zhao, H. A. Dabkowska, J. S. Gardner, Y. Qiu, J. R. D. Copley, T. Jenkins, and B. D. Gaulin, *Revisiting static and dynamic spin-ice correlations in $Ho_2Ti_2O_7$ with neutron scattering*, Phys. Rev. B **79**, 014408 (2009).

[76] G. Ehlers, A. L. Cornelius, T. Fennell, M. Koza, S. T. Bramwell and J. S. Gardner, *Evidence for two distinct spin relaxation mechanisms in 'hot' spin ice $Ho_2Ti_2O_7$*, J. Phys.: Condens. Matter **16**, S635-642 (2004).

[77] K. Matsuhira, C. Paulsen, E. Lhotel, C. Sekine, Z. Hiroi, and S. Takagi, *Spin Dynamics at very low temperature in spin ice $Dy_2Ti_2O_7$*, J. Phys. Soc. Jpn. **80**, 123711 (2011).

[78] J. A. Quilliam, L. R. Yaraskavitch, H. A. Dabkowska, B. D. Gaulin, and J. B. Kycia, *Dynamics of the magnetic susceptibility deep in the Coulomb phase of the dipolar spin ice material* $Ho_2Ti_2O_7$, Phys. Rev. B **83**, 094424 (2011).

[79] D. Slobinsky, C. Castelnovo, R. A. Borzi, A. S. Gibbs, A. P. Mackenzie, R. Moessner, and S. A Grigera, *Unconventional magnetization processes and thermal runaway in spin-ice* $Dy_2Ti_2O_7$, Phys. Rev. Lett. **105**, 267205 (2010).

[80] S. Erfanifam, S. Zherlitsyn, J. Wosnitza, R. Moessner, O. A. Petrenko, G. Balakrishnan, and A. A. Zvyagin, *Intrinsic and extrinsic nonstationary field-driven processes in the spin-ice compound* $Dy_2Ti_2O_7$, Phys. Rev. B **84**, 220404(R) (2011).

[81] G. Kolland, O. Breunig, M. Valldor, M. Hiertz, J. Frielingsdorf, and T. Lorenz, *Thermal conductivity and specific heat of the spin-ice compound* $Dy_2Ti_2O_7$*: Experimental evidence for monopole heat transport*, Phys. Rev. B **86**, 060402(R) (2012).

[82] Z. Hiroi, K. Matsuhira, S. Takagi, T. Tayama and T. Sakakibara, *Specific Heat of Kagome ice in the pyrochlore oxide* $Dy_2Ti_2O_7$, J. Phys. Soc. Jpn. **72**, 411-418 (2003).

[83] C. Krey, S. Legl, S. R. Dunsiger, M. Meven, J. S. Gardner, J. M. Roper, and C. Pfleiderer, *First order metamagnetic transition in* $Ho_2Ti_2O_7$ *observed by vibrating coil magnetometry at milli-Kelvin temperatures*, Phys. Rev. Lett. **108**, 257204 (2012).

[84] J. Lago, S. J. Blundell and C Baines, *$\mu$SR investigation of spin dynamics in the spin-ice material* $Dy_2Ti_2O_7$, J. Phys.: Condens. Matter **19**, 326210 (2007).

[85] H. Fukazawa, R. G. Melko, R. Higashinaka, Y. Maeno, and M. J. P. Gingras, *Magnetic anisotropy of the spin-ice compound* $Dy_2Ti_2O_7$, Phys. Rev. B **65**, 054410 (2002).

[86] M. Mczka, M. L. Sanjuan, A. F. Fuentes, L. Macalik, J. Hanuza, K. Matsuhira, and Z. Hiroi, *Temperature-dependent studies of the geometrically frustrated pyrochlores* $Ho_2Ti_2O_7$ *and* $Dy_2Ti_2O_7$, Phys. Rev. B **79**, 214437 (2009).

[87] S. Rosenkranz, A. P. Ramirez, A. Hayashi, R. J. Cava, R. Siddharthan, and B. S. Shastry, *Crystal-field interaction in the pyrochlore magnet* $Ho_2Ti_2O_7$, J. Appl. Phys. **87**, 5914 (2000).

[88] S. T. Bramwell, *Generalised longitudinal susceptibility for magnetic monopoles in spin ice*, Phil. Trans. R. Soc. A **370** 57385766 (2012).

[89] Y. Nakanishi, T. Kumagai, and M. Yoshizawa, *Elastic properties of the rare-earth dititanates* $R_2Ti_2O_7$ *(R = Tb, Dy, and Ho)*, Phys. Rev. B **83**, 184434 (2011).

[90] T. W. Kephart and Thomas J. Weiler, *Magnetic monopoles as the highest energy cosmic ray primaries*, Astroparticle Physics **4**, 271–279 (1996).

[91] J. Preskill, *Magnetic monopoles*, Ann. Rev. Nucl. Part. Sci **34**, 461–530 (1984).

[92] P. Langacker, G. Segre, and S. Soni, *Majorana neutrinos nucleosynthesis, and the lepton asymmetry of the universe*, Phys. Rev. D **26**, 12 (1982).

[93] I. V. Kolokolov and P.V.Vorob'ev, *Cherenkov radiation of magnon and phonon by the slow magnetic monopole*, JETP Lett. **67**, 910-912 (1998).

[94] R. D. Gardner, B. Cabrera, M. E. Huber, and M. A. Taber, *Search for cosmic-ray magnetic monopoles using a three-loop superconductive detector*, Phys. Rev. D **44**, 622-635 (1990).

[95] P. V. Vorob'ev, I. V. Kolokolov and V. V. Ianovsk *On a new method of search for magnetic monopoles*, Astronomical & Astrophysical Transactions **19**, 675-683 (2000).

[96] K. A. Milton, *Theoretical and experimental status of magnetic monopoles*, Rep. Prog. Phys **69**, 1637-1711 (2006).

[97] J. S. Song, *Theory of magnetic monopoles and electric-magnetic duality: a prelude to s-duality* J. Undergrad. Sci **3**, 47-55 (1996).

[98] P. B. Price, E. K. Shirk, W. Z. Osborne and L. S. Pinsky, *evidence for detection of moving magnetic monopole*, Phys. Rev. Lett **35**, 8 (1975).

[99] M. Wilkens, *Quantum Ppase of a moving dipole*, Phys. Rev. Lett **72**, 1 (1994).

[100] Henry H. Kolm, F. Villa, and A. Odian, *search for amgnetic monopoles*, Phys. Rev. D **4**, 5 (1971).

[101] R. R. Ross, P. H. Eberhard, L. W. Alwarez and R. D. Watt, *Search for magnetic monopoles in lunar material using an electromagnetic detector*, Phys. Rev. D **8**, 3 (1973).

[102] S. D. Drell, N. M. Croll, M. T. Mueller, S. J. Parke and M. A. Puderman, *Energy loss of slowly moving magnetic monopole in matter*, Phys. Rev. Lett **50**, 9 (1983).

[103] Xiao-Liang Qi, R. Li, J. Zang, and Shou-Cheng Zhang, *Inducing a magnetic monopole with topological surface states*, Science, **323**, 1184 (2009).

[104] C. Castelnovo, R. Moessner and S. L. Sondhi, *Debye-Hueckel theory for spin ice at low temperature*, Phys. Rev. B **84**, 144435 (2011).

[105] G. Sala, C. Castelnovo, R. Moessner, S. L. Sondhi, K. Kitagawa, M. Takigawa, R. Higashinaka, and Y. Maeno, *Magnetic Coulomb fields of monopoles in spin ice and their signatures in the internal field distribution*, Phys. Rev. Lett. **108**, 217203 (2012).

[106] Y. Wan and Oleg Tchernyshyov, *Quantum strings in quantum spin ice*, Phys. Rev. Lett **108**, 247210 (2012).

[107] I. A. Ryzhkin and M. I. Ryzhkin, *Screening of the magnetic field by magnetic monopoles in spin ice*, JETP Letters **93**, 384-387 (2011).

[108] T. Sakakibara, T. Tayama, Z. Hiroi, K. Matsuhira, and S. Takagi, *Observation of a liquid-gas-type transition in the pyrochlore spin ice compound* $Dy_2Ti_2O_7$ *in a magnetic Field*, Phys. Rev. Lett. **90**, 207205 (2003).

[109] S. R. Giblin, S. T. Bramwell, P. C. W. Holdsworth, D. Prabhakaran, and I. Terry, *Creation and measurement of long-lived magnetic monopole currents in spin ice*, Nat. Phys. **7**, 252 (2011).

[110] H. Kadowaki, N. Doi, Y. Aoki, Y. Tabata, T. J. Sato, J. W. Lynn, K. Matsuhira, and Z. Hiroi, *Observation of magnetic monopoles in spin ice*, J. Phys. Soc. Jpn **78**, 103706 (2009).

[111] M. Tachiki and S. Maekawa, *Effect of magnetic field on sound propagation near magnetic phase transition temperatures*, Progr. Theor. Phys. **51**, 1 (1974).

[112] O. Chiatti, A. Sytcheva, J. Wosnitza, S. Zherlitsyn, A. A. Zvyagin, V.S. Zapf, M. Jaime, and A. Paduan-Filho, *Character of magnetic excitations in a quasi-one-dimensional antiferromagnet near the quantum critical points: Impact on magnetoacoustic properties*, Phys. Rev. B **78**, 094406 (2008).

[113] A. Sycheva, O. Chiatti, J. Wosnitza, S. Zherlitsyn, A.A. Zvyagin, R. Coldea, and Z. Tylczynski, *Short-range correlations in quantum frustrated spin system*, Phys. Rev. B **80**, 224414 (2009).

[114] P. N. Timonin, *Spin ice in a field: quasi-phases and pseudo-Transitions*, J. Exp. Theor. Phys. **113**, 251-265 (2011).

[115] A.A. Zvyagin, *Re-distribution (condensation) of magnons in a ferromagnet under pumping*, Fiz. Nizk. Temp. **33**, 1248 (2007) [Low Temp. Phys. **33**, 948 (2007)].

[116] Y. P. Varshni, *Temperature dependence of the elastic constants*, Phys. Rev. B **2**, 10 (1970).

[117] L. D. C. Jaubert and P. C. W. Holdsworth, *Magnetic monopole dynamics in spin ice*, J. Phys.: Condens. Matter **23**, 164222 (2011).

[118] R. G. Melko, B. C. den Hertog, and M. J. P. Gingras, *Long-range order at low temperatures in dipolar spin ice*, Phys. Rev. Lett. **87**, 067203 (2001).

[119] A. Bertin, Y. Chapuis, P. Dalmas de Réotier, and A. Yaouanc,*Crystal electric field in the* $R_2Ti_2O_7$ *pyrochlore compounds*, J. Phys.: Condens. Matter **24**, 256003 (2012).

[120] R. Applegate, N. R. Hayre, R. R. P. Singh, T. Lin, A. G. R. Day, and M. J. P. Gingras, *Vindication of* $Yb_2Ti_2O_7$ *as a Model Exchange Quantum Spin Ice*, Phys. Rev. Lett. **109**, 097205 (2012).

[121] J. D. Thompson, P. A. McClarty, H. M. Rønnow, L. P. Regnault, A. Sorge, and M. J. P. Gingras, *Rods of neutron scattering intensity in* $Yb_2Ti_2O_7$*: Compelling evidence for significant anisotropic exchange in a magnetic pyrochlore oxide*, Phys. Rev. Lett. **106**, 187202 (2011).

[122] L. Yin, J. S. Xia, Y. Takano, N. S. Sullivan, Q. J. Li, and X. F. Sun, *Low-temperature low-field phases of the pyrochlore quantum magnet* $Tb_2Ti_2O_7$, Phys. Rev. Lett. **110**, 137201 (2013).

[123] T. Fennell, M. Kenzelmann, B. Roessli, M. K. Haas, and R. J. Cava, *Power-Law Spin Correlations in the Pyrochlore Antiferromagnet* $Tb_2Ti_2O_7$, Phys. Rev. Lett. **109**, 017201 (2012).

[124] S. Legl, C. Krey, S. R. Dunsiger, H. A. Dabkowska, J. A. Rodriguez, G. M. Luke, and C. Pfleiderer, *Vibrating-Coil Magnetometry of the Spin Liquid Properties of* $Tb_2Ti_2O_7$, Phys. Rev. Lett. **109**, 047201 (2012).

[125] Lieh-Jeng Chang, S. Onoda, Y. Su, Ying-Jer Kao, Ku-Ding Tsuei, Y. Yasui, K. Kakurai and M. R. Lees, *Higgs transition from a magnetic Coulomb liquid to a ferromagnet in* $Yb_2Ti_2O_7$, Nat. Commun. **3**, 992 (2012).

[126] J. A. Hodges, P. Bonville, A. Forget, A. Yaouanc, P. Dalmas de Reotier, G. Andre, M. Rams, K. Krolas, C. Ritter, P. C. M. Gubbens, C. T. Kaiser, P. J. C. King, and C. Baines, *First-order transition in the spin dynamics of geometrically frustrated* $Yb_2Ti_2O_7$, Phys. Rev. Lett. **88**, 077204 (2002).

[127] K. A. Ross, L. R. Yaraskavitch, M. Laver, J. S. Gardner, J. A. Quilliam, S. Meng, J. B. Kycia, D. K. Singh, Th. Proffen, H. A. Dabkowska, and B. D. Gaulin, *Dimensional evolution of spin correlations in the magnetic pyrochlore* $Yb_2Ti_2O_7$, Phys. Rev. B **84**, 174442 (2011).

[128] A. Yaouanc, P. Dalmas de Reotier, C. Marin, and V. Glazkov, *Single-crystal versus polycrystalline samples of magnetically frustrated* $Yb_2Ti_2O_7$*: Specific heat results*, Phys. Rev. B **84**, 172408 (2011).

[129] L. Savary and L. Balents, *Coulombic quantum liquids in spin*-1/2 *pyrochlores*, Phys. Rev. Lett. **108**, 037202 (2012).

[130] H. B. Cao, A. Gukasov, I. Mirebeau and P. Bonville, *Anisotropic exchange in frustrated pyrochlore* $Yb_2Ti_2O_7$, J. Phys.: Condens. Matter **21**, 492202 (2009).

[131] R. F. Wang, C. Nisoli, R. S. Freitas, J. Li, W. McConville, B. J. Cooley, M. S. Lund, N. Samarth, C. Leighton, V. H. Crespi, P. Schiffer, *Artificial 'spin ice' in a geometrically frustrated lattice of nanoscale ferromagnetic islands*, Nature **439**, 303 (2006).

[132] G. Mueller and R. Moessner, *Magnetic multipole analysis of kagome and artificial spin-ice dipolar arrays*, Phys. Rev. B **80**, 140409(R) (2009).

# Publication

**S. Erfanifam**, S. Zherlitsyn, J. Wosnitza, R. Moessner, O. A. Petrenko, G. Balakrishnan, and A. A. Zvyagin, *Intrinsic and extrinsic nonstationary field-driven processes in the spin-ice compound* $Dy_2Ti_2O_7$, Phys. Rev. B **84**, 220404(R) (2011).

# Versicherung

Hiermit versichere ich, dass ich die vorliegende Arbeit ohne unzulässige Hilfe Dritter und ohne Benutzung anderer als der angegebenen Hilfsmittel angefertigt habe. Die aus fremden Quellen direkt oder indirekt übernommenen Gedanken sind als solche kenntlich gemacht. Die Arbeit wurde bisher weder im Inland noch im Ausland in gleicher oder ähnlicher Form einer anderen Prüfungsbehörde vorgelegt.

Diese Dissertion wurde unter der Betreuung von Prof. J. Wosnitza im dem Hochfeld-Magnetlabor Dresden (HLD) am HZDR angefertigt.

Ich erkenne die Promotionsordnung an der Fakultät Mathematik und Naturwissenschaften der Technischen Universität Dresden an.

Dresden, 20. September. 2013 Salim Erfanifam

# Curriculum vitae

Salim Erfanifam, born 21 January 1983 in Maragheh, Eastern Azarbaijan province, Iran.
2001-2005 B.S., Physics in **University of Tabriz**, Tabriz, Iran.
2005-2008 M.S., Nanophysics **University of Kashan**, Kashan, Iran.
2009-2013 International Max Planck Research School for "Dynamical Processes in Atoms, Molecules and Solids", and scientific employee of High-magnetic field laboratory of HZDR, Dresden, Germany.

# Acknowledgment

The work presented in this thesis has benefited from the help of many people. First I would like to thank my supervisor and advisor, Joachim Wosnitza and Sergei Zherlitsyn, for their guidance and support. They provided me with many opportunities to meet and interact with other physicists through many conferences. Furthermore, I would also like to thank my parents for their endless love and support. I must thank the other member of the ultrasound group, Shadi Shaikh Yasin. He provided lots of help at the beginning of my Ph.D for running the experiment. The theoretical explanations of the results were made possible with the invaluable help of Roderich Moessner, Andrei Zvyagin, and Paul Mc Clarty. Also I acknowledge Oleg Petrenko, Geetha Balakrishnan, and Andrey Maljuk for providing the samples. I would also like to acknowledge with much appreciation the crucial role of the staff of high magnetic field laboratory, who provided a nice atmosphere to complete this thesis.